The Intrinsic Quantum Hall Effect

by

Daping Chu

Department of Physics

University of Warwick

Coventry CV4 7AL

This thesis is presented to

the University of Warwick

in partial fulfilment of the requirements

for entry to the degree of

Doctor of Philosophy

11 July 1994

Abstract

We first consider an interacting two-dimensional electron gas in a ballistic quantum wire in an external magnetic field. Self-consistent calculations are made of the electrostatic Hall potential (EHP), the local chemical potential (LCP), and current density in a uniform ballistic quantum wire containing two-dimensional electrons in a perpendicular magnetic field B when either one or two subbands are occupied. The corresponding Hall resistances, $R_{\rm EHP}$ and $R_{\rm LCP}$, are also calculated. The former is nearly linear in B in spite of subband depopulation. The latter is quantised but the quantisation steps are rounded because of overlap of the forward and backward going wave functions. Secondly, self-consistent calculations are also made of wave functions and the two kinds of Hall resistances for the same system in a weak perpendicular magnetic field when several subbands are occupied. We find intermittent quenching of the Hall resistance associated with the local chemical potential as the electron density varies. The quenching is due to the overlap of opposite-going wave functions in the same subband, which is enhanced significantly by the singularity of the density of states at the subband minima as well as by Coulomb interactions between the electrons. Finally, with a model calculation, we demonstrate that a non-invasive measurement of intrinsic quantum Hall effect defined by the local chemical potential in a ballistic quantum wire can be achieved with the aid of a pair of voltage leads which are separated by potential barriers from the wire. Büttiker's formula is used to determine the chemical potential being measured and is shown to reduce exactly to the local chemical potential in the limit of strong potential confinement in the voltage leads. Conditions for quantisation of Hall resistance and measuring local chemical potential are given.

Acknowledgements

I would like to take this opportunity to thank some of the many people who have helped me to reach this stage:

First of all, I would like to thank Prof. P. N. Butcher for his excellent supervision and guidance. The encouragement and help from him and his wife, Freda, have been invaluable both in physics and in real life. I would also like to take this opportunity to thank the many people who have helped with discussions, comments and communications, especially Dr. Markus Büttiker, Dr. Chris Ford, Dr. Duane Johnson, Dr. Peter Main and Dr. Frank Stern.

Thanks are due to my previous professors in the Nanjing University and my former colleagues in the Institute of Physics, Chinese Academy of Sciences. Seven years in the Nanjing University and five years in the Institute of Physics gave me the opportunity to get into the world of condensed matter physics.

A great deal of thanks go to my wife, Miao Lu, my parents and my sister for all their moral support and interest throughout this period.

Thanks also go to Tao Xiang, Yue Yu, Hui Tang, Yanmin Li, John McInnes, my other friends, and all the members of staff at the Physics Department of the Warwick University for friendship and help received and for making my stay at Warwick a pleasant one.

Finally, I would also like to thank Prof. P. N. Butcher for arranging financial support for me to attend some conferences and workshops and the International Centre of Theoretical Physics, Trieste, for their hospitality during my visits.

Declaration

This thesis, unless where is stated otherwise, contains an account of my own independent research work performed in the Department of Physics at the University of Warwick between October, 1991 and June, 1994 under the supervision of Professor P N Butcher.

Some parts of the work in this thesis have previously been published:

1. "Intrinsic integer quantum Hall effect in a quantum wire"
   D. P. Chu and P. N. Butcher,
   Phys. Rev. B **47**, 10008 (1993);

2. "Quenching of the quantum Hall effect in a uniform ballistic quantum wire"
   D. P. Chu and P. N. Butcher,
   J. Phys.: Condens. Matter **5**, L397 (1993);

3. "A new definition of the local chemical potential in a semiconductor nanostructure"
   P. N. Butcher and D. P. Chu,
   J. Phys.: Condens. Matter **5**, L633 (1993);

4. "Noninvasive measurement of the intrinsic quantum Hall effect"
   D. P. Chu and P. N. Butcher
   Phys. Rev. Lett., **72**, 3698 (1994).

Relevant Books and Review Articles

Some of the most relevant books and review articles published recently are:

1. *The Physics of the Two-Dimensional Electron Gas*, Vol. 157 of NATO ASI Series B: Physics, edited by J. T. Devreese and F. M. Peeters, Plenum Press, New York, 1987.

2. *The Quantum Hall Effect*, edited by R. E. Prange and S. M. Girvin, Springer-Verlag, New York, 1987;

3. *IBM Journal of Research and Development*, Vol. 32, No. 3, 1988;

4. *Nanostructure Physics and Fabrication*, edited by M. A. Reed and W. P. Kirk, Academic Press, San Diego, 1989;

5. C. W. J. Beenakker and H. van Houten, in Vol. 44 of *Solid State Physics: Advances in the Research and Applications*, edited by H. Ehrenreich and D. Turnbull, Academic Press, New York, 1991;

6. *Mesoscopic Phenomena in Solids*, Vol. 30 of *Modern Problems in Condensed Matter Sciences*, edited by B. L. Altshuler, P. A. Lee, and R. A. Webb, North-Holland, Amsterdam, 1991;

7. *Quantum Coherence in Mesoscopic Systems*, Vol. 254 of NATO ASI Series B: Physics, edited by B. Kramer, Plenum Press, New York, 1991;

8. *Nanostructure Systems*, Vol. 35 of *Semiconductors and Semimetals*, edited by M. A. Reed, Academic Press, San Diego, 1992;

9. *Quantum Transport in Semiconductors*, edited by D. K. Ferry and C. Jacoboni, Plenum Press, New York, 1992;

10. *Physics of Nanostructures*, edited by J. H. Davies and A. R. Long, IOP Publishing, Bristol, 1992;

11. *Physics of Low-Dimensional Semiconductor Structures*, edited by P. N. Butcher, N. H. March, and M. P. Tosi, Plenum Press, New York, 1993.

Preface

In this thesis, we are going to discuss the intrinsic quantum Hall effect. By "intrinsic" we mean the results of noninvasive measurements of a system. We choose a two-dimensional electron gas (2DEG) confined in a ballistic quantum wire (BQW) and study its magnetic response when there is a current flowing through the wire.

The thesis is arranged as follows. It begins with the introductions to the experimental and theoretical backgrounds of the problem. Ideas, definitions and physical pictures of a 2DEG, microstructures, resistance, chemical potential and measurement effects are taken from the level of their definition to a form suitable to the problem which we are going to study. The relationship between the chemical potential in an equilibrium system and the current driving force in a transport system is carefully examined. We present a new definition of the so-called local chemical potential (LCP), which extends the original idea to general situations and gives the LCP a new physical interpretation. Previous experimental and theoretical work in relevant fields are described. The derivations of the key formulae which we use are included as well as some relevant matters which are important but are not usually mentioned in general review articles. The details which are not mentioned here can be easily found in the references. When we turn to our work we again give the essential steps and the results. Detailed derivations are included as appendices. The three chapters before the final Conclusion give our main results which are also described in the Abstract. Our results and discussions are all for the case of the temperature $T = 0$ K unless we indicate eitherwise. Finally, we summarise what we have contributed to the understanding of the intrinsic quantum Hall effect.

Contents

List of Figures

Chapter 1

Two-Dimensional Mesoscopic Systems

1.1 Introduction

The real world we live in is three-dimensional (3D) and objects in it are described by three lengths: width, height and length. Usually the length scale of each dimension is many orders larger than the microscopic characteristic lengths associated with electrons, such as de Broglie wavelength, lattice constants, etc. Then, the object is macroscopically 3D and we can employ translation invariance in all three dimensions when we study its electronic properties. Boundaries do not have any particular effect on the results but merely tell us how far the object extends.

Obviously, it is possible to reduce any one of these three lengths to a very small value so that translational invariance does not apply in the corresponding direction. The dimensionality of the object is thus reduced. At the same time, the energy difference between the electron ground state and the first excited state associated with that direction increases and can become much larger than energy differences associated with other directions. The electron momentum along this special direction is then no longer a good quantum number. The electronic properties of such an object show two-dimensional (2D) macroscopic character, which are drastically different from its 3D counterparts. Similar

further reductions of length in other two directions will result in one-dimensional (1D) and zero-dimensional (0D) systems.

If we only decrease the lengths in the other two directions to such a size which is comparable with some of the microscopic electron characteristic lengths without destroying translation invariance, many new and novel phenomena have been observed in such **two-dimensional mesoscopic systems.** This is an exceedingly rich field. The ability to vary different variables results in nearly limitless possibilities for creating different structures for researches and applications.

In this introductory chapter, we will briefly introduce the relevant physics of 2D mesoscopic systems and the techniques for making them. We concentrate on heterostructures and the two-dimensional electron gas (2DEG), the split-gate technique, and the basic concepts of mesoscopic and ballistic systems. At the end, the quantum Hall effect (QHE) and measurement procedure will be discussed.

1.2 Heterostructures and the 2DEG

The ability to study a low-dimensional solid state system has been longed for by condensed matter physicists for decades. The attraction of this field is their potential for exhibiting macroscopic quantum size effects and the problems associated with how to observe and control the system parameters to study them.

In 1957 J. R. Schrieffer suggested that the narrow confinement potential of an inversion layer may lead to the observation of non-classical electron transport behaviour [1]. This was demonstrated in 1966 by measuring the low temperature magnetotransport properties of a 2DEG in a silicon inversion layer [2]. Since then, intensive efforts have been made in the exploration of 2DEG systems.

Inversion layers are formed at the interface between a semiconductor and an insulator or between two semiconductors with one of them acting as an insulator. As always, basic research in condensed matter physics has greatly benefited

from the rapid development of industrial technology. Ultra-thin epitaxial film growth techniques have made it possible for scientists to make a multilayered thin wafer, *i.e.* a **heterostructure**, with different materials in different layers. The first quantum well [3] was successfully made in 1974.

A Nobel Prize was awarded in this field in 1985 for the discovery of the QHE [4]: the quantisation of the Hall resistance of high mobility 2DEGs in a high perpendicular magnetic field. The system used was a Si/SiO_2 heterostructure. Si and SiO_2 are for the semiconductor and insulator respectively. Because of the roughness of the crystal discontinuity at the interface as well as trapped impurities in the SiO_2 and Si layers, scattering of electrons is strong and limits the mobility of electrons to $\sim$ 4 m^2/Vs or less. Further researches in this system are therefore restricted.

In 1978, a technique for creating an exceptionally pure 2DEG was invented which is known as modulation doping [5]. It spatially separates the charge carriers in a conduction band from the impurity atoms which they come. The electron mobility is then improved dramatically. This method has opened a door for the researchers to study electronic transport in ultra-high mobility carrier systems.

Recently, modulation-doped $GaAs/Al_xGa_{1-x}As$ heterostructures [5], with $Al_xGa_{1-x}As$ playing the role of insulator, has been intensively studied because of its extraordinary high electron mobility. A schematic plot of a typical layer structure and the corresponding band-bending diagram is shown in Figs. 1.1(a) and 1.1(b) respectively. Molecular-beam epitaxy is used to fabricate such structures, because it produces the highest quality structures in the terms of purity, interface sharpness and crystalline perfection. The growth of thin layers can be controlled with extreme precision, approaching the scale of single atomic layer. The relative smooth interfaces ensure only moderate scattering by interface roughness. The scattering of electrons is further largely reduced by modulation doping in which the conduction electrons are separated from the ionised donors in the doped $Al_xGa_{1-x}As$ layer. More reduction is achieved by inserting an un-doped $Al_xGa_{1-x}As$ "spacer layer" to keep the doped layer from the

heterointerface. Record low temperature mobility up to 10^3 m^2/Vs has been reported [6]. This corresponds to electron elastic mean free path exceeding 0.1 mm. In Fig. 1.1(b), we can see the conduction electrons supplied by the donors in the $Al_xGa_{1-x}As$ layer are confined in a very narrow potential well the the interface of GaAs and $Al_xGa_{1-x}As$. This confinement potential well is formed by the competition between the repulsive potential barrier due to the band offset at the interface of GaAs and $Al_xGa_{1-x}As$ and the attractive electrostatic potential resulted by the positively charged donors in the $Al_xGa_{1-x}As$ layer.

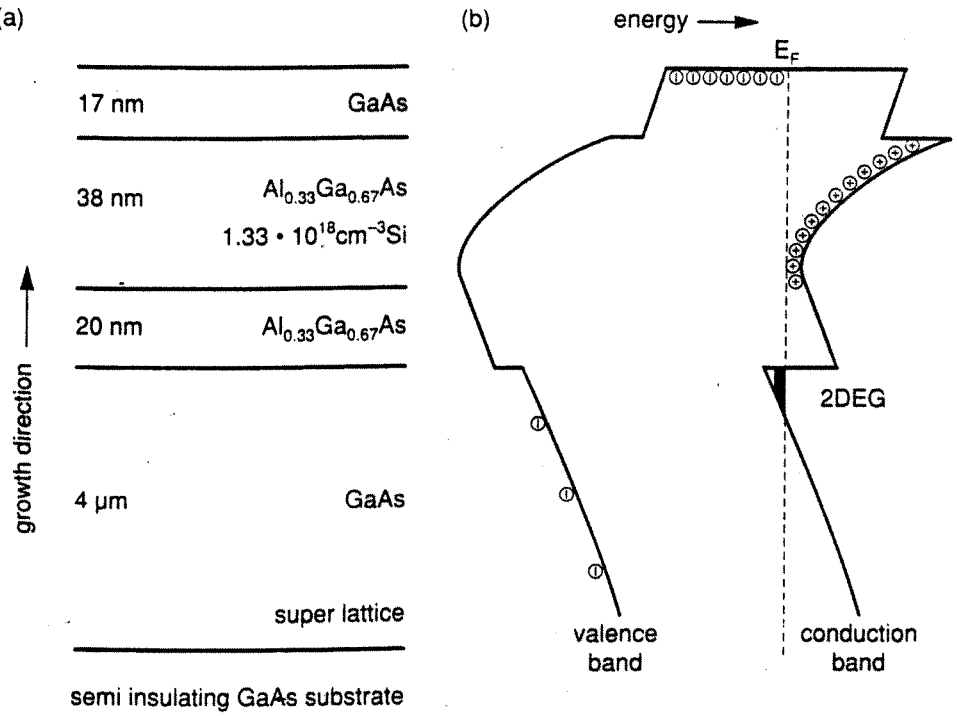

Figure 1.1: Layers of a modulation doped GaAs/$Al_xGa_{1-x}As$ heterostructure (a) and the corresponding band-bending diagram and 2DEG (b). The numbers here are typical. The band offset between GaAs and $Al_xGa_{1-x}As$ is about 0.3 eV when $x = 0.33$. (From Ref. [7])

The electrons in the confinement potential well can move freely parallel to the interface and are confined with confinement energy levels in the perpen-

dicular direction. This results in the formation of 2D subbands in the well. Because the wavelength of these conduction electrons at the Fermi energy is much larger than the GaAs lattice constants, we can use the effective mass approximation and treat the electrons collectively as a gas with a certain density moving in a continuous background. (The Fermi wavenumber $k_F = (2\pi n_s)^{1/2}$ and typically the sheet electron density is $n_s \sim 10^{15}$ m^{-2} the Fermi wavelength is $\lambda_F = 2\pi/k_F \sim$ 80 nm.) We can further just concern ourselves with the 2D behaviour of the electron gas since only the lowest subband is usually populated in typical experimental situations. Based on the above understandings, it will be sensible to model these confined conduction electrons as a **2DEG** in the heterostructure when we calculate its electronic properties.

1.3 Split-gate Technique and Microstructures

One of the most important feature of a 2DEG is that we can shape it into any desired ultra-small geometry. There are two approaches, etching a pattern which results in permanent removal of parts of the 2DEG, or using a patterned gate electrode to deplete parts of the 2DEG electrostatically and reversibly. The later is known as **split-gate technique** [8]. By applying a negative voltage to the split-gate the 2DEG immediately beneath the gate electrodes is depleted and the 2DEG is laterally constrained within the area between the electrodes. A **microstructure** is such a patterned 2DEG.

Lithographic techniques are used in creating the gate. Because of the very high spatial resolution needed ($<$ 10 nm), both X-ray and electron beams are employed to generate the photo-lithographic masks which are essential in producing patterned gates. Electron beam which can be focussed into spot sizes less than 1 nm.

A sketch of a quantum point contact [9, 10] made by the split-gate technique is shown in Fig. 1.2. The 2DEG underneath of the split-gate electrodes is patterned by applying the gate voltage on the electrodes. Similarly, quantum wire [8, 11] and quantum dot [12] can also be made. The dimensions of such a semiconductor microstructure can be as small as the electron Fermi wavelength

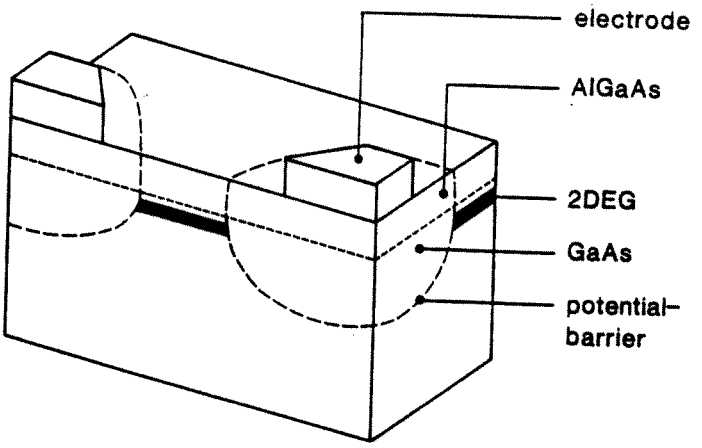

Figure 1.2: A quantum point contact shaped by split-gate technique. (From Ref. [7])

[13]. Recently, microstructures have been fabricated for which the presence or absence of a single electron affects the transport properties [14, 15]. This effect is known as Coulomb blockade which is beyond the range of this thesis.

An additional gate electrode is often put on the top of a microstructure to change the sheet electron density n_s under it as the electric field applied on the electrode varies. Alternatively, split-gate electrodes can be used to do the same thing. This enables us not only to study the density dependence of the electronic transport properties of a 2DEG but also to explore the limit of electronic conduction when the number of the conducting electrons is small. The sheet density of electrons under a large gate electrode depends linearly on the electrostatic gate voltage according to the formula for a parallel plate capacitor $\Delta n_s = \epsilon \Delta V_g / eD$, where the static dielectric constant of GaAs is $\epsilon = 12.8\epsilon_0$ and D is the distance between the gate electrode and the 2DEG.

1.4 Characteristic Lengths and Ballistic Systems

The dramatic improvement in the fabrication of ultra-small conducting devices (microstructures) has greatly increased interest in the novel electron transport phenomena because of the quantum interference which occurs in such systems.

A microstructure is called **mesoscopic** as if it shows quantum size effects which can be measured macroscopically but de not have a macroscopic explanation. Mesoscopic systems occupy the area between the microscopic world which requires a quantum mechanical description and the macroscopic world where we believe classical physics are normally adequate. Many different quantum interference behaviours have been observed and predicted. There are a lot of parameters involved, such as composition, band offset, dimensions, impurities (density and distribution), etc. It is very helpful that we can use some simple quantities as the criteria for classifying mesoscopic systems according to their electronic characteristics. The most convenient and most often used are ratios of the spatial dimensions of a system to its electronic characteristic lengths.

Typical **characteristic lengths** associated with electronic transport properties are elastic and inelastic mean free paths, the phase coherence length, the magnetic length and lattice constants. Most of them are system dependent. The elastic (inelastic) mean free path is the average distance between two elastic (inelastic) scatterings of an electron. The phase coherence length measures how long an electron travels without the phase memory of its wavefunction changing.

The ratios of these lengths to the system dimensions are crucial. For example, quantum interference effects in a system, *e.g.* the Aharonov-Bohm effect [16] in the magnetoresistance of a mesoscopic ring, are found to disappear exponentially when the relevant space dimension becomes large compare to its phase coherence length.

A system with a size much larger than its inelastic mean free path is diffusive and phase random and can be treated classically. Then, random phase averages are made in calculations and resistances are local and additive. While a system with dimensions about in the order of its inelastic mean free path and

larger than its elastic mean free path is diffusive but quantum coherent. It is interesting to notice that an inelastic scattering is not necessarily a dephasing scattering because phase coherence has been observed in the presence of finite energy transfer [17].

Quantum coherent diffusive systems are divided into three classes. The first class shows weak localisation effects in the average conductance [18]. This effect arises from the coherent back-scattering of diffusing electrons, which is sensitive to a weak magnetic field. The behaviour of this effect depends on dimensionality but not the system size as long as it is about or smaller than the inelastic mean free path. The second class shows reproducible conductance fluctuations in a changing magnetic field [19]. The relation of the conductance to the magnitude of an applied magnetic field is system dependent while the amplitude of the fluctuation is universal. The universality arises because the maximum sensitivity of conductance to the change of magnetic field is e^2/h and is independent to the average conductance itself. This effect depends on the ratio of the inelastic mean free path to the system size. Unlike the first two classes which are defined by their low temperature properties, the third class is determined to the thermodynamic properties of quantum coherent mesoscopic system, such as the persistent current [20, 21] and orbital magnetic response [22, 23]. The origin of this class is not clear. Theoretical prediction shows that there should be an average effect due to the constraint of fixed particle number in a mesoscopic system [24]. All these three interference effects involve diffusing electrons and have their mathematical origin in the properties of the disorder-averaged two-particle Green function. More details can be found in Ref. [25].

When the size of a mesoscopic system is less than the inelastic mean free path but larger than or about the elastic mean free path, there will still be diffusion but the phase of electron wave functions are fixed. The electrons in such a system can be described by electron modes. Despite of the changes of the electron distributions between the modes, which are caused by elastic scatterings, the system is still phase-deterministic. Quantum interference of electron wave-

functions without randomness can be observed, such as the Aharonov-Bohm oscillations of the resistance in small metallic ring structures [26].

Furthermore, the phase-preserving properties of electron wavefunctions will be ensured if the dimensions of a system is smaller than both the elastic and inelastic mean free path. This kind of quantum coherent system is known as **ballistic system**. In this regime, quantum transport becomes dominant and the wave nature of the electrons becomes apparent. The motion of electrons in a ballistic system is of course coherent and the energy and momenta are quantised. The resistance is non-local and has a quantum mechanical aspect. The average velocity is not an appropriate basis for a description of the resistance.

An electron waveguide [27] is a ballistic quantum wire (BQW) made of a 2DEG, which is so clean and so small that electron waves can propagate in guided modes without loss of phase coherence. The propagating modes of electrons are characterised by its quasi-one-dimensional (Q1D) geometry. Atomic precision of lithography and crystal growth is needed in fabricating a ballistic quantum wire demonstrating the transport characteristics of an electron waveguide.

There are obvious differences between an optical or microwave waveguide and an electron waveguide. The guided mode of electron is sensitive to an applied electric or magnetic field because it possesses a charge. Moreover, the number of electrons in a specific mode of the waveguide is limited by the Pauli principle due to the fermion feature of electrons.

1.5 Four-lead Measurement and the QHE

Conductance and resistance, as well as conductivity and resistivity, are the most frequently used quantities in characterising the electronic transport properties of a system. The "ances" represent the global features of the system being studied, while the "ivities" are used to refer the local properties. Experimentalists usually use the "ances" because they measure them directly. While, theoreticians normally prefer to calculate the "ivities" since they are size independent. However, if a system is a quantum coherent one, only the "ances" are

the suitable quantities in describing the system because these quantities are not additive any more. For the same reason, in this thesis, we concern the "ances" rather than the "ivities".

For a steady transport system, the resistance is defined as the electrostatic voltage difference applied on the system divided by the amount of the current driven through it (or equivalently using electrostatic voltage difference induced in the system divided by the amount of the current injected into it). The electrostatic voltage drop on a system comes from the electrochemical potential difference between two voltaic electron reservoirs which are connected to the system as current source and drain respectively. The electrostatic voltage difference is normally different from the electrochemical potential difference when the internal resistance between the current source and drain is finite. However, these two differences become one if the internal resistance between the two reservoirs is much larger than the resistance of the system. This is usually true in high accuracy resistance measurements. We assume that this is also the case in our calculations.

The primary resistance measurement uses a pair of leads connected at the two sides a system. The current flowing through and the voltage drop on the system are measured with the same pair of leads. The problem of this method is that the contact resistances at the two sides of the system becomes parts of the measured resistance of the system, so that the final results can be significantly distorted if the system resistance itself is smaller than or comparable to the contact resistance. For excluding this extra part of resistance, **four-lead measurement** is introduced. Two pairs of leads are used to measure current and voltage drop separately. Each of the two voltage leads and the two current leads are connected at each side of the system with the voltage contacts being put closer to the system than the current contacts. Therefore, the voltage drops on the current contacts are not included in what being measured by the voltage leads. While, the amount of current traversing through the voltage contacts are very small because the internal resistance of the voltage measurement circuit is very large. (Sometimes, current-stop procedure is applied in voltage leads in

high precision measurement.) For the same reason, the current in the current leads is equal to the current traversing through the system. Consequently, we can use four-lead configuration to measure the electrochemical potential difference applied on a system and the induced current traversing it and exclude the potential drops on the voltage contacts.

The **Hall effect** was discovered in metal wires in 1879 by E. H. Hall [28]. He observed "the state of stress in the conductor" in the case that "the magnet may tend to deflect the current $\cdots$". This state of stress appears as transverse voltage (known nowadays as the Hall voltage) [29]. Generally speaking, the Hall effect is that the current in a conductor or semiconductor under a perpendicular magnetic field will induce a potential difference in the third direction which is perpendicular to both the current and the magnetic field. In an electric field $\mathbf{E}$, the induced current density $\mathbf{j}$ has a linear relationship with it: $\mathbf{E} = \rho_0 \mathbf{j}$. The normal longitudinal resistivity for a homogeneous electron gas system with the charge of electron $-e$ is $\rho_0 = m^*/n_s e^2 \tau_0$, where m^* is electron effective mass, n_s is density of electrons and $\tau_0 = l_0/v_F$ is relaxation time and is the ratio of electron mean free path to electron Fermi velocity. When a magnetic field $\mathbf{B}$ is applied, an additional bending field $\mathbf{j} \times \mathbf{B}/n_s(-e)$ affects the moving electrons due to the existence of the Lorentz force. Hence, $\mathbf{E} + \mathbf{j} \times \mathbf{B}/n_s(-e) = \rho_0 \mathbf{j}$. In 3D case, the resistivity has the form of a rank 3 tensor. For a 2DEG, which is put in x-y plan under a magnetic field $\mathbf{B}$ in z direction, the resistivity reduces to a rank 2 tensor with the diagonal terms $\rho_{xx} = \rho_{yy} = \rho_0$ for the longitudinal resistivity and the off-diagonal terms $\rho_{xy} = -\rho_{yx} = B/n_s e$ for the Hall resistivity. Similarly, the longitudinal resistance and the Hall resistance for a system can be defined. Usually, the Hall resistivity is a property of the material which a system is made of while the Hall resistance is a character of a system. Four-lead measurement is essential in measuring the Hall resistance because of its off-diagonal nature. Very often six leads are used in a real experiment to measure the longitudinal resistance and the Hall resistance at the same time. A sketch of experiment is shown in Fig. 1.3, which is known as a Hall bar measurement. The shape of a system in the Hall measurement is normally rectangular

in order to avoid the complexity caused by system geometry.

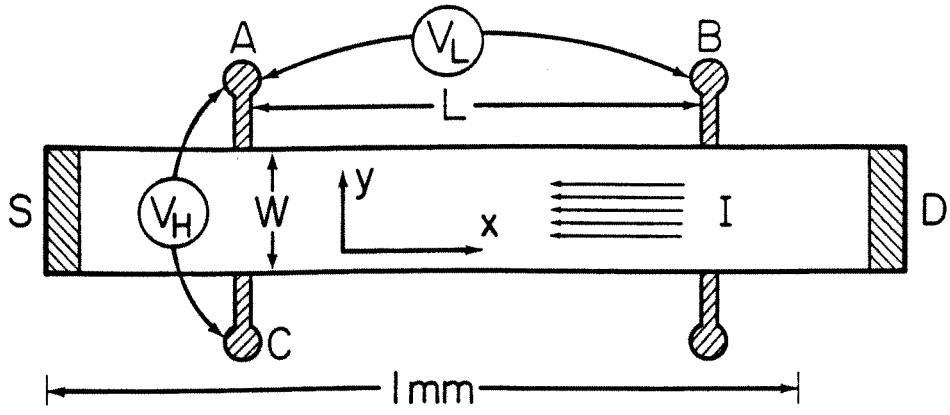

Figure 1.3: A diagram of experimental arrangement in the Hall measurement. S and D stand for electron source and drain. V_L and V_H are the longitudinal voltage drop and the Hall voltage respectively. (From Ref. [30])

The Hall resistance normally increases smoothly when the magnitude of the applied magnetic field increases. In 1980, von Klitzing, Dorda and Pepper observed the **integer QHE** (IQHE) [4]. They found that the Hall resistance of the 2DEG in a Si/SiO_2 inversion layer was fully quantised as the unit of h/e^2 divided by integers at helium temperature and in a strong magnetic field of order 15 T. The accuracy of the quantisation is exceptionally high: about one tenth ppm. A typical experiment result of Hall resistance R_{xy} and longitudinal resistance R_{xx} is shown in Fig. 1.4. Two years later, the **fractional QHE** (FQHE) was also observed for which the quantisation is a rational fraction of h/e^2 [32]. Both the IQHE and the FQHE have attracted intensive research efforts since the time of discovering, trying to understand the mechanisms from both the experimental and the theoretical angles. Reviews can be found in Refs. [33] and [34]. Most of the previous works studying the IQHE have their emphasises on either the 2DEG itself or the terminal feature of microstructure. Is there a kind of IIQHE for a microstructure itself? Can this intrinsic IQHE (IIQHE) be measured? We will give positive answers to both of the two questions in this

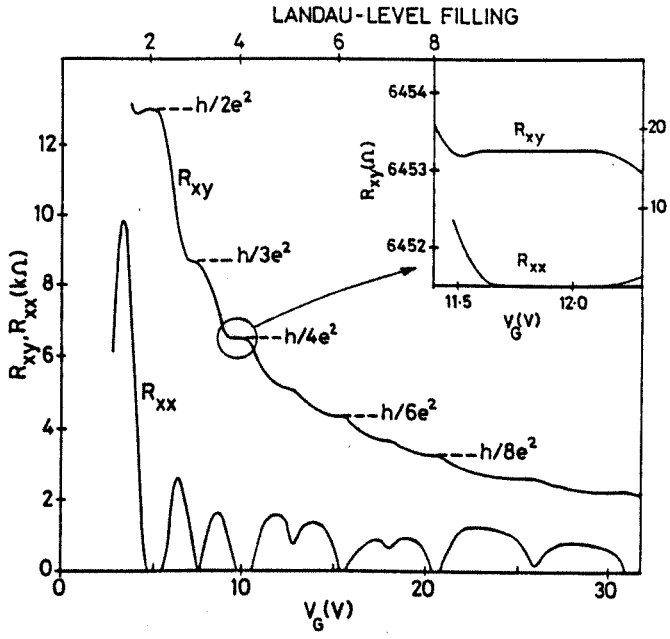

Figure 1.4: The Hall resistance R_{xy} and the longitudinal resistance R_{xx} of the 2DEG in a Si/SiO_2 inversion layer as a function of applied gate voltage V_g. (From Ref. [31])

thesis.

Chapter 2

The electrons in the 2D microstructures

2.1 Introduction

As we already have seen in the previous chapter, a system can be characterised by its dimensions compared with some relevant length scales. In this chapter, we are mainly concerned with the Fermi wavelength $\lambda_F = 2\pi/k_F$ where k_F is the electron wavevector at the Fermi surface. Reduced dimensionality arises when at least one dimension of a system is comparable to λ_F. A system is dynamically 2D when only one dimension is small. The motion of electrons in the corresponding direction is quantised which is known as **spatial quantisation.** As a simple model, the 2DEG has proved to be very successful as a starting point to discuss the physics of real microstructures [35]. The reason is that it retains the most important feature of the electrons: that they are dynamically free to move in only two dimensions. The details left out of this simple model, which are associated with the confinement in the third direction, are not very important for studying transport properties. Of course, there are some particular situations where a many-body description is necessary which we do not discuss in this thesis.

Some basic concepts associated with 2DEG are presented here. We find out what the peculiar features the electrons have due to the reduced dimensionality

and the geometrical confinement of microstructures. Particular attention will be payed to a simple example, *i.e.* the quasi-one-dimensional (Q1D) BQW which is dynamically 1D with the length shorter than the electron mean free path. The BQW will be used later as the system in which we study the IIQHE. Different types of electric confinement, as well as the Coulomb interactions between the electrons, will be briefly discussed. At the end, further confinement produced by an external perpendicular magnetic field will also be considered.

2.2 The effective mass approximation and 2D features of a 2DEG

It is convenient to describe some of the characteristics of quantum mechanical wavefunctions in the terms of classical mechanics. Some classical concepts, such as group velocity and mass, can be extended. To build up the relationships between these quantities in the two pictures, we normally use de Broglie waves of electron to construct a quantum wave packet which behaves like a classical particle. In a lattice, Bloch waves are used instead of de Broglie waves. Correspondingly, some classical concepts are therefore meaningful in the quantum case. The group velocity of a wave packet $\mathbf{v}$ and its effective mass m^* are

$$\mathbf{v_k} = \frac{1}{\hbar}\nabla_{\mathbf{k}} E(\mathbf{k}) \tag{2.1}$$

and

$$m_j^* = \frac{\hbar^2}{\left(\dfrac{\partial^2 E}{\partial {k_j}^2}\right)}, \quad j = x, y, z \tag{2.2}$$

where $E(\mathbf{k})$ is the energy of a packet with momentum $\mathbf{k}$. Since these results do not contain any restrictions on the construction of the wave packet, they can further be extended into general situations. In the **effective mass approximation**, the effective mass m_j^* in Eq. (2.2) is assumed to be constant. If a lattice has cubic symmetry, the effective mass is isotropic. It is noticed that this approximation suits the situations where there is only one conduction band. Otherwise, different effective masses should be used for each conduction

band. It may be questionable whether this approximation is appropriate in the case when there are only a few atomic layers in one or more directions. As is often the case, the approximation turns out to be rather good. Nevertheless, it loses validity for monolayer structures. Approximations that take account of the discrete atomic structures are then required [38]. In this thesis, the effective mass approximation will be used because it has been proven to be a good approximation to 2DEGs [35].

The one-electron Hamiltonian for a 2DEG which is dynamically free in the x-y plane is

$$\mathcal{H} = \frac{\mathbf{p}^2}{2m^*} + V(z) \tag{2.3}$$

where $\mathbf{p} = -i\hbar\nabla$ and $V(z)$ is the confinement potential in the z direction. To determine the eigenfunctions of $\mathcal{H}$, we consider a macroscopic square of side L in the x-y plane and apply periodic boundary conditions in both the x and y directions. Since the $\mathcal{H}$ is independent of x and y, the eigenfunctions take the plane-wave form

$$\psi_{\alpha\mathbf{k}}(\mathbf{r}, z) = \frac{1}{L} e^{i\mathbf{k}\cdot\mathbf{r}} \phi_\alpha(z) \tag{2.4}$$

where $\mathbf{r} = (x, y)$ and $\mathbf{k} = (k_x, k_y)$ with both k_x and k_y equal to integer multiples of $2\pi/L$. By substituting the Eq. (2.4) into the Eq. (2.3), we find that the eigenvalue associated with $\psi_{\alpha\mathbf{k}}$ is

$$E_\alpha(\mathbf{k}) = E_\alpha + \frac{\hbar^2 k^2}{2m^*} \tag{2.5}$$

where E_α and $\phi_\alpha(z)$ are determined by the 1D Schrödinger equation

$$-\frac{\hbar^2}{2m^*}\frac{d^2\phi_\alpha(z)}{dz^2} + V(z)\phi_\alpha(z) = E_\alpha\phi_\alpha(z) \tag{2.6}$$

and $k^2 = k_x^2 + k_y^2$. In general, the value of $\mathbf{k}$ may be taken to be continuous, reflecting the macroscopic size of the 2DEG in the x-y plane. The index α which labels the solutions of Eq. (2.6) takes positive integer values.

We see clearly from Eq. (2.5) that the energy spectrum of the 2DEG consists of **2D subbands** which are distinguished by the index α. Each E_α defines the minimum of a subband upon which a continuous parabola is built from the x and y components of the 2D wavevector $\mathbf{k}$. This is different from the

familiar 3D energy spectrum where there is only one continuous parabola from $E = 0$ upwards. The gaps between the subband minima increase when the confinement potential $V(z)$ is narrowed. As an example, let us consider a square well potential of width L_z

$$V(z) = \begin{cases} 0 & 0 < z < L_z, \\ \infty & \text{otherwise.} \end{cases} \tag{2.7}$$

Solving Eq. (2.6), $\phi_\alpha(z)$ and E_α are

$$\phi_\alpha(z) = \left(\frac{2}{L_z}\right)^{1/2} \sin\left(\frac{\alpha\pi z}{L_z}\right), \tag{2.8}$$

$$E_\alpha = \frac{\hbar^2}{2m^*}\left(\frac{\alpha\pi}{L_z}\right)^2. \tag{2.9}$$

When the width L_z is of the order of the electron Fermi wavelength $\lambda_F = 1/k_F$, the Fermi energy $E_F \sim E_{\alpha=1}$. The effect of the energy quantisation then becomes important and the system will have distinguishable 2D features as we will see later. On the other hand, when $L_z \to \infty$, the 3D features of the wavefunctions and the energy spectrum are restored, as E_α in Eq. (2.9) becomes quasi-continuous.

In addition to the energy quantisation, the density of states of the 2DEG, which is shown in Fig. 2.1, has the unique "stair-case" structure

$$\begin{aligned} \rho(E) &= 2\sum_\alpha N_\alpha(E) \\ &= 2\sum_\alpha \theta(E - E_\alpha)\left(\frac{L}{2\pi}\right)^2 \oint \frac{dl}{|\nabla_{\mathbf{k}} E_\alpha(\mathbf{k})|} \\ &= L^2 N_{ssb} \sum_\alpha \theta(E - E_\alpha) \end{aligned} \tag{2.10}$$

where the factor 2 is for electron spin degeneracy, $\theta(E)$ is the unit step function and $N_{ssb} = m^*/\pi\hbar^2$ is the density of states for a single subband per unit area. When only the lowest subband is occupied, as is usually the case for a real 2DEG, the density of states is constant which the behaviour normally associates with a strictly 2D system. As the width of the confinement at the z direction becomes larger, the energy gaps between the 2D subbands are decreased and more and more subbands are occupied. When the $L_z \gg \lambda_F$, many subbands

are occupied. Therefore, the 3D character of the density of states, $\rho(E) \sim E^{1/2}$, is observable as the envelope of $\rho(E)$ because $E_\alpha \sim \alpha^2$. In the limit $L_z \to \infty$, $\rho(E)$ will return to the familiar 3D continuous form $\sim E^{1/2}$.

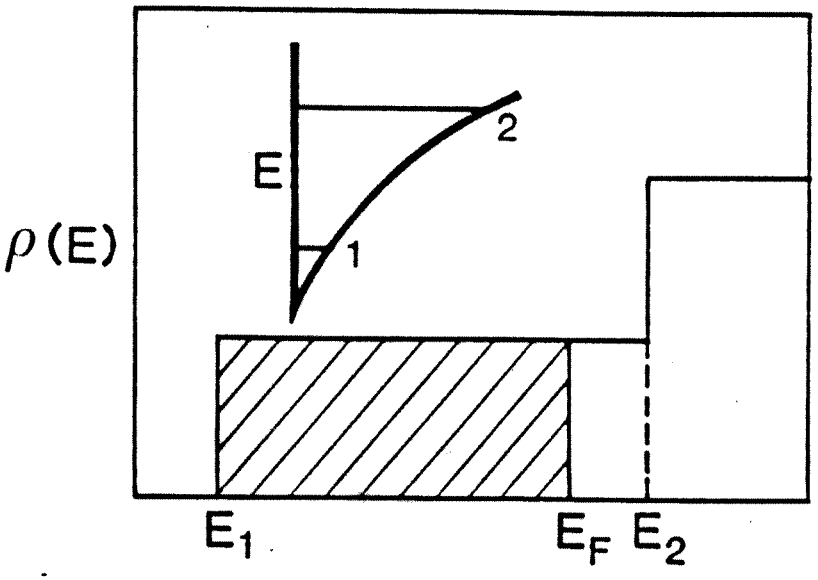

Figure 2.1: Quasi-2D density of states $\rho(E)$ as a function of energy with only the lowest 2D subband occupied (hatched). Insert: Confinement potential perpendicular to the plane of the 2DEG. (From Ref. [39])

2.3 A 2DEG in a BQW and Coulomb interactions between the electrons

In a BQW, a 2DEG in the x-y plane is further dimensionally reduced to a Q1D-EG. A lateral confinement potential, which is normally applied by split-gate electrodes, shapes the 2DEG into a desired geometry. Assuming that this new confinement is in the y direction and is described by a potential function $U(y)$, the electrons are only free to move in the x direction. The electron wavefunction $\psi_{\alpha \mathbf{k}}$ in Eq. (2.4) becomes

$$\psi_{\alpha k_x}(x,y,z) = \frac{1}{L^{1/2}} e^{ik_x x} \varphi_\alpha(y,z) \tag{2.11}$$

and the corresponding eigenvalue is

$$E_\alpha(k_x) = E_\alpha + \frac{\hbar^2 k_x^2}{2m^*} \tag{2.12}$$

where $\varphi_\alpha(y,z)$ and E_α are determined by the 2D Schrödinger equation

$$-\frac{\hbar^2}{2m^*}\left(\frac{\partial^2}{\partial y^2}+\frac{\partial^2}{\partial z^2}\right)\varphi_\alpha(y,z)+[U(y)+V(z)]\varphi_\alpha(z)=E_\alpha\varphi_\alpha(y,z). \tag{2.13}$$

Since the confinement potentials $U(y)$ and $V(z)$ are independent to each other, the eigenfunction $\varphi_\alpha(y,z)$ may take the form

$$\varphi_\alpha(y,z) = \chi_\beta(y)\phi_\gamma(z) \tag{2.14}$$

and correspondingly

$$E_\alpha = E_\beta + E_\gamma \tag{2.15}$$

where $\alpha = (\beta,\gamma)$ with $\beta,\gamma = 1,2,\cdots$. E_β and E_γ are normally discrete and are determined by $U(y)$ and $V(z)$ respectively. When $U(y)$ takes the form shown in Eq. (2.7), E_β will have the same form as in Eq. (2.9) and depends on the size of the microstructure. We see that a BQW with a different size will have a different set of the electron energy levels. This phenomena is known as the **quantum size effect** which has the same physical origin as the spatial quantisation effect which we mentioned before. The eigenvalues in Eq. (2.12) can still be classified as subbands labelled by an index α with a minimum energy E_α for each subband. Because the size of the confinement in the y direction is normally much larger than that in the z direction, the number of the discrete levels E_β is much bigger than the number of E_γ in any energy range. To be clear, we refer to the parts associated with E_β as **1D subbands** which are normally formed within one 2D subband ($E_{\gamma=1}$ in real experimental situations when $L_z \sim \lambda_F$). In addition, the pattern of the density of states has another qualitative change associated with the further reduction of dimensionality. By using the same method in Eq. (2.10), the Q1D density of states is

$$\begin{aligned}\rho(E) &= 2\sum_\alpha N_\alpha(E)\\ &= 2\sum_\alpha \theta(E-E_\alpha)\left(\frac{L}{2\pi}\right)\frac{2}{|\nabla_{k_x}E_\alpha(k_x)|}\\ &= L\left(\frac{2N_{ssb}}{\pi}\right)^{1/2}\sum_\alpha\frac{\theta(E-E_\alpha)}{(E-E_\alpha)^{1/2}}\end{aligned} \tag{2.16}$$

as shown in Fig. 2.2. The most noticeable feature here is that there is a square root singularity at the bottom of each 1D subband. It is expected that much sharper discontinuities will be associated with the 1D case than with the 2DEG and that the quantum size effect will increase the number of these discontinuities.

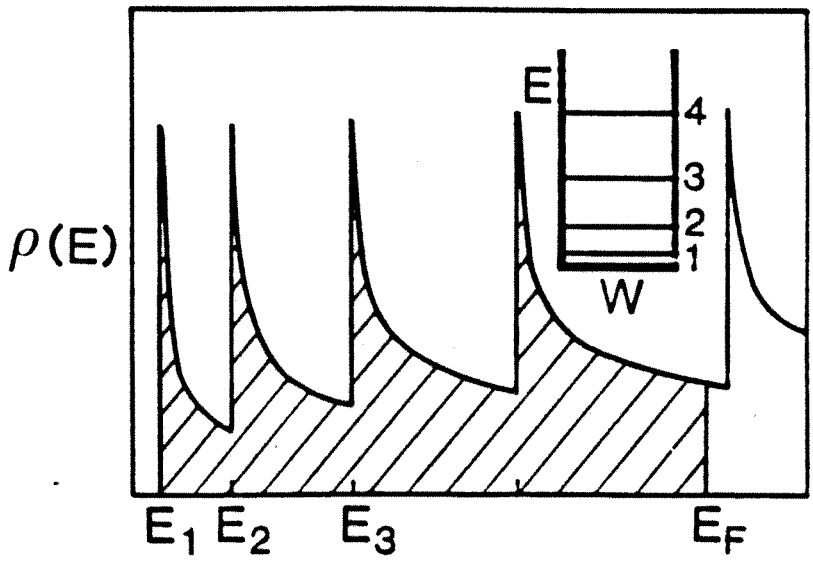

Figure 2.2: Q1D density of states $\rho(E)$ as a function of energy with four 1D subbands occupied (hatched). Insert: Square well lateral confinement potential with discrete energy levels indicating the bottoms of the 1D subbands. (From Ref. [39])

Once we leave the above over-simplified models and begin to study the electron energy spectrum in a real microstructure, calculations become more complicated. Because there are carriers present, the description of the potential and the calculations of the energy level as well as other properties are coupled and must be solved self-consistently. Coulomb interaction between the electrons should be included in order to find out what the charge and potential distributions are. In this case, we should solve the Schrödinger and Poisson equations together. Due to the technical difficulties in solving the non-linear second order partial differential equations, only a few circumstances with sim-

ple geometries can be solved exactly [36]. Variational approximations are the simplest way to obtain approximate solutions, especially for the ground state. The Fang-Howard trial function [37] was widely used. Nowadays, as full numerical solutions become more easily accessible, especially for the 2DEG where equations only involve one space dimension, it is less necessary to rely on variational functions. A brief review of energy level calculations for 2D interacting electrons can be found in Ref. [40].

In a BQW, Schrödinger's equation must be solved in two dimensions with free electron motion only in the third dimension. This problem have been formulated as a set of coupled 1D equations in treating a rectangular GaAs/$Al_xGa_{1-x}As$ wire [41]. Full numerical self-consistent calculations have been done for the electrons in silicon [42] and in GaAs [43, 44]. Normally, only the Hartree approximation is used, the exchange-correlation and image effects are expected to change the results slightly [43]. The calculated confinement potential profiles [43] across a 400 nm BQW along a line 5.6 nm from the GaAs/$Al_xGa_{1-x}As$ interface at 4.2 K are shown in Fig. (2.3). We see from this figure that when the gate voltage $V_g = -1.30$ V ($n_s \sim 2 \times 10^{15}$ m^{-2}) the effective one-electron confinement potential when Coulomb interaction is taken into account is somewhat like a hard wall square well. While, when $V_g = -1.52$ V ($n_s \sim 5 \times 10^{14}$ m^{-2}) the confinement potential behaves rather like a parabolic potential. These numerical simulations for quantum wires in GaAs agree qualitatively with the capacitance experiments [45, 46]. While the external magnetic field have dominant effects on the electron transport properties, it will not change the confinement potential profiles qualitatively [47]. Based on these results, we believe that it is reasonable to use one electron approximation in a hard wall square well as a starting point for our calculations for the IIQHE in a BQW with a certain density of electrons. The parabolic type of confinement potential is an alternative when the electron density is very low.

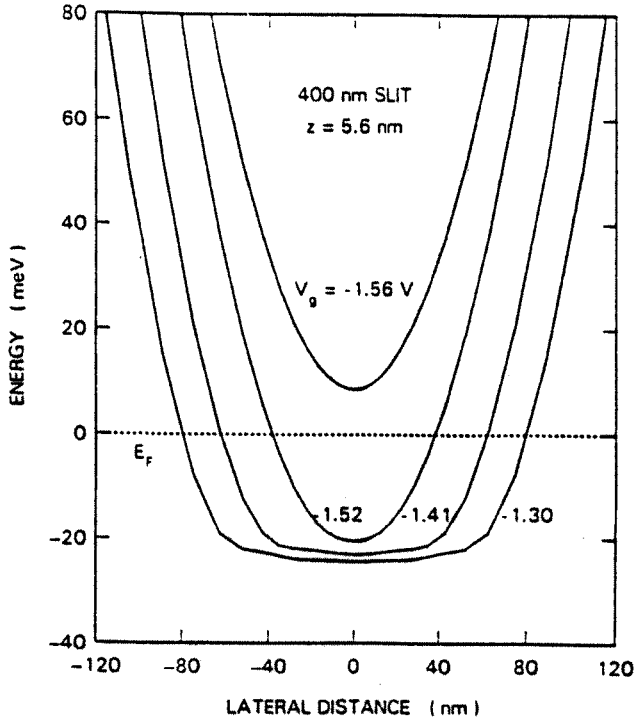

Figure 2.3: Calculated potential profiles at 4.2 K along a line 5.6 nm from the GaAs/$Al_xGa_{1-x}As$ ($x = 0.26$) interface for four values of gate voltage. (From Ref. [43])

2.4 Parabolic potential with magnetic confinement

Let us consider a BQW with the 2DEG in the x-y plane and laterally confined in the y direction by a parabolic potential $U(y)$. This is one of the few models which can be solved exactly. The Hamiltonian for motion in the plane of the 2DEG is

$$\begin{aligned} \mathcal{H} &= \frac{\mathbf{p}^2}{2m^*} + U(y) \\ &= \frac{(p_x^2 + p_y^2)}{2m^*} + q\frac{1}{2}\frac{m^*}{(-e)}\omega_p^2 y^2 \\ &= \frac{p_x^2}{2m^*} + \frac{p_y^2}{2m^*} + \frac{1}{2}m^*\omega_p^2 y^2 \end{aligned} \tag{2.17}$$

where $q = (-e)$ for electrons and the frequency ω_p is used to refer the strength of the lateral confinement. Because the momentum p_x along the BQW commutes

with $\mathcal{H}$, *i.e.* $[p_x, \mathcal{H}] = 0$, we can diagonalise both of them simultaneously. For each eigenvalue $\hbar k_x$ of p_x, the Hamiltonian has discrete energy levels $E_n(k_x)$ $(n = 0, 1, \cdots)$ with the corresponding wavefunctions taking the form

$$\psi_{n,k_x} = \frac{1}{L^{1/2}} e^{ik_x x} \chi_{n,k_x}(y) \tag{2.18}$$

In waveguide terminology, the index n labels the **modes** (or the **channels** as in the language of electronic transport) and the dependence of the energy $E_n(k_x)$ on the wave number k_x is the **dispersion curve** of the n-th mode. The wavefunction ψ_{n,k_x} is the product of a transverse profile $\chi_{n,k_x}(y)$ and a longitudinal plane wave $e^{ik_x x}$. $\chi_{n,k_x}(y)$ and $E_n(k_x)$ are determined by the following Schrödinger equation

$$-\frac{\hbar^2}{2m^*}\frac{\partial^2 \chi_{n,k_x}(y)}{\partial y^2} + \frac{1}{2}m^*\omega_p^2 y^2 \chi_{n,k_x}(y) = E_n(k_x)\chi_{n,k_x}(y). \tag{2.19}$$

The eigenfunctions of the Eq. (2.18) are

$$\chi_{n,k_x}(y) = \frac{1}{(2^n n! \pi^{1/2})^{1/2}} H_n(\xi) \tag{2.20}$$

with the eigenvalues

$$E_n(k_x) = \hbar\omega_p\left(n + \frac{1}{2}\right) + \frac{\hbar^2 k_x^2}{2m^*} \tag{2.21}$$

where H_n is the n-th order Hermite polynomial and $\xi = (m^*\omega_p/\hbar)^{1/2} y$. From Eq. (2.21), we see the familiar 1D subbands again with the spacing $\hbar\omega_p$. The group velocity defined in Eq. (2.1) is equal to the velocity $\hbar k_x/m^*$ obtained from the momentum, and the effective mass is simply m^* for the free 2DEG.

Next, we look at the effect of a perpendicular magnetic field B in z direction on a free 2DEG. Again only equilibrium state is concerned. In the Landau gauge $\mathbf{A} = (-By, 0, 0)$, the Hamiltonian has the form

$$\begin{aligned} \mathcal{H} &= \frac{1}{2m^*}(\mathbf{p} - q\mathbf{A})^2 + U(y) \\ &= \frac{1}{2m^*}(p_x - eBy)^2 + \frac{p_y^2}{2m^*} \end{aligned} \tag{2.22}$$

for a single spin component. Still we have $[p_x, \mathcal{H}] = 0$ and the wavefunctions has the same form of Eq. (2.18). After we put the wavefunctions into the

Eq. (2.17), we get the differential equation which is mathematically equivalent to the Eq. (2.19). This tells us that the magnetic field provides a special type of parabolic confinement (with different potential minima for electrons with different momenta). The solution $\chi_{n,k_x}(y)$ has the same form as in Eq. (2.20) with $\xi = y/l_c - l_c k_x$ and $E_n(k_x) = E_n = \hbar\omega_c(n + 1/2)$. Here, $l_c = (\hbar/eB)^{1/2}$ is the **magnetic length** and $\omega_c = eB/m^*$ is the **cyclotron frequency**. In this particular case, $E_n(k_x)$ does not depend on k_x and we only have the **Landau levels** E_n instead of the 1D subbands. Because there is only magnetic confinement, the group velocity is zero and all the electrons are localised with an infinite effective mass.

The mathematical similarity between parabolic and magnetic confinement allows us to get an exact solution for the parabolic confined BQW in a perpendicular magnetic field B [48]. Using the same gauge, coordinates and notations, we have the same solutions for $\chi_{n,k_x}(y)$ as in the Eq. (2.20) with the $\xi = (1+\gamma)^{1/4}y/l_c - l_c k_x/(1+\gamma)^{3/4}$, where $\gamma = (\omega_p/\omega_c)^2$. While $E_n(k_x)$ has the similar form to that in the Eq. (2.21)

$$E_n(k_x) = \hbar\omega\left(n + \frac{1}{2}\right) + \frac{\hbar^2 k_x^2}{2M} \tag{2.23}$$

where $\omega^2 = \omega_p^2 + \omega_c^2$ and $M = (1+\gamma)m^*/\gamma$. The effective mass M here is $(1+\gamma)/\gamma$ times heavier and the group velocity $\hbar k_x/M$ is then$\gamma/(1+\gamma)$ smaller than that in the free 2DEG case. The electrons no longer behave in the same way as they do when there is only electrostatic parabolic confinement, because the momentum contains an extra contribution from the magnetic vector potential. On the other hand, unlike the case when there is only magnetic field, the electrons are no longer localised since they are delocalised from their static cyclotron motions when they are scattered by the confinement potential.

The correspondence between the electron wavefunction in a magnetic field and its classical trajectory may help us to understand more about the nature of the quantum wavefunction [49]. It is less confusing to look at a 2DEG in a magnetic field confined by a hard wall square well because the edges are well defined. We will follow Ref. [39] to demonstrate this correspondence and more details can be found there.

Let us assume the edges of a square well confined BQW are at $y = \pm W/2$. An exact quantum mechanical solution of this problem is given in Appendix A. In the classical picture, the electron position (x, y) is on a circle with centre coordinates (X, Y) can be expressed in terms of its velocity $\mathbf{v}$ by

$$x = X + \frac{v_y}{\omega_c}, \quad y = Y - \frac{v_x}{\omega_c} \tag{2.24}$$

and the electron energy $E = m^* v^2/2 = m^* \omega_c^2 r_c^2/2$ with the cyclotron radius $r_c = (2m^* E)^{1/2}/eB$. Both the electron energy E and the shift Y of the orbit centre from the edges of the wire are constants of the motion. The shift Y is related to the electron momentum k_x, the constant of motion in the quantum mechanical description, as $Y = l_c^2 k_x = \hbar k_x/eB$ (which is identical to the average position of a free 2DEG wavefunction in the magnetic field B with the gauge we choose). On the other hand, the coordinate X along the wire changes on each reflection when the electron is scattered by one of the edges. The trajectory (x, y) can be classified as a cyclotron orbit, a skipping orbit, or a traversing trajectory, depending on whether the trajectory collides with zero, one, or both of the edges of the wire. Using the conditions $(Y \pm W/2) = r_c$, we can separate these three types of trajectories in the space (Y, E) by two parabolas $(Y \pm W/2)^2 = 2m^* E(eB)^{-2}$ as shown in Fig. 2.4.

The quantum mechanical dispersion curves $E_n(k_x)$ can then be fitted into the above classical picture by the correspondence $k_x = YeB/\hbar$. We may apply the Bohr-Sommerfeld quantisation rule to the classical motion in the y direction, *i.e.*

$$\frac{1}{\hbar} \oint p_y dy + \gamma = 2\pi n, \quad n = 1, 2, \cdots \tag{2.25}$$

to find out the dispersion curve with sufficient accuracy for our purpose here. The phase shift γ is the sum of the phase shift at the two turning points of the projected motion along the y direction. The phase shift is π when v_y changes sign by the reflection at the edge and $-\pi/2$ when v_y changes sign continuously. Consequently, γ is $-\pi/2 - \pi/2 = \pi \pmod{2\pi}$ for a cyclotron, $\pi - \pi/2 = \pi/2$ for a skipping orbit, and $\pi + \pi = 0 \pmod{2\pi}$ for a traversing trajectory. By

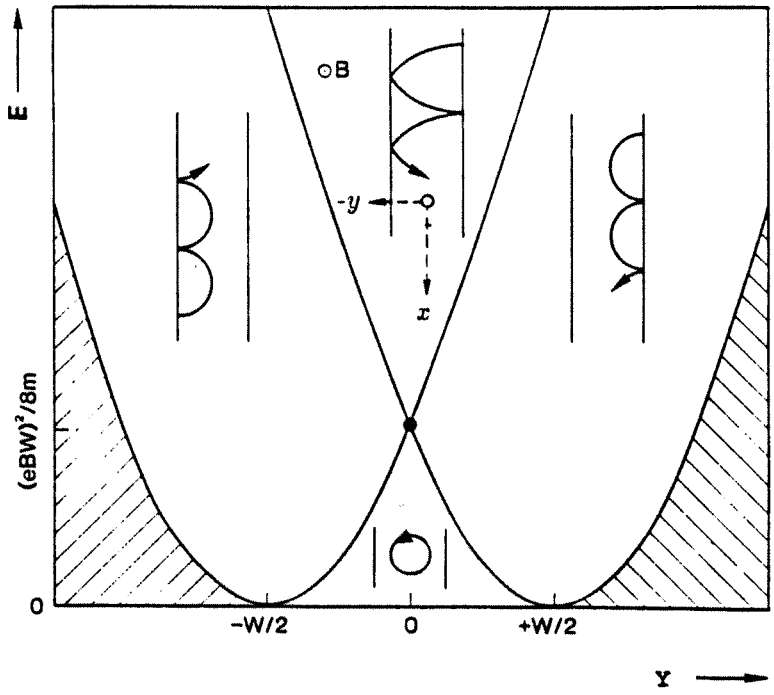

Figure 2.4: Energy-orbit centre phase diagram. Different types of classical trajectories in a magnetic field are shown (clockwise from the left: skipping orbits on one edge, traversing trajectories (only one direction is drawn here), skipping orbits on the other edge and cyclotron orbits). The hatched region is forbidden. (From Ref. [39])

using Eq. (2.24), $p_y = m^* v_y = eB(x - X)$ and Eq. (2.25) takes the form

$$B \oint (x - Y) dy = \frac{e}{h} \left(n - \frac{\gamma}{2\pi} \right). \tag{2.26}$$

This quantisation condition has a geometrical interpretation: $n - \gamma/2\pi$ flux quanta h/e are contained in the area bounded by the wire edges and a cyclotron circle centred at Y with radius $(2m^*E)^{1/2}/eB$. The electron energy $E = m^* v^2/2$ will be calculated with the aid of Eqs. (2.24) and (2.26). The dispersion curve for $E_n(k_x)$ can then be carried out straight forwardly for each integer n and momentum Y by using the relation $k_x = YeB/\hbar$. The results are shown in Fig. 2.5. The regions occupied by the classical skipping orbits are shaded, which are bounded by the two parabolas shown in Fig. 2.4. The unshaded regions contain cyclotron orbits at small E and traversing trajecto-

ries at larger E. From Fig. 2.5, we can easily see the correspondences between these classical trajectories and the parts on the quantum dispersion curves. The cyclotron orbits correspond to the Landau levels which are the flat portions of the dispersion curve at $E_n = (n - 1/2)\hbar\omega_c$. The group velocity is zero for a Landau level, which is identified with a circular orbit. The traversing trajectories, which interact with both the opposite edges and have a nonzero group velocity, correspond to the 1D subbands where both the electrostatic confinement and the magnetic field are present. The skipping orbits correspond to the **edge states** [50], which interact with a single edge only. The two sets of the edge states (one for each edge) are separated in the (k, E) space. Edge states at opposite boundaries move in opposite directions, which is the same as for the skipping orbits. Finally, the critical field $B_{\text{crit}} = 2\hbar k_F/eW$ in Fig. 2.5 is obtained from the requirement of having the BQW width equal to the classical cyclotron diameter. There are traversing trajectories only when $B < B_{\text{crit}}$.

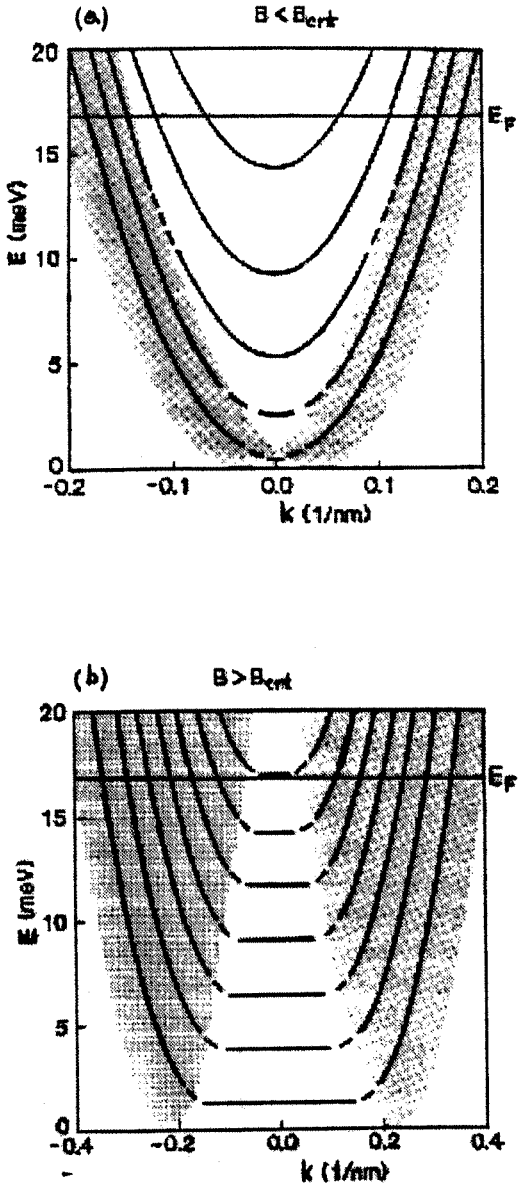

Figure 2.5: Dispersion curves $E_n(k_x)$. (a) $W = 100$ nm, $B = 1$ T; (b) $W = 200$ nm, $B = 1.5$ T. The shaded area is the region of classical skipping orbits and $B_{\text{crit}} = 2\hbar k_F/eW$. (From Ref. [39])

Chapter 3

Electronic transport: Landauer-Buttiker formulae

3.1 Introduction

Transport in a system is a phenomenon associated with a non-equilibrium state. A system is in a **non-equilibrium** state if there are any kind of "potential" differences between any two spatial points in it so that a "flow" is built up from a source to a drain which are associated with the high and low "potentials" respectively. The dependence of the amount of the "flow" on the "potential" difference is generally nonlinear. Because of the difficulty of dealing with the nonlinearity there is no unified theoretical approach to non-equilibrium systems. Only the so-called **near-equilibrium** systems have been systematically studied in a unified picture [51]. In a near-equilibrium system, the difference between the "potential" μ_s at the source and the "potential" μ_d at the drain is so small that the "flow" can be treated as a **linear response** of it. We would like to use $2(\mu_s - \mu_d)/(\mu_s + \mu_d) \to 0$ as the criterion of near-equilibrium instead of the conventional $(\mu_s - \mu_d) \to 0$, since we believe any system in which $\mu_s > \mu_d = 0$ is far from equilibrium. In fact, a system is in a near-equilibrium state only if the amount of net current is much smaller than both of the currents from source and drain.

There are different kinds of flows, such as charge, heat, mass, etc., corre-

sponding to different kinds of potential differences. Current, *i.e.* the charge flow, is induced by the electrochemical potential differences in a system. The ratio of the potential difference to the current is defined as the resistance between the two corresponding points in the system as in the well known Ohm's law. While the ratio of the change of the potential difference to the change of the current is known as the differential resistance. It is understandable that these two kinds of resistances are generally not equal to each other and that both of their magnitudes depend not only on the average chemical potential in a system but also on the potential difference. If a system is in the near-equilibrium regime, the linearity of electronic transport will merge these two resistances into one constant which depends only on the chemical potential of the system and can be used to characterise the system response. This is the resistance we are going to study in 2DEG microstructures in this thesis.

Resistance comes from the disturbance produced by different kinds of "impurities" on the directed motion of the charge carriers which are the electrons in solid state materials. We can see this from a simple classical example. In a 2D infinite space without any impurities the current density $\mathbf{j}$ will approach infinity because the infinite velocity of free electrons which are accelerated by a constant electric field $\mathbf{E}$. Hence, the resistivity ρ defined by $\mathbf{E} = \rho\mathbf{j}$ must approach zero. On the other hand, the electron velocity and the corresponding current density cannot be arbitrarily large as long as there is an impurity distribution in the system because there is always some momentum loss associated with scattering. It is very obvious that a classical resistance problem is very similar to a classical diffusion problem. The concepts of the **mean free path** l and the **relaxation time** τ have been borrowed from there. They refer to the average distance and time respectively between two electron-impurity scattering events. The resistivity may be found easily [52] as $\rho = m^*/ne^2\tau$, where m^* is the electron mass and n is the density of electrons. More detail calculations can be performed by using a distribution function $f(\mathbf{r}, \mathbf{p}, t)$ which expresses the fraction of states occupied and its time dependence, where $\mathbf{r}$ and $\mathbf{k}$ are the electron position and momentum respectively. If we imagine f as the

density of a fluid in 6-dimensional $(\mathbf{r}, \mathbf{p})$ space, the equation of continuity has the form

$$\frac{\partial f}{\partial t} + \nabla \cdot (f\mathbf{V}) = 0 \tag{3.1}$$

where V is a 6-dimensional velocity composed of the electron velocity $\mathbf{v} = \partial\mathbf{r}/\partial t$ and the force on electrons $\mathbf{F} = \partial\mathbf{p}/\partial t$. Because $\mathbf{r}$ and $\mathbf{p}$ are conjugate coordinates and the Hamiltonian equations held for them, we will have $\nabla \cdot \mathbf{V} = 0$ and

$$\frac{df}{dt} = \frac{\partial f}{\partial t} + \mathbf{v} \cdot \nabla_{\mathbf{r}} f + \mathbf{F} \cdot \nabla_{\mathbf{p}} f = 0 \tag{3.2}$$

by the Liouville's theorem [53]. In the presence of impurities, electrons being scattered in the $\mathbf{p}$-space can not be fully described by the force $\mathbf{F}$ and a supplement term to include the effect of scatterings is needed. Using the relation $\mathbf{p} = \hbar\mathbf{k}$, we have the **Boltzmann equation** in the form

$$\frac{df}{dt} = \frac{\partial f}{\partial t} + \mathbf{v} \cdot \nabla_{\mathbf{r}} f + \frac{\partial \mathbf{k}}{\partial t} \cdot \nabla_{\mathbf{k}} f = \left(\frac{df}{dt}\right)_{\text{scatterings}} \tag{3.3}$$

where the right-hand side is the time rate of change due to the scattering by impurities. To solve Eq. (3.3), a **relaxation time approximation** is often used [55], which is

$$\left(\frac{df}{dt}\right)_{\text{scatterings}} = -\frac{f - f_0}{\tau}. \tag{3.4}$$

where f_0 is the equilibrium distribution function. For a simple homogeneous system at low temperatures with randomly located impurities: $f = f(\mathbf{k})$ for the steady state. Then we have the resistivity in the same form, $\rho = m^*/ne^2\tau(k_F)$, for a free EG [36], where $\tau(k_F)$ is the relaxation time for the electron at the Fermi level. The Boltzmann equation is derived from the classical point of view [54]. In principle, the Boltzmann equation may only be used when wave packets can be constructed. Nevertheless, it sometimes produces similar answers as a quantum calculation even when this criterion is not satisfied.

Electronic transport in microstructures is a kind of quantum transport because the Fermi wavelength is of the order of the microstructure dimensions. Furthermore, the time for electrons traversing the system is equal or less than the relaxation time in common semiconductors (typical values are velocity for electrons in semiconductors 10^5 m/s [39], the relaxation relaxation time

$10^{-13} - 10^{-11}$ s [39] and size of microstructures $10^{-8} - 10^{-7}$ m). For such cases, we need quantum mechanics to discuss near-equilibrium systems. A general formula for the quantum mechanical linear response was first derived in 1957 [56], which is known as the **Kubo formula**. The great generality of this approach makes specific calculations very difficult even in the cases which are easily handled by means of the Boltzmann equation [57]. To use this formula to calculate the resistivity, various techniques based on density matrix, Wigner functions, Feynman path integrals and Green's functions have been developed for different applications. All these techniques have their computational strengths and weaknesses, and all are equivalent representations of the quantum transport. A brief review for each of these techniques can be found in Ref. [58]. To study quantum electronic transport in microstructures, the Landauer-Büttiker formulae (L-B formulae) are the most frequently used because they directly give the quantities measured at the terminal of the structure. These formulae express the relations between the resistance and the scattering matrix of a microstructure. In the following sections, we will look at the original classical Landauer formula, its quantum form, the quantum L-B formulae and, finally, a special feature associated with the L-B formulae — contact resistance. A detailed review about the Landauer formula, the L-B formulae and relevant problems is in Ref. [59], where a derivation of the L-B formula from linear response theory is also included.

3.2 Classical and quantum forms of the Landauer formula

The original Landauer formula [60] was introduced in the same year as the Kubo formula was obtained. It took a novel point of view that transport should be viewed as a consequence of incident carrier flux [61]. This made it the most useful formalism for the study of the electronic resistance in microstructures for which the system size is comparable with the electron Fermi wavelength. The Landauer formula was first derived by using the analogue to a classical diffusion

problem. Although this formula has a classical origin, the nonlinearity and irreversibility associated with the electron wave character and phase coherence of electrons were discussed by analysing the relation between the transmission probabilities of the whole system and its individual parts. Below we give a derivation of the Landauer formula based on his 1970's paper [62].

Landauer considered electrons incident on an array of obstacles. The length of the array is L and the transmission and reflection probabilities for the whole array are T and $R = 1 - T$ respectively. Hence, the density gradient across the array is $\nabla n = -2R/L$ for a unit incident flux. The current of particles associated with this gradient is $j = vT$, where v is the electron velocity in the absence of scatterers. Using the diffusion equation $j = -D\nabla n$, the diffusion coefficient D is

$$D = \frac{vL}{2}\frac{T}{R}. \tag{3.5}$$

Then, the corresponding resistivity ρ can be carried out through the Einstein relation [63]:

$$\frac{1}{\rho} = \frac{e^2 D}{\left(\frac{\partial \mu}{\partial n}\right)_T} = \frac{e^2 vL}{2\left(\frac{\partial \mu}{\partial n}\right)_T}\frac{T}{R} \tag{3.6}$$

where μ is the chemical potential for a density of n electrons. The total resistance of the array, Ω, is:

$$\Omega = \rho L = \frac{2}{e^2 v}\left(\frac{\partial \mu}{\partial n}\right)_T \frac{R}{T}. \tag{3.7}$$

Eq. (3.7) is known as the **Landauer formula.** There is no contradiction to our naive understanding of resistance, for a perfect conductor $R \to 0$ and $\Omega \to 0$ while for an insulator $T \to 0$ and $\Omega \to \infty$. Resistance additivity is retained in classical situation. If the whole array consists of N identical classical obstacles, we will have $R/T = Nr/t$ [62] where r and t are the transmission and reflection probabilities for one obstacle. But, the resistance of the system can be expressed in the terms of the transmission and reflection probabilities of the whole system and does not depend directly on the length of the system. If electrons can keep their phase memory when they traverse between two adjacent obstacles, the ratio of the total reflection and transmission probabilities is not a linear

combination of the individual ratios. This is the case when system dimensions are smaller than the phase coherence length of the system. The resistance of such a system is nonlocal because of both the electron wave character and phase memory. From this point, we may realise that the global "ances" are more fundamental than the local "ivities" in phase coherent systems. Moreover, the resistance of a phase coherent system has generally no irreversibility unless the system itself has some kinds of intrinsic symmetries.

In 1980, the Landauer formula was obtained again through quantum mechanics approach [64]. The system is the same, an 1D obstacles array with its two ends connected with two electron reservoirs. The chemical potential difference between the two reservoirs is $\delta\mu$. The phases of the electrons coming out of the reservoirs are randomised. The incoming current from the source (drain) to the system is I_s (I_d), and the reflected current from the system to the source (drain) is I'_s (I'_d). We can use the transmission and the reflection probabilities, T and R, to express the reflected currents in terms of the incoming currents

$$I'_s = RI_s + TI_d, \quad I'_d = TI_s + RI_d. \tag{3.8}$$

The extra density of electrons in the energy space near the Fermi surface is

$$\delta n = \frac{\delta\mu}{\left(\frac{dE}{dn}\right)_{E_F}} \tag{3.9}$$

which is equal to

$$\delta n = \frac{I_s + I'_s}{(-e)v_s} - \frac{I_d + I'_d}{(-e)v_d} = \frac{2R}{(-e)v_F}(I_s - I_d) \tag{3.10}$$

where the electron group velocities from the source and drain, v_s and v_d, are equal to the electron Fermi velocity v_F because the chemical potential difference $\delta\mu$ is very small. The net current traversing the system is

$$I = I_s - I'_s = -(I_d - I'_d) = T(I_s - I_d). \tag{3.11}$$

A very important and unique quantum feature of a dynamically 1D-EG is that the product of its Fermi velocity and the density of states at the Fermi energy is a constant which is

$$v_F \left(\frac{dn}{dE}\right)_{E_F} = \frac{4}{h} \tag{3.12}$$

with spin degeneracy included. With the aid of this relation, the conductance of the system can be written in the form

$$\begin{aligned} G &= \frac{I}{\delta\mu/(-e)} \\ &= \frac{e^2}{2}\frac{v_F}{\left(\frac{dE}{dn}\right)_{E_F}}\frac{T}{R} \\ &= \frac{2e^2}{h}\frac{T}{R}. \end{aligned} \tag{3.13}$$

Now, we may look back to Eq. (3.7) and find that we can directly use the quantum relation between the 1D group velocity and density of states and get the identical final result.

Eq. (3.13) was employed in a rigorous formulation of a new scaling theory of localisation [64, 65]. However, this approach was a complete success only in the strictly 1D case and had little impact on experimental work on quantum transport phenomena. To calculate the conductance of a real system, we should generalise it to higher dimensions where more than one lateral conducting channels are involved. Many attempts were made to reestablish Eq. (3.13) and propose the multi-channel generalisations of it in either approximated or rigorous manner by different approaches (including the sophisticated self-consistent linear response theory) [64, 66, 67, 68, 69]. But, there appeared to be no unique generalisation and the final form depended entirely on the assumption made deliberately, or used unconsciously, about the nature of the measurement leads. What kind of role these leads played in the experimental resistance measurements remained a problem. There was a detailed examination of the effect of the measurement methods [70]. Four-lead configurations and current-stop procedures for measuring voltage were both simulated by using a scattering matrix. This work recognises the importance of considering the actual physical conditions corresponding to a measurement and is vital to the study of the transport properties of microstructures. The authors rederived Eq. (3.13) but missed a new formula which will be given in the next section. This was partly because the voltage leads were assumed to couple to the system very weakly and partly because the Landauer formula was apparently and essentially correct so that everybody wanted to keep it.

3.3 The single-channel and multi-channel L-B formulae

In 1981, another form of conductance formula in strictly 1D quantum limit [71] was obtained:

$$G = \frac{2e^2}{h}T. \tag{3.14}$$

A short time later, a generalisation of Eq. (3.14) into the N-channel case was derived exactly for the linear response of a system to an applied field which only varies within the obstacle region [72]. The result is

$$G = \frac{2e^2}{h}\sum_{m,n} T_{mn} \tag{3.15}$$

where the subscripts m and n run over all the N-channels on the two sides of a system respectively. $T_{mn} = |t_{mn}|^2$ is the transmission probability of an incoming electron wave from the n-th channel of one side into the m-th channel of the other side and t_{mn} is the corresponding element of the system transmission matrix. It is obvious that Eq. (3.14) contradicts the Landauer formula Eq. (3.13). From the former equation, we will find that the resistance of any system is not zero even for a "perfect" conductor ($T = 1$ for a complete transmission). This feature was considered to be very puzzling and suspicious by many researchers. But, the only quantitative application of a Landauer-type formula to multi-channel transport at that time was using Eq. (3.15) to test the scaling theory of localisation in 2D and 3D and good agreement with the expected behaviour of scaling function was obtained [73].

The dispute was settled by the work of Büttiker *et al.* [69]. They used a simple 1D picture to show that Eq. (3.13) and Eq. (3.14) have difference physical correspondences. The model they used is shown in Fig. 3.1. The chemical potentials in the reservoirs μ_1 and μ_2 are fixed. However, the chemical potential difference between the two sides of the obstacle array is smaller than the chemical potential difference between the reservoirs due to the non-equilibrium distribution of electrons in the leads. The chemical potential in the lead is defined as the chemical potential that would correspond to the same density of

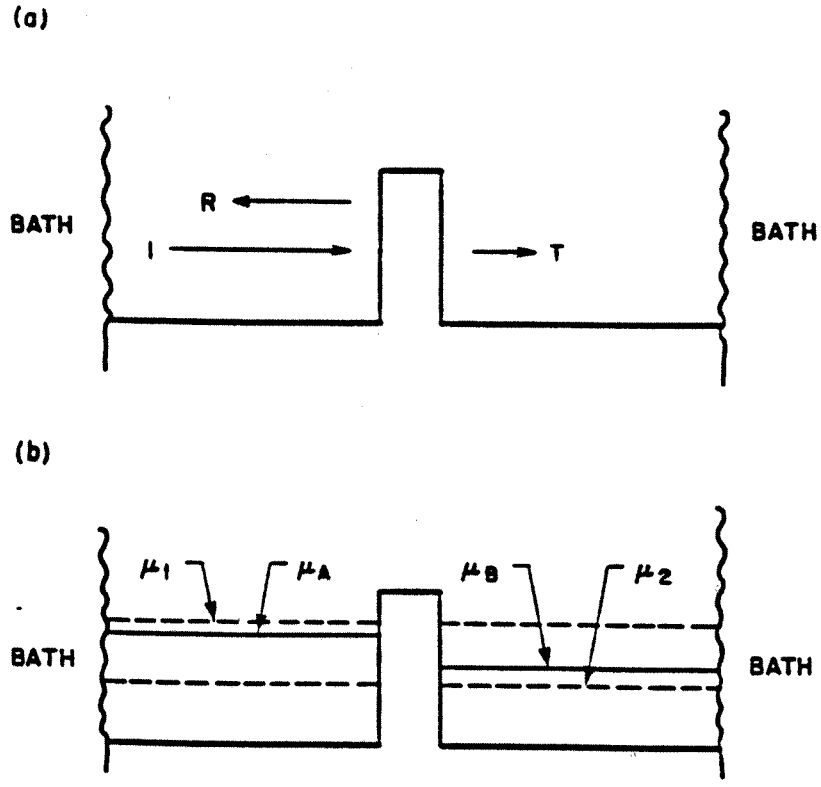

Figure 3.1: (a) An array of obstacles connected to two incoherent reservoirs by ideal 1D conductors. The obstacle array is represented by a potential barrier characterised by transmission and reflection probabilities T and R. (b) The chemical potentials in the single-channel case. The chemical potentials for the source and drain are μ_1 and μ_2 respectively. μ_A and μ_B are two chemical potentials which characterise the electron densities in the two ideal leads. (From Ref. [69])

electrons if they were in equilibrium. $\mu_A(\mu_B)$ can be determined by equalising the number of electron energy states above and below $\mu_A(\mu_B)$ for the states between μ_1 and μ_2 at the left(right)-hand side of the obstacle array. When the system is in the near-equilibrium state, with the aid of the very helpful relation Eq. (3.12) the total net current I has the form

$$I = \frac{2(-e)}{h} T(\mu_1 - \mu_2) \tag{3.16}$$

and the chemical potential difference at the two sides of the obstacle array is

$$\mu_A - \mu_B = R(\mu_1 - \mu_2), \tag{3.17}$$

where T and R are the transmission and reflection probabilities of the obstacle array. Therefore, the conductance of the obstacle array itself is determined by the Landauer formula Eq. (3.13) while the conductance of the whole system has the form of Eq. (3.14). Generalisation to the multi-channel cases is made by assuming that all the electrons in different channels arriving from the source and drain to the corresponding leads are characterised by one single chemical potential μ_1 and μ_2 respectively. The chemical potentials in the leads, μ_A and μ_B, are determined through the same procedure as for the single-channel case. The N-channel conductance associated with $\mu_A - \mu_B$ is

$$G = \frac{2e^2}{h} \sum_m T_m \frac{2\sum_m v_m^{-1}}{\sum_m v_m^{-1}(1 + R_m - T_m)} \tag{3.18}$$

where $R_m = \sum_n R_{mn}$, $T_m = \sum_n T_{mn} = 1 - R_m$ and v_m is the Fermi velocity for the m-th channel. The subscripts m and n run over all the N-channels on the two sides of the system respectively. This formula was also obtained in Ref. [68]. While the multi-channel conductance associated with $\mu_1 - \mu_2$ has the form as in Eq. (3.15).

The difference between Eq. (3.13) and Eq. (3.14) can be understood in this way: even in the strictly 1D situation measurement does have significant effect on the final results. These two kinds of formulae will merge into one at the limit of $R \to 1$ ($R_{mn} \to 1$ for the multi-channel case) because the electrons in the leads will approach equilibrium state at this limit. In fact, the convergence can be much more rapid [74] and the condition is $G \ll N(2e^2)/h$

or equivalently $l/L \ll 1$ where N is the number of conducting channels, l is the elastic mean free path and L is the length of a microstructure. In another particular situation, these two formulae will also merge when one of the channel velocity vanishes as the Fermi energy approaches the corresponding channel energy. For example, when E_F approaches E_{N+1} at which the $(N+1)$-th channel becomes conducting, both the corresponding channel velocity v_{N+1} and transmission probability T_{N+1} will approach zero, and Eq. (3.18) for $(N+1)$ channels will reduce to the form of Eq. (3.15) for N channels.

At about the same time, a series of fundamental experiments on the conductance of ultra-small metallic rings revealed the presence of a normal metal Aharonov-Bohm effect [26] and system-specific time-independent magnetoresistance fluctuations [19]. These experiments were primarily carried out in multi-lead configurations and the magnetic asymmetry in the conductance fluctuations due to the phase coherence of electrons completely ruled out the possibility of using the two-lead formula Eq. (3.14) or its multi-channel form Eq. (3.15). The point is that in the two-lead phase coherent system the phase of electrons will be randomised after the electrons traverse the system, so that the length of the system is very similar to the inelastic mean free path in other systems. The two-lead formula can be applied only when the lead spacing is about the inelastic mean free path which is normally not the case in the above multi-lead experiments. A multi-lead multi-channel generalisation is needed. Büttiker extended the scattering matrix description used in Ref. [70] and considered a four-lead system in terms of its transmission and reflection matrices [75]. This four-lead 2DEG system is shown in Fig. 3.2 with an external magnetic field B applied in the direction perpendicular to the plane of the system (which is represented by the magnetic flux Φ in the figure). The chemical potentials of each reservoirs were assumed to be so close that the electrons in the microstructure are in a near-equilibrium state. The important thing is that Büttiker assumed that the voltage leads and the current leads are qualitatively the same as in a real four-lead configuration experiments. The only difference is that they just happen to be used for measuring the voltage and the current respectively.

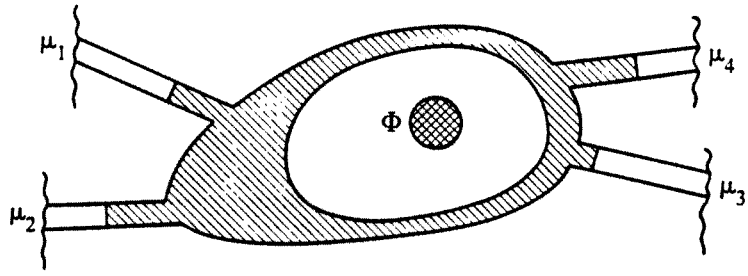

Figure 3.2: A four-lead system connected to four reservoirs via four perfect leads (unshaded). An external magnetic field is applied as represented by the magnetic flux Φ. (From Ref. [75])

Then he evaluated the current flowing into or out each reservoir in the terms of the corresponding chemical potential difference by using the same procedure in two-lead case. For an M-lead system we can write the current in the i-th lead in the terms of the chemical potentials of each reservoirs as

$$I_i = \frac{2(-e)}{h}\left[(N_i - R_{ii})\mu_i - \sum_{j\neq i} T_{ij}\mu_j\right] \tag{3.19}$$

with

$$T_{ij} = \sum_{m,n} T_{ij,mn} \tag{3.20}$$

and

$$R_{ii} = \sum_{m,n} R_{ii,mn} \tag{3.21}$$

where $T_{ij,mn}$ is the transmission probability of a unit incident current in the n-th channel of the j-the lead to the m-th channel of the i-th lead, $R_{ii,mn}$ is the reflection probability in the m-th channel of the i-th lead due to a unit incident current in the n-th channel of the same lead. The subscripts i, j, m and n run from 0 to M, M, N_i and N_j respectively, where M is the total number of leads and $N_i(N_j)$ is the total number of conducting channels in the lead $i(j)$. Using

the current conservation condition

$$N_i = R_{ii} + \sum_{j \neq i} T_{ij}, \tag{3.22}$$

we can express Eq. (3.19) in the form

$$I_i = \sum_j G_{ij} \frac{\mu_j}{(-e)}. = \frac{2e^2}{h} \sum_{j \neq i} T_{ij} \frac{(\mu_i - \mu_j)}{(-e)} \tag{3.23}$$

where G_{ij} is the conductance between the i-th and the j-th leads. If the system is connected only to two reservoirs, Eq. (3.23) yields the two-lead multi-channel conductance G_{12} as in Eq. (3.15). A multi-lead generalisation of Eq. (3.15) can be obtained directly from Eq. (3.23) as

$$G_{ij} = \begin{cases} \dfrac{2e^2}{h} T_{ij}, & i \neq j, \\ \dfrac{2e^2}{h}(N_i - R_{ii}), & i = j. \end{cases} \tag{3.24}$$

Eqs. (3.22) and (3.23) represent a quantum version of the Kirchhoff's law [33, 76]. These equations provide a linear response relationship between the chemical potentials of the electron reservoirs connected to the system and the currents at the connections of the system and the reservoirs. The linear response coefficients in Eq. (3.19), *i.e.* the transmission and reflection probabilities, are evaluated at equilibrium at the Fermi energy and have the Onsager-Casimir symmetry under magnetic field reversal [77, 78]. The diagonal R_{ii} are symmetric under B reversal and the off-diagonal T_{ij} obey a reciprocity relation [75, 80] which is based on the symmetry of the scattering matrix [79],

$$R_{ii}(B) = R_{ii}(-B), \quad T_{ij}(B) = T_{ji}(-B). \tag{3.25}$$

Now, consider a four-lead configuration of conductance measurement. Let the leads k and l be the current source and drain and the leads m and n be the voltage leads. The voltmeter connected to the voltage leads is taken to have infinite impedance. Hence, the voltage measured at a voltage lead is obtained by adjusting the chemical potential of the reservoir connected to this lead such that the net current through the measurement lead is zero. After

solving Eq. (3.19) with the conditions $I = I_k = -I_l$ and $I_m = I_n = 0$, we find the four-lead conductance [75]

$$G_{kl,mn} = \frac{\mu_m - \mu_n}{(-e)I} = \frac{2e^2}{h} \frac{D_{kn}}{T_{mk}T_{nl} - T_{ml}T_{nk}} \tag{3.26}$$

where D_{kn} is a rank 3 subdeterminant of the matrix of transport probabilities in Eq (3.22) with row k and column n deleted from the full matrix. Actually, all these subdeterminants are equal, $D_{kn} = D$, as a consequence of current conservation [33]. The kind of formulae given in Eqs. (3.14), (3.15), (3.24) and (3.26) are known as the **Landauer-Büttiker formulae.** The important symmetry of the four-lead conductance Eq. (3.26) is the reciprocity relation [75, 80],

$$G_{kl,mn}(B) = G_{mn,kl}(-B) \tag{3.27}$$

and $D(B) = D(-B)$, which can be easily verified by applying the reciprocity relations in Eq. (3.25) onto Eqs. (3.22) and (3.26). A derivation of the L-B formula, Eq. (3.24), and the Onsager-Casimir relations Eq. (3.25) can be found in Ref. [81]. (Actually, reciprocity of current sources and voltage sources has been understood for a long time, well before the Onsager-Casimir symmetry was found. As being pointed out by Büttiker [80], Searle presented a derivation of Eq. (3.27) in 1911 [82], which he attributed to Heaviside.)

We see clearly from above that the form of conductance formula has been changed several times to suit different situations. From Eq. (3.7), Eq. (3.13), Eq. (3.18), Eq. (3.15), Eq. (3.24) and, finally, to Eq. (3.26), the corresponding physical background varies in turn from classical 1D system, quantum 1D system, quantum multi-channel system (which dimension is higher than 1D), quantum 1D system with two measurement leads, quantum multi-channel system with multi-leads to quantum multi-channel multi-lead system with the current and voltage leads fixed. In addition to what we have discussed about the electronic transport at zero temperature, we would like to mention that an extension of the L-B formulae has been made to account for temperature changes in the reservoirs and heat flows in the leads [81]. It describes the linear electrical, thermal and thermoelectric transport properties of a microstructure at low

temperatures and near-equilibrium state. Onsager-Casimir symmetry relations and reciprocity theorems are given for all the electrical, thermal and thermoelectric configurations. The advantage of the formalism is that the theory puts the formulae for the thermal and thermoelectric matrices of a multi-lead microstructure on the same footing as those for the conductance matrix.

3.4 Contact resistance

Before we end this chapter, let us explore a special feature associated with the L-B formulae in more detail. For simplicity, we only discuss a two-lead system which is physically the same to a multi-lead case for what concerns us. It is about the finite conductance at the ballistic transport regime for which the transmission probability $T_m = \sum_n T_{mn} \to 1$ in Eq. (3.15) for every conducting channel m. At this limit, the conductance is finite, $G = 2e^2N/h$, where N is the number of conducting channels. When there is only one conducting channel involved, the conductance of the system becomes a universal constant $2e^2/h$. There are various ways of giving a qualitative or even semi-quantitative explanation of this result, emphasising on either the effect of system boundaries or the contact resistance at the contacts between leads and reservoirs.

From what we have discussed in the last section, we understand that the quantised finite conductance of a perfect lead — a BQW — is a kind of phenomena associated with the fact of non-equilibrium in the leads connecting the reservoirs and the obstacle array. Due to the finite width of a BQW, there are only limited conducting channels involved in a finite range of chemical potential differences. In this ballistic transport regime, it is the boundaries which limits the current rather than the obstacles. Quantised finite conductance in a BQW is a result of the quantum size effect associated with the finite width of the wire. If we could make an infinite wide BQW, the number of conducting channels N would approach infinity as well as the conductance. The infinite conductance of a system is associated with its infinite cross section which is always assumed in macroscopic calculations. At this limit, we may restore our classical picture that a perfect conductor has zero resistance. On the other

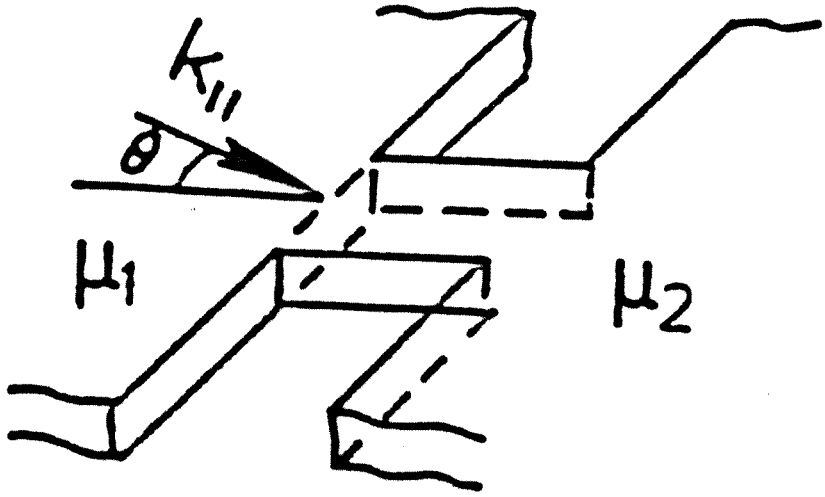

Figure 3.3: A configuration for calculating contact resistance.

hand, the narrower a BQW is, the fewer the conducting channels are and the more obvious the conductance quantisation is. Eventually, the conductance will be zero when there is no conducting channel involved. This naturally leads to an area of interest at the limit of electrical conduction, such as the recent discovery of quantised conductance in a ballistic quantum point contact [9, 10]. Furthermore, another explanation is needed for the observation of the universal conductance $G = 2e^2/h$ when $N = 1$ and $T = 1$. It is obvious that the 1D quantum relation between the Fermi velocity and the density of states at the Fermi energy, Eq. (3.12), makes this simple and unique formula Eq. (3.15) possible. Because this relation arises only in 1D case, it is reasonable to attribute this universal constant conductance partly to the effect of system dimensionality — quasi-1D or 2D with finite boundaries. However, the constant conductance of a BQW is only associated with the L-B formulae rather than the Landauer formula. For such a uniform perfect wire coupled without scattering to reservoirs, a connection has been made between the universal constant $2e^2/h$ and contact resistance [83]. It would be helpful and illuminating to understand this connection by recalling the calculation of contact resistance [84]. As we know, contact

resistance is caused by the geometrical shape of a narrow lead connected to a large electrode. Let us consider the configuration shown in Fig. 3.3, where a narrow perfect conductor with cross section A is connected to two large conductors which have chemical potentials μ_1 and μ_2 respectively. Two contacts are formed at the two ends of the narrow conductor. Because of the perfectness of the narrow conductor, the resistance of this system can be completely attributed to the two contacts for which the same contact resistances are assumed [85]. We first calculate the current injected from the left-hand side conductor with chemical potential μ_1 to the narrow region, which is

$$\begin{aligned} I_1 &= (-e)A\int \frac{4}{8\pi^3}k_{\|}d\theta dk_{\|}dk_{\perp}\frac{\hbar k_{\|}}{m^*}\cos\theta \\ &= (-e)A\frac{4}{8\pi^3}\int_0^{k_{F_1}}\frac{\hbar k_{\|}^2}{m^*}dk_{\|}\int_0^{(k_{F_1}^2-k_{\|}^2)^{1/2}}dk_{\perp}\int_{-\pi/2}^{\pi/2}\cos\theta d\theta \\ &= \frac{(-e)A}{16\pi^2}\frac{\hbar}{m^*}k_{F_1}^4 \\ &= \frac{(-e)A}{4\pi^2}\frac{m^*}{\hbar^3}\mu_1^2, \end{aligned} \tag{3.28}$$

where $\mu_1 = E_{F_1} = (\hbar k_{F_1})^2/2m^*$. Hence, the net current traversing the contacts and the system is

$$\begin{aligned} I &= I_1 - I_2 \\ &= \frac{(-e)A}{4\pi^2}\frac{m^*}{\hbar^3}(\mu_1-\mu_2)(\mu_1+\mu_2). \end{aligned} \tag{3.29}$$

If we define $\delta\mu = \mu_1 - \mu_2$ and $\mu = (\mu_1+\mu_2)/2$ as well as the number of conducting channels in the cross section A as $N_\perp = (4/4\pi^2)A\pi k_F^2 = (A/\pi)(2m^*/\hbar^2)\mu$, we finally have the net current in the form

$$I = \frac{(-e)}{4\pi\hbar}N_\perp\delta\mu = \frac{e^2}{2h}N_\perp\frac{\delta\mu}{(-e)}. \tag{3.30}$$

When there is only one channel involved, *i.e.* $N_\perp = 1$, the contact resistance for each conducting channel at each contact is universal as we have found before:

$$R_{\text{contact}} = \frac{h}{e^2} \tag{3.31}$$

which is only two times the universal resistance which we have obtained from the L-B formula Eq. (3.14) for a single-channel BQW.

Chapter 4

The chemical potential in a transport system

4.1 Introduction

Before we start talking about the chemical potential in a transport system, let us first make a brief review about the concept of chemical potential itself and some relevant features of it. When a system is in an equilibrium state, the second law of thermodynamics requires the entropy of the system approaches its possible maximum value in a given environment. Under this condition, a distribution function can be defined to describe the probability of each microstate being occupied. The environment of such a system can be changed in a so-called quasi-static adiabatic way so that the system undergoes a reversible process from one equilibrium state to another provided that its entropy remains at the same value. Such a system is normally not isolated any more and the number of particles in it may be indeterminate, such is the case in a grand canonical ensemble. When the interactions between the system and its environment are defined, there is a corresponding thermodynamic function to describe the relation between the changes of the system and the work that the environment has done to the system during the process. The amount of work associated with the addition of one particle to such an equilibrium system is defined as the **chemical potential** of the system.

The form of distribution function for an equilibrium system depends on the nature of the particles and so does the chemical potential if the system has indeterminate number of particles. Often we can treat the particles as classical particles and use classical Boltzmann statistics to describe them. However, the distribution function will depart from its classical form when the following condition is fulfilled [86]

$$k_B T \leq \frac{h^2}{2\pi m}\left(\frac{N}{V}\right)^{2/3}, \tag{4.1}$$

where m is the mass of particle, N is the number of particles and V is the volume of system. Under this condition, the thermal energy which each particle has on average is smaller than its kinetic energy. So that the degeneracy of the microstates will affect the particle distributions and quantum effects will appear. The reason for this is simple. Let us consider a system of N particles of a certain kind. If the interactions between the particles are weak enough, the **single-particle approximation** works and we can treat the motion of each particle as to be independent of all the others. This is the case for the 2DEG systems. The quantum states allowed for these individual motions — single-particle states — are determined by a single-particle Schrödinger equation and are described by the energies of these states and the wave functions associated with them. However, the occupation number of each of these quantum states is restricted by a general principle of quantum mechanics: the wave function of a system of identical particles must be either symmetrical or antisymmetrical under the permutations of the particle coordinates. These two kinds of particles are known as bosons and fermions respectively. Unlimited number of bosons can be in the same quantum state while only one fermion per state is allowed at any time. Quantum statistics are needed to include the effects of these two kinds of microstate degeneracy when the condition in Eq. (4.1) is fulfilled. Correspondingly, there are two types of quantum distribution functions, the Bose-Einstein distribution function [87, 88] and the Fermi-Dirac distribution function [89, 90]. Particularly important applications of these quantum distributions are those involving phonons and electrons in solids.

It is necessary to use the Fermi distribution function in our calculations.

The phenomena which we are going to study in the 2DEG microstructures have their origin in quantum size effects and the effects of an applied magnetic field. The energy scales associated with these two effect are $E_s = h^2/2\pi m^*(2W)^2$ and $E_B = \hbar eB/m^*$ respectively, where W is a length associated with the size of a microstructure, e is the absolute value of electron charge, and m^* is the particle mass. For a system of free electrons with $W \sim 100$ nm in a magnetic field $B \sim 10$ T, the energy scales, E_s and E_B, in the unit of temperature are about 0.38 K and 13 K respectively. Since the electron in the GaAs microstructures has an effective mass $m^* \sim 0.067\ m_e$ [39], the corresponding E_s and E_B are about 5.5 K and 190 K respectively. In other words, the temperatures in the GaAs system we study should be lower than 5 K in order to observe the quantum phenomena associated with E_s. It is clear that the quantum effects which are observed in the temperatures below several Kelvins in GaAs microstructures are mainly due to the quantum size effect which is enhanced by the reduction of the electron effective mass. To observe quantum size effects in a Si microstructure, we need to be in even lower temperatures under the same conditions because the effective mass of electrons in Si is $0.19m_e$ [39]. However, in these 2DEG systems, the ratio N/V is normally about 10^{23} m^{-3} for a standard electron sheet density $n_s \sim 10^{15}$ m^{-2} with a typical layer thickness $\sim 10^{-8}$ m [91]. Hence, the condition in Eq. (4.1) will be fulfilled when $T < 12$ K. If we put the electron effective mass in GaAs, $m^* \sim 0.067\ m_e$, into Eq. (4.1), the temperature satisfying the condition can be as high as two hundred Kelvins. Hence, we should treat a 2DEG system at low temperatures as a quantum system of fermions and consider the chemical potential which is associated with the Fermi-Dirac distribution function. The average occupation number of a single-particle state α in our system will be given by

$$f(E_\alpha) = \frac{1}{e^{(E_\alpha - \mu)/k_B T} + 1} \tag{4.2}$$

where E_α is the energy of the quantum state α and μ is the chemical potential which is sometimes called the Fermi energy in semiconductor physics.

In a fermion system, the chemical potential has some distinct properties. It can be either positive or negative but is normally larger than the energy of

the ground single-particle state in the systems discussed here (when μ is much smaller than the ground state energy, the system reaches its classical limit and the Fermi distribution can be replaced by the Boltzmann distribution). If the energies of the single-particle states are independent of temperature T, μ becomes smaller when T is lowered. When $T \to 0$, μ tends to a finite limit which is the average free energy per fermion. The last and the most useful property of μ is that at low temperatures the number of the occupied states with their energies larger than μ equals to the number of the unoccupied states with their energies smaller than it. At $T = 0$, there is no unoccupied states below μ and no occupied states above it. Consequently, we find out that μ plays a dual role in Fermi statistics: it not only characterises the free energy of fermions but also determines their distributions in energy.

4.2 The chemical potential in the Landauer and L-B formulae

It is obvious from the above discussion of the nature of the chemical potential that, in a transport system, we cannot define a chemical potential because of the non-equilibrium condition of the system. In principle, we may talk about the chemical potential of a system only if there are no potential differences or associated particle flows. In that case, the chemical potential in Eq. (4.2) is the same for any particle in any part of the system. Because of this, we cannot use a global chemical potential to describe a non-equilibrium system which is intrinsically non-uniform. However, it would be very inconvenient to study electronic transport in a system without using an appropriate quantity to describe the driving force in it. There are other potentials, such as electrostatic potential. While, the quantity associated with resistance could be nothing but chemical potential as has been stressed in Ref. [70],

There are two ways to escape from this dilemma. One is the approach used in the derivation of the L-B formula [75]. It takes the advantage of the presence of terminals in microstructures and uses the chemical potentials of the

equilibrium reservoirs connected to the leads and the net currents in the leads to define the conductance between different parts of a system. This method require neither a specific arrangement of the contact configurations nor particular kinds of voltage contacts. It avoids the difficulty of defining chemical potential in a non-equilibrium system. However, we may only calculate the total conductance contributed by the system *and* the leads. It is difficult to use this method to present a detailed picture inside a microstructure and distinguish the contributions from different parts of a system to the final results. Moreover, a microstructure with a lead attached to it is not the same as the microstructure without the lead. Therefore, if we want to look at details, a local parameter is needed. This leads to the other way, defining "chemical potential" in a transport system. Obviously this parameter cannot be uniform for a system in a non-equilibrium state but it should become the global chemical potential when the system *is* in an equilibrium state. The very definition of "chemical potential" away from equilibrium permits some exercise of taste and choice. The chemical potential which Büttiker *et al.* used in rederiving the Landauer formula is one of them [69]. As being pointed out by Landauer [92], the definition should be the quantity which in an equilibrium system will take us to the same average electron occupation. In other words, it should measure the electron density [93].

Büttiker *et al.* suggested, in 1985, a method to define a chemical potential in a uniform perfect measurement lead connecting a reservoir to an obstacle in the presence of transport in a near-equilibrium state at all temperatures [69]. The chemical potential is determined by equalising the number of unoccupied states below it to the number of occupied states above it. This is similar to the situation for the real chemical potential in equilibrium system at finite temperatures, but this time the redistribution of the occupied states is due to the near-equilibrium status of the system since the other side of the obstacle is connected to another reservoir. This parameter satisfies the Landauer condition and gives the true chemical potential and electron density when the system is in equilibrium. Using this definition, Büttiker *et al.* regained the Landauer

formula and revealed the relationship between the Landauer formula and the L-B formula. This definition of chemical potential can also be established by using a weakly coupled voltage lead through a current-stop measurement procedure [70]. Many quantum effects, such as the quantum oscillations of the transmission probability through a 1D normal-metal ring to a voltage lead [79] and the role of quantum coherence in series resistors [94] as well as the chemical potential oscillations in a perfect lead near an obstacle in the presence of transport [95, 96] have been discussed in terms of this parameter. However, this definition of chemical potential is intrinsically quasi-1D and can only be used in studying longitudinal resistance, because it merely concerns changes *along* a measurement lead and pays no attention to the *cross section* of the lead. Special arrangements for the configuration of leads can be made to measure off-diagonal resistance, such as in a Hall bar system. However, the result describes the Hall bar rather than a microstructure itself. If we want to investigate the Hall effect thoroughly, we need a 2D "chemical potential".

4.3 Local chemical potential

A 2D form of the "chemical potential" in transport microstructures at zero temperature was proposed in 1986 for two-lead single-channel case [97] and was generalised to two-lead multi-channel situation three years later [98]. The approach is based on the same measurement reservoir idea [70] which was adopted by Büttiker *et al.* [69], using a current-stop procedure to determine the chemical potential in a measurement reservoir which is connected weakly to the microstructure being measured by a voltage lead. The value of the determined chemical potential for the measurement reservoir is defined as the "**local chemical potential**" (LCP) at the site where the voltage lead is connected. It is obvious that the LCP is merely a parameter and it stands for a real chemical potential only when the system is in equilibrium. However, the LCP has the character of a chemical potential and is the driving force of current in resistance measurement.

To determine the LCP on the site $\mathbf{r} = (x, y)$ in a uniform two-lead system,

we connect the site to a measurement reservoir with chemical potential μ_r which satisfies the condition $\mu_s \geq \mu_r \geq \mu_d$, where μ_s and μ_d are the chemical potentials in the source and drain reservoirs respectively. By assuming that there is only one conducting channel in the measurement lead, the coupling matrix elements squared are $\epsilon_{i,E}^{(s)}|\psi_{i,E}^{(s)}(\mathbf{r})|^2$ and $\epsilon_{i,E}^{(d)}|\psi_{i,E}^{(d)}(\mathbf{r})|^2$ for the states coming from the source and drain respectively, where $\epsilon_{i,E}^{(s)}$ ($\epsilon_{i,E}^{(d)}$) is the modulus squared scattering matrix element for the state in the i-th channel with energy E from the source (drain) and $\psi_{i,E}^{(s)}(\mathbf{r})$ ($\psi_{i,E}^{(d)}(\mathbf{r})$) is the magnitude of the wavefunction for this state at the site $\mathbf{r}$. The total number of conducting states contributed by the electrons from the source to the measurement lead is

$$N^{(s)} = \int_{\mu_r}^{\mu_s} dE \sum_i n_i(E)\epsilon_{i,E}^{(s)}|\psi_{i,E}^{(s)}(\mathbf{r})|^2 \tag{4.3}$$

where $n_i(E)$ is the density of states for the channel i at energy E and the subscript i runs over all the conducting channels. Furthermore, we assume that the system is in a near-equilibrium state, *i.e.* $(\mu_s - \mu_d)/(\mu_s + \mu_d) \ll 1$, and the scattering matrix elements are the same for different channels. With the aid of the 1D quantum relation of the density of state and the corresponding group velocity, the kernel of the integral in Eq. (4.3) can now be replaced by the quantities at the Fermi energy. Hence, we have

$$N^{(s)} = (\mu_s - \mu_r)\frac{4}{h}\epsilon^{(s)} \sum_i \frac{1}{v_{Fi}^{(s)}}|\psi_{i,E_F}^{(s)}(\mathbf{r})|^2. \tag{4.4}$$

where $v_{Fi}^{(s)}$ is the group velocity for the i-th channel at the Fermi energy. Similarly, the total number of conducting states contributed by the electrons from the drain to the measurement lead is

$$N^{(d)} = (\mu_d - \mu_r)\frac{4}{h}\epsilon^{(d)} \sum_i \frac{1}{v_{Fi}^{(d)}}|\psi_{i,E_F}^{(d)}(\mathbf{r})|^2. \tag{4.5}$$

The elements of scattering matrix have been proved to be the same for the states in the same channels coming from two opposite directions [79] (this means that the direction of the current in the measurement lead is perpendicular to both the opposite going currents), and the corresponding group velocities of the electrons for the same channel are approximately equal to each other because the system

being measured is in the near-equilibrium state. Hence, the net current in the lead will be zero when the following condition is fulfilled

$$N^{(s)} + N^{(d)} = 0. \tag{4.6}$$

This current-stop procedure determines the LCP at the site $\mathbf{r}$, which has the form

$$\mu_r(\mathbf{r}) = \frac{\sum_i \left[|\psi_i^{(s)}(\mathbf{r})|^2 \mu_s + |\psi_i^{(d)}(\mathbf{r})|^2 \mu_d\right] / v_i}{\sum_i \left[|\psi_i^{(s)}(\mathbf{r})|^2 + |\psi_i^{(d)}(\mathbf{r})|^2\right] / v_i} \tag{4.7}$$

where all the quantities are at the Fermi energy and the corresponding subscripts are omitted.

The definition of the LCP is based on many assumptions about an idealised isotropic noninvasive contact and is only for a uniform two-lead system. Nevertheless, Eq. (4.7) provides with a way of looking at the spatial variation of the current driving force in a microstructure and enables studies to be made of the off-diagonal response of the system itself in an external field. Moreover, the wavefunctions in Eq. (4.7) are for the eigenstates of the system being studied. The quantum phase relations between the injected and reflected electron wavefunctions are included and the LCP gives phase sensitive results unless there are other approximations on the squared wavefunctions having been made. In fact, if we apply Eq. (4.7) to the 1D problem which Büttiker has studied with the weakly coupled voltage lead [95, 96], we can get exactly the same result for the chemical potential oscillations which are due to the coherent interference between the incident electron wavefunctions and the reflected ones. The phase average and phase insensitive results can also be obtained by using different approximations. In the equilibrium state of a system, the quantum interference still exits. Despite the oscillations in the density of electrons caused by the reflections, the local chemical potential will be constant throughout the real space because $\mu_s = \mu_d$. This is consistent with the definition of the true chemical potential.

In the following chapters we will use the LCP to calculate some intrinsic properties of the BQWs in an external magnetic field. However, one may well ask that whether the LCP is real, *i.e.* whether it can be measured or not.

We believe there should be a way which can be applied practically to measure this LCP no matter what assumptions we have made in its definition since it is defined by a measurement procedure. We will come back to this in detail later. Here, it should be mentioned that Büttiker has examined the induced local electric fields in the presence of current flow [80]. With the assumption that the wavefunctions vary slowly on the scale of the screening length, both the two-lead single-channel and multi-channel forms of Eq. (4.7) are obtained for the electrostatic potential from the Poisson equation at the strong screening limit.

4.4 A new definition of the LCP

The derivation of Eq. (4.7) rests on a particular view of the behaviour of non-invasive voltage leads [70, 97]. The equation is justified by envisaging a non-invasive lead which removes an infinitesimal current proportional to the local electron density in the channel considered. Some calculations [99, 100, 101] have been made for the LCP from Eq. (4.7) with the group velocity factors omitted (Eq. (4.7) itself is also used in [101]). In this case the lead is envisaged as removing an infinitesimal current which is proportional to the local current density in the channel considered. Both these hypothetical leads fit well into the single-particle formalism but it is not clear how either of them could be fabricated so as to behave in the manner assumed. We believe Eq. (4.7) is closer to the reality. Later in this thesis we will use a model calculation to prove that the chemical potential determined by the L-B formula at noninvasive limit have the exactly form as in Eq. (4.7) under certain conditions.

Büttiker has calculated the self-consistent electrostatic potential in a microstructure when currents are transmitted [80]. He uses the Thomas-Fermi approximation and assumes strong screening. The physics behind the calculation is completely different from that used in the calculation of the LCP described above. The same form as in Eq. (4.7) is obtained but with the LCP replaced by the electrostatic potential. Neither of the approximations made in his calculation are very appropriate to the single-particle formalism which

is usually employed to describe the electronic behaviour of semiconductor microstructures [80, 81]. Moreover, we discuss in the following chapter the Hall resistance derived from the numerically determined self-consistent electrostatic Hall potential which arises when current flows in the presence of a magnetic field. It behaves completely differently from the Hall resistance calculated from the LCP and, in particular, it does not exhibit the expected quantisation.

All these derivation of Eq. (4.7) are restricted to the linear response regime at zero temperature and several approximations are involved. Here, we will give a precise definition of the LCP in a multi-lead multi-channel microstructure described in the single-particle picture. It avoids any reference to noninvasive voltage leads and any assumptions as well as any approximations apart from those which are involved in the L-B formalism. The definition is valid in the nonlinear transport regime at all temperatures. In linear response regime at low temperatures it immediately reduces to Eq. (4.7) for a two-lead system.

We consider an arbitrary microstructure in two different situations. Firstly, a non-equilibrium situation in which the chemical potential in the reservoir feeding lead l takes an arbitrary value μ_l. We write $n_(\mathbf{r}, \mu_1, \mu_2, \cdots)$ for the electron density at $\mathbf{r}$ in this case. Secondly, we consider an *equilibrium* situation in which $\mu_l = \mu_0$ for all l. The electron density at $\mathbf{r}$ in this case is simply $n(\mathbf{r}, \mu_0, \mu_0, \cdots)$ which we abbreviate to $n_e[\mathbf{r}, \mu_0]$.

We now define the LCP at the point $\mathbf{r}$ by the equation

$$n_e[\mathbf{r}, \mu(\mathbf{r})] = n(\mathbf{r}, \mu_1, \mu_2, \cdots), \tag{4.8}$$

i.e. $\mu(\mathbf{r})$ is the chemical potential in the equilibrium system which creates the same electron density at $\mathbf{r}$ as that which is actually found there in the non-equilibrium system. In other words, we may really know the distribution of the LCP in a microstructure if the density of electrons at any site in it can be measured.

Eq. (4.8) applies at all temperatures and all values of μ_l. It is easily solved for $\mu(\mathbf{r})$ in the linear, low temperature regime assumed in Eq. (4.7). Since the

reservoirs are phase randomising, we have

$$n(\mathbf{r},\mu_1,\mu_2,\cdots)=\sum_l\sum_i\int dE f_l(E)n_{li}(E)|\psi_{li}(\mathbf{r})|^2 \tag{4.9}$$

where $f_l(E)$ is a Fermi-Dirac function with chemical potential μ_l and $n_{li}(E)=4/hv_{li}$ is the density of states for channel i in lead l. To obtain $n_e[\mathbf{r},\mu(\mathbf{r})]$, we have only to replace every $f_l(E)$ in Eq. (4.9) by the Fermi-Dirac function $f_\mu(E)$ which involves the LCP $\mu(\mathbf{r})$. According to Eq. (4.8), the difference between these two quantities must vanish. The integrals in the difference involve

$$\begin{aligned} f_l(E)-f_\mu(E) &\simeq -[\mu_l-\mu(\mathbf{r})]\frac{df_0(E_F)}{dE} \\ &\simeq [\mu_l-\mu(\mathbf{r})]\delta(E-\mu_0) \end{aligned} \tag{4.10}$$

Here $f_0(E)$ is the Fermi-Dirac function involving the original chemical potential E_F of the microstructure before it was perturbed. The first approximation in Eq. (4.10) is valid in the linear regime because both μ_l and $\mu(\mathbf{r})$ remain close to μ_0. The second approximation is standard at low temperatures. With the aid of Eq. (4.10), we find immediately that Eq. (4.8) have the form

$$\mu(\mathbf{r})=\frac{\sum_l p_l\mu_l}{\sum_l p_l}, \tag{4.11}$$

where

$$p_l=-\frac{\sum_i|\psi_{li}(\mathbf{r})|^2}{v_{li}}. \tag{4.12}$$

For a two-lead uniform wire, it reduces to Eq. (4.7).

The advantage of the new definition of $\mu(\mathbf{r})$ is that it involves no assumptions or approximations which are not already involved in the Landauer-Büttiker formalism. No appeal is made to self-consistent fields, screening, or non-invasive probes of any sort. Moreover, the general formula Eq. (4.8) for $\mu(\mathbf{r})$ is valid at high temperatures and in nonlinear regime, and it can be directly used in the dimensions higher than 2D if necessary.

Chapter 5

Intrinsic quantum Hall effect in a BQW

5.1 Introduction

Since the discovery of the IQHE by von Klitzing, Dorda, and Pepper in 1980 [4], much attention has been devoted to the transport properties of a 2DEG in a magnetic field [103]. Two years later, the FQHE was observed [32], where the quantisation of the Hall resistance is a rational fraction of the universal constant h/e^2 with normally odd number denominators. During the continuous advance in understanding the mechanism of the IQHE and FQHE, much theoretical progress has been made [104]. In 1981 Laughlin used an ideal experiment to demonstrate the possibility of the existence of integer quantised Hall resistance [105]. Halperin in 1982 pointed out that the Landau levels of a 2DEG rise as the edge of the system is approached and form quasi-continuous delocalised edge states in which the main part of the current and the Hall voltage drop are located [50]. Two opposite-going currents propagate along two opposite sides of a 2DEG respectively. The same kind of physical picture as described by Teller in 1931 [106] was reproduced. The IQHE is attributed to the existence of energy gaps between the bulk Landau levels, and the vanishing of the diagonal elements of resistivity tensor in the middle of each Hall plateau is due to the vanishing of the diagonal elements of conductivity tensor when the Fermi energy is in

between the bulk Landau levels. In 1983, Laughlin constructed the renowned Laughlin wavefunction to describe the behaviour of 2D interacting electrons in a symmetric gauge and attributed the FQHE to the many-body energy gap [107]. However, Laughlin's ground and excited quasi-particle wavefunctions can only explain the $1/M$-type FQHE. Haldane used them to construct new quasi-particles which form a hierarchy for the whole range of the FQHE [108]. Because the accuracy of the observed Hall resistance quantisations is very high, in the order of one tenth ppm, independent of the shape of the conductor and microscopic details, the IQHE is adopted as a resistance standard. Such high accuracy as a general feature of this effect leads to the belief that there must exist a fundamental explanation of it. Naturally, some topological considerations are introduced to examine closed conductors in which exact quantisations are shown [109, 110]. Despite of all these successes, people pursue their studies for finding a way which can deal with both the IQHE and FQHE on the same footing. In 1989, Jain suggested a so-called composite fermion picture which is understood as fermions interacting with a Chern-Simons gauge field and gave a unified explanation to the IQHE and FQHE as well as the construction of a hierarchy [111]. Four years later, by using the same picture, Halperin *et al.* successfully transformed a 2DEG in an external magnetic field with Landau level half filled to a mathematically equivalent system of fermions with zero average effective magnetic field acting on the fermions [112] and explained why no one half quantisation has been found. Further developments along these lines are in progress [34].

All the approaches mentioned above concern closed conductors. The electron reservoirs connected onto the conductors and the effect of measurement procedures are not included. The Hall resistance there is assumed to be additive because only the Hall resistivity is considered. Actually, the conductor in real situations is an open conductor which connects several electron reservoirs at the same time. Experiment results show clearly that if the source and drain are close enough the quantisation of the Hall resistance is not generally maintained [113, 114]. This reminds us that we cannot fully describe the QHE without con-

sidering the effect of current source and drain. Moreover, the quantised Hall resistance is nonlocal because of the long-range nature of electron transport in high magnetic field as shown by experiments [118]. In such a quantum coherent system, resistivity is not a very suitable quantity to use in describing electron transport. Therefore, a new approach is needed to deal with the quantised Hall resistance in open conductors. A 2DEG should be examined together with the measurement leads. Furthermore, the fact that a real 2DEG has a finite size has also to be taken into account. This is a very different picture from an exact 2D case. For an exact 2D system there are energy gaps between the Landau levels. When its Landau levels are completely filled the system appears as an insulator in a weak electric field. While for a finite 2DEG, the the Landau levels overlap because of the effect of the edges and there is no energy gaps between them. Moreover, each Landau level can only be partially occupied to form a conducting channel, and and the system always appears as a conductor. However, the conductance between a source and drain keeps finite due to the finite size of the system even when there is no impurities in it.

In 1988, Büttiker successfully described a picture for the IQHE in the terms of the properties of measurement leads [115, 116, 95]. As in the case of typical experiments, current leads are considered together with voltage leads on the same footing. The Hall resistance is calculated by using the L-B formulae with the aid of the concept of edge states. Exact quantisations of the Hall resistance are obtained under certain conditions as the results of counting conduction channels, while the longitudinal resistance approaching zero is the result of equalisation of chemical potentials in two measurement reservoirs connected to the same edge of the system in the absence of backscattering. Generalisation of this picture to the FQHE regime was made two years later by Beenakker [117]. We understand from the L-B formulae that quantisation of resistance can be maintained only when there is no backscattering of electrons. In other words, the absence of the inter-edge state scattering is essential for perfect quantisation of resistance in the QHE. Büttiker carefully examined this problem and concluded that there is no scattering backwards against the flow of carriers

over distances which are large compared to the cyclotron radius [115]. Both elastic and inelastic backscattering in 2D conductors are suppressed significantly by high magnetic field. Later on, this theoretical consideration was confirmed by experiments [119]. More detailed calculations have been done for the inter-edge state scattering rate for elastic scattering and for acoustic phonons and exponential reductions are found for both these scattering rates in high fields [120]. Another important problem has also arisen from experiments: edge states which initially have been populated unequally do not equilibrate even over a very long distance [118]. This result shows again the crucial role of the contacts for high precision measurement of the QHE. It is necessary to inject and detect electrons in an equilibrium way to observe quantised resistance. Further experimental results show that the outermost edge states equilibrate over a long distance with each other but not with the innermost edge state [121]. It is worth mentioning that, although the inter-edge state scatterings are suppressed, the intra-edge state scatterings are probably not suppressed [33]. Therefore, the high field phase coherence length which is limited by intra-edge state scattering is not longer than the one in zero field. Consequently, the QHEs in 2DEGs can be explained in the framework of the L-B formulae and the quantisation of the Hall resistance is attributed to the measurement effect of the measurement leads on the edge states. Numerical calculations have been done for the QHE for a four-lead junction [124, 125, 126]. A detailed review of this approach can be found in Ref. [33].

The investigations of the QHE do not stop here. We may go further and ask what the *intrinsic* Hall resistance of a microstructure is. In the other words, how such a system itself, apart from the measurement leads, responds to an external magnetic field and how will this intrinsic Hall resistance differ from what is measured when four conventional leads are used. Furthermore, other questions arise concerning the behaviour in a magnetic field: the LCP, the electrostatic Hall potential (EHP) and the resistances associated with them. Here, we consider intrinsic *resistance* rather than intrinsic resistivity because the former is a global quantity which is suitable for describing *finite* quantum

coherent systems. Naturally, noninvasive voltage contacts should be used for measuring both the LCP and the EHP. We suppose that it is possible to achieve such a measurement as discussed by Engquist and Anderson [70] and Landauer [122]. Recently, for example, Shepard, Roukes, and van der Gaag have measured quantum Hall resistance behaviour in this limit [123]. In this chapter, we are going to study the **intrinsic integer quantum Hall effect** (IIQHE) in microstructures. The absence of backscattering in high magnetic field is assumed so that we can treat these systems as *ballistic*, even they may not be intrinsically so. The Coulomb interactions between electrons are included self-consistently. Both the EHP and the LCP and the corresponding Hall resistances, $R_{\rm EHP}$ and $R_{\rm LCP}$, are calculated. Calculations are carried out in a BQW when up to three Landau levels are occupied. We find that the former resistance is nearly linear in magnetic field in spite of Landau level depopulation but the latter is quantised.

5.2 Previous theoretical works on the IIQHE

The first calculation of intrinsic Hall field distribution for a 2DEG with the Hall bar geometry is a classical one by Rendell and Girvin [127] which uses a local conductivity tensor. However, as we know, both of the Hall field distribution and the current are nonuniform even in this idealised geometry and they cannot be described by uniform local quantities. After that, the behaviour of a interacting 2DEG was calculated quantum mechanically by MacDonald, Rice, and Brinkman with the assumption of a slowly varying potential which is appropriate to high magnetic fields [128]. By using a Hartree approximation, a self-consistent (SC) equation is derive for calculating the redistribution of charge in real space, which generates the EHP, as well as the current density distribution. The tendency toward the system edges is found for all these distributions and is attributed by the authors to the electron-electron interactions. The size of the system is introduced in the calculation, however, the system is intrinsically 2D since no partially occupied Landau levels are considered. In fact, the IIQHE of a 2DEG confined in a BQW is quite different from that of its

unconfined counterpart. As we know from the general case, there is no energy gap and each Landau level is always only partially occupied. The rise of the Landau levels as an edge is approached is mainly due to the potential confinement at the edges. The longitudinal conductance is finite instead of infinite in such a ballistic system since the wire has finite width. Li and Thouless study this problem for the interacting electrons in a GaAs wire in a weak magnetic field when only the lowest Landau level is occupied and give results for the EHP [129]. The electrostatic interactions between the electrons in a certain magnetic field are considered properly, using a square well potential confinement as an effective single electron potential for a 2DEG in a BQW at zero magnetic field [43]. Only the potential due to the redistribution of the electron density in a magnetic field should be taken into account. Unfortunately, they do not include more Landau levels because of a numerical instability which they argue is due to the assumed hard-wall confining potential. Their calculations do not yield a quantised integer Hall resistance. This is not only because the Fermi level lies below the excited Landau levels. More importantly, these authors concentrate on the EHP and, as we show later, the corresponding Hall resistance is *always* nearly linear in the magnetic field. The electrostatic theory of a 2DEG in a BQW is also studied by Chklovskii, Shklovskii, and Glazman [132]. They find that the SC electrostatic potential in the region occupied by 2DEG changes in a step-like manner and forms alternating strips of compressible and incompressible electron liquids along the wire. However, the authors start their calculations with the assumption that there exists a square well potential confinement and then, in addition, consider the Coulomb interactions between the electrons. This procedure introduces a large additional electrostatic potential into the calculation and makes the system very different from what we usually believe to exist in real experimental situations as described in Ref. [43].

The QHEs associated with the chemical potential in some BQWs have been studied by using the so-called weak-link model [99, 130, 100, 101, 131]. Two voltage leads are placed on the two sides of the wire. One end of each lead connects to an electron reservoir and the other end contacts one edge of the wire

in a weakly coupled manner. The chemical potentials in the reservoir as well as the Hall resistance are calculated by the L-B formula. A typical result is shown in Fig. 5.1. However, there are three things which are not very clear in these

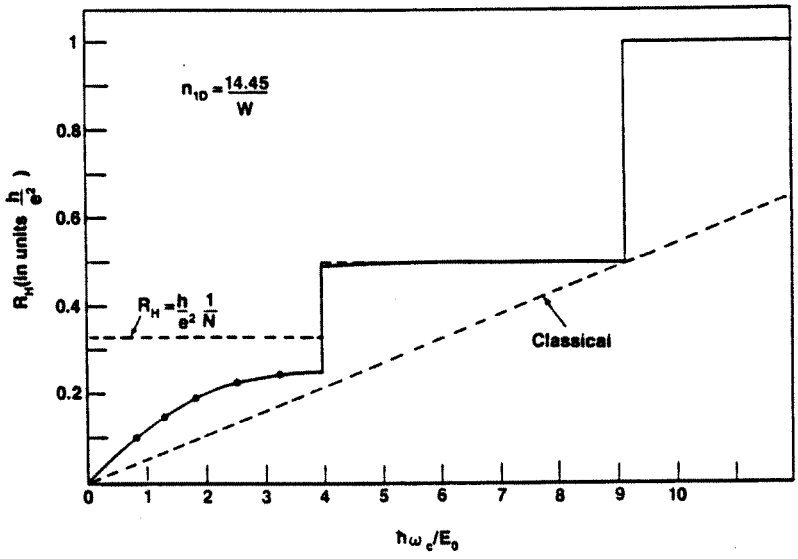

Figure 5.1: The Hall resistance (solid curve) for a three Landau level situation. The results from simple channel-counting arguments (dashed curve) and the classical result (straight dashed line) are also given as reference. (From Ref. [99])

calculations. First of all, there are no features of the measurement lead involved so that it is not clear what kind of measurement situation the calculations correspond to. Ideal voltage leads with different potential confinement give different results. *The measured Hall resistance depend strongly on the characters of the measurement leads even in the case of a noninvasive measurement.* We will show this in detail later in this thesis. Hence, the physics behind these calculated resistance is not well defined. Secondly, the infinitesimal current leaking from the wire is assumed to be proportional to the local current density in the channel considered. While, from what we have discussed in the last chapter, we know that the infinitesimal current removed by a noninvasive lead is proportional to local electron density. Therefore, the chemical potential used in these calculations does not include the effect of electron density of states and is

different from the LCP. Finally, none of these calculations consider the Coulomb interactions between electrons. How much this interaction would effect the Hall resistance is not known. Because of these problems, there is a need to calculate the Hall resistance of the IIQHE with the Coulomb interaction included. Before we end this section, it should be mentioned that there is one paragraph in Ref. [101] where the Hall resistance is calculated with the density of states factor included. However, the original form of the transmission coefficients used in calculating the Hall resistance in that paper is not, as the authors believed, the fraction of current, and there is no obvious physical reason for them to add the density of states factor into it.

5.3 The IIQHE for an interacting 2DEG in a BQW

In this section we present numerical IIQHE results for an interacting 2DEG in a BQW subjected to a perpendicular magnetic field when up to three subbands are occupied [133]. Electrostatic interactions between electrons within the same subband and among different subbands are included self-consistently. The same problem for non-interactiing electrons can be solved analytically in a non-SC manner as shown in Appendixe A. Spin degeneracy is also taken into account. We distinguish two kinds of intrinsic Hall potential, the EHP and the LCP, which depend differently on magnetic field and correspond to different measurements. Both the EHP and LCP differences and the two kinds of intrinsic Hall resistance associated with them are investigated. We demonstrate that quantisation occurs only for the Hall resistance connected with the LCP. We also find that the leading edges of the quantisation steps are rounded off at low B because of the overlap of wave functions propagating in opposite directions along the wire. Furthermore, we show that the resistance associated with the EHP retains the classical linear dependence on the magnetic field. Distributions of EHP, LCP and current density across the wire when one or two subbands are occupied are also calculated and shown.

5.3.1 The model

Let us consider a 2DEG with an electron density n_s which is confined in a space of width W in the x-y plane by infinite potential barriers at $y = \pm W/2$, as shown in Fig. 5.2. A uniform magnetic field B is applied in the z direction and describe

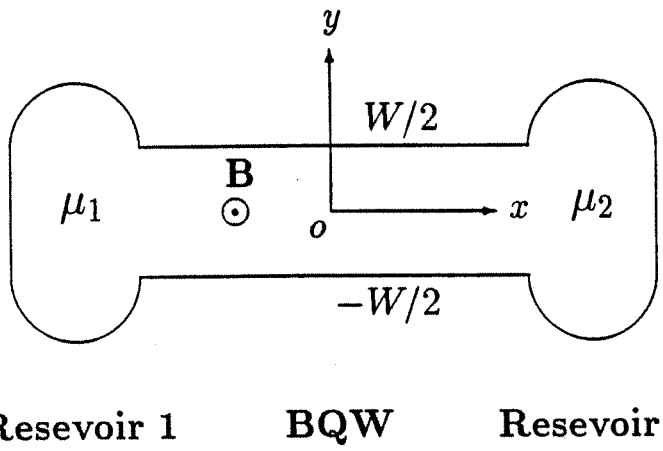

Figure 5.2: A sketch of our system.

it in the Landau gauge be writing the vector potential as $\mathbf{A} = (-By, 0, 0)$. Following previous authors [128, 129], we introduce an EHP $V(y)$ which is induced by the external magnetic field. The electron wave function $\psi_n(x, y)$ satisfies the Schrödinger equation

$$\left[\frac{1}{2m^*}(\mathbf{p} - (-e)\mathbf{A})^2 + (-e)V(y)\right]\psi_n(x, y) = E_n\psi_n(x, y) \qquad (5.1)$$

where m^* is the effective mass and n is the index of the subbands ($n = 0, 1, 2, \cdots$ refers to the lowest, the second, the third, $\cdots$ subbands). The normalised eigenfunctions are then of the form $\psi_n(x, y) = L_x^{-1/2} e^{ik_x x}\chi_{n,k_x}(y)$, where L_x is the length of the wire. The EHP, which must be determined self-consistently, can be expressed as

$$V(y) = \begin{cases} \dfrac{1}{4\pi\epsilon_0\epsilon}\displaystyle\int_{-W/2}^{W/2} dy'(-2\ln|y - y'|)\delta\sigma(y'), & -W/2 \le y \le W/2; \\ -\infty, & \text{otherwise}, \end{cases} \qquad (5.2)$$

where we consider the electrostatic interactions between electrons as homogeneous in the x direction. The redistribution of the electron charge density as a result of the external magnetic field is

$$\delta\sigma(y) = -\frac{e}{2\pi}\sum_{n,\sigma}\int_{k^{(n)}_{-x,E_F-\Delta/2}}^{k^{(n)}_{x,E_F+\Delta/2}} dk_x[|\chi_{n,k_x}(y)|^2 - |\chi^{(0)}_{n,k_x}(y)|^2]. \qquad (5.3)$$

where $k^{(n)}_{x,E_F+\Delta/2}$ and $k^{(n)}_{-x,E_F-\Delta/2}$ are the Fermi wave numbers of subband n for the positive and the negative x directions respectively, Δ is the chemical potential difference between the two terminals, and σ is the spin label. We make Δ small enough to ensure that we stay in the linear transport regime. The functions $\chi^{(0)}_{n,k_x}(y)$ are the eigenfunctions of the Schrödinger equation Eq. (5.1) in the absence of a magnetic field. With these definitions, we know that the EHP is related to the applied magnetic field and describes a kind of Hall effect and we have hard-wall, square-well confinement when $B = 0$. Furthermore, from Eqs. (5.2) and (5.3), we can see the spin degeneracy is important. The up- and down-spins give the same contribution to the EHP if we ignore the Zeeman splitting which is a reasonable first approximation in a model calculation for a GaAs system. In fact, the ratio of the Zeeman splitting to the Landau level splitting is $g_e\mu_B B/\hbar\omega_c \sim m^*/m_e \sim 0.067$, where $g_e = 2$ is the Landé g-factor for electron, $\mu_B = \hbar e/2m_e$ is the Bohr magneton, $\omega_c = eB/m^*$ is the cyclotron frequency, and m^* and m_e are the effective and real masses of electron respectively. To complete the calculation, it is important to constrain E_F in the Fermi wave numbers so as to yield the given electron density n_s for fixed Δ, *i.e.*

$$n_s = \frac{1}{2\pi W}\sum_{n,\sigma}[k^{(n)}_{x,E_F+\Delta/2} - k^{(n)}_{-x,E_F-\Delta/2}]. \qquad (5.4)$$

Then charge neutrality is ensured by the normalisation of the wave functions.

Solving the Eqs. (5.1)-(5.3) self-consistently with the constraint Eq. (5.4), we obtain the wave functions and the charge density redistribution as well as the SC EHP. The current density distribution across the wire can also be calculated from

$$j_x(y) = -\frac{e\hbar}{2\pi m}\sum_{n,\sigma}\int_{k^{(n)}_{-x,E_F-\Delta/2}}^{k^{(n)}_{x,E_F+\Delta/2}} dk_x\left(k_x - \frac{1}{l_B^2}y\right)\chi^2_{n,k_x}(y) \qquad (5.5)$$

where $l_B = (\hbar/eB)^{1/2}$ is the magnetic length. Since the total current is $I_x = \int dy j_x(y)$, the longitudinal resistance can be calculated straightforwardly as $R_L = \Delta/(-e)I_x$.

In addition to the EHP we may also calculate the LCP $\mu(y)$ using the form which we derived in the last chapter, which is

$$\mu(y) = \frac{\sum_{n,\sigma}[\mu_1|\chi_{n,k_{x,E_F+\Delta/2}}(y)|^2 + \mu_2|\chi_{n,k_{-x,E_F-\Delta/2}}(y)|^2]/v_n}{\sum_{n,\sigma}[|\chi_{n,k_{x,E_F+\Delta/2}}(y)|^2 + |\chi_{n,k_{-x,E_F-\Delta/2}}(y)|^2]/v_n} \tag{5.6}$$

where μ_1 (μ_2) is the chemical potential of the reservoir connected at the left (right) end of the wire, $\chi_{n,k_{x,E}}(y)$ and $\chi_{n,k_{-x,E}}(y)$ are the right- and left-going electron wave functions respectively, and v_n is the velocity at Fermi level. When the external magnetic field vanishes we may use the symmetry of the electron wave functions to show that the LCP is a constant everywhere. The difference of the LCP across the wire when $B \neq 0$ gives another kind of Hall effect.

The EHP is the electrostatic potential response when the electron density redistributes to balance the Lorentz force. It describes the real space potential which the electrons in the wire experience. One the other hand, the LCP characterises the local electron energy distribution and is determined by the overlap of wave functions propagating in opposite directions along the wire. By using Eqs. (5.2), (5.6) and (5.5), we can calculate both these potential distributions and current density distribution in the wire. We can also calculate two kinds of intrinsic Hall resistance from the EHP and the LCP respectively, which are $R_{\rm EHP} = (V(W/2) - V(-W/2))/I_x$ and $R_{\rm LCP} = (\mu(W/2) - \mu(-W/2))/(-e)I_x$ Previous authors have suggested ways to simulate [100] or measure [129] intrinsic Hall potentials. We believe that contacted-probes give the LCP differences in the weak coupling limit (when the measurement does not change the detected system) while the non-contacted probe method proposed by Li and Thouless [129] gives the EHP differences across the wire.

5.3.2 Numerical results about the IIQHE

In this subsection, we use the parameters of a GaAs wire, $m^* = 0.067m_e$ and $\epsilon = 13.1$ [39], with $W = 100$ nm and $n_s = 2 \times 10^{14}$ m^{-2} and 4×10^{14} m^{-2}. Our

results are very sensitive to the accuracy of the SC EHP and the Fermi wave numbers and, contrary to the experience of Li and Thouless [129], we get stable solutions for multi-subband occupancy in a hard-wall, square-well confining potential. The three-point Anderson-Pulay prediction method [134, 135], is used for accelerating the convergence of the SC process. A description of this method can be found in Appendix B.

Fig. 5.3(a) shows the current density distribution when $B = 0.25$ T and $n_s = 4 \times 10^{14}$ m^{-2} and two subbands are occupied, Fig. 5.3(b) is the corresponding result when $B = 1.25$T and only one subband is occupied. Figs.5.3(c) and 5.3(d) show the distributions of the EHP when $B = 0.25$ T and 1.25 T respectively and Figs. 5.3(e) and 5.3(f) show the corresponding distributions of the LCP in the unit of volt. The LCP in Fig. 5.3(f) is shifted down for convenience. The offset is 0.458 mV as marked in the picture. Comparing Figs. 5.3(a) and 5.3(b), we can see that the current density of the two occupied subband case spreads in the wire more than that of one occupied subband since B is increased and the Fermi wave numbers of each occupied subband in the former case are both smaller than the one in later. For the same reason, the amplitude of the EHP, $V(y)$, in Fig. 5.3(d) and the difference of the LCP across the wire in Fig. 5.3(f) are larger than that in Figs. 5.3(c) and 5.3(e) respectively. We note that there is a kink of the LCP in Fig. 5.3(e) because there are two occupied subbands and no such a kink in Fig. 5.3(f) for one occupied subband.

Fig. 5.4 exhibits the different behaviour of the two kinds of intrinsic Hall resistance. In Fig. 5.4(b), the $R_{\rm LCP}$ (circles) shows the step-like behaviour which is characteristic of the IQHE and the value of resistance at the N-th plateau is $h/2e^2N$ except on the "last plateau" ($0 < B < 0.5$ T). This quenching behaviour of the IQHE is due to the overlap of opposite-going wave functions of the same subband and we will discuss in detail in the next chapter. We note that the leading edge of the $R_{\rm LCP}$ step is not sharp as that of the longitudinal resistance (crosses). The curvature arises from the overlap between the right- and left-going waves in our 100 nm wire. Calculations for larger values of B show that the higher quantisation steps in the $R_{\rm LCP}$ are sharper because the

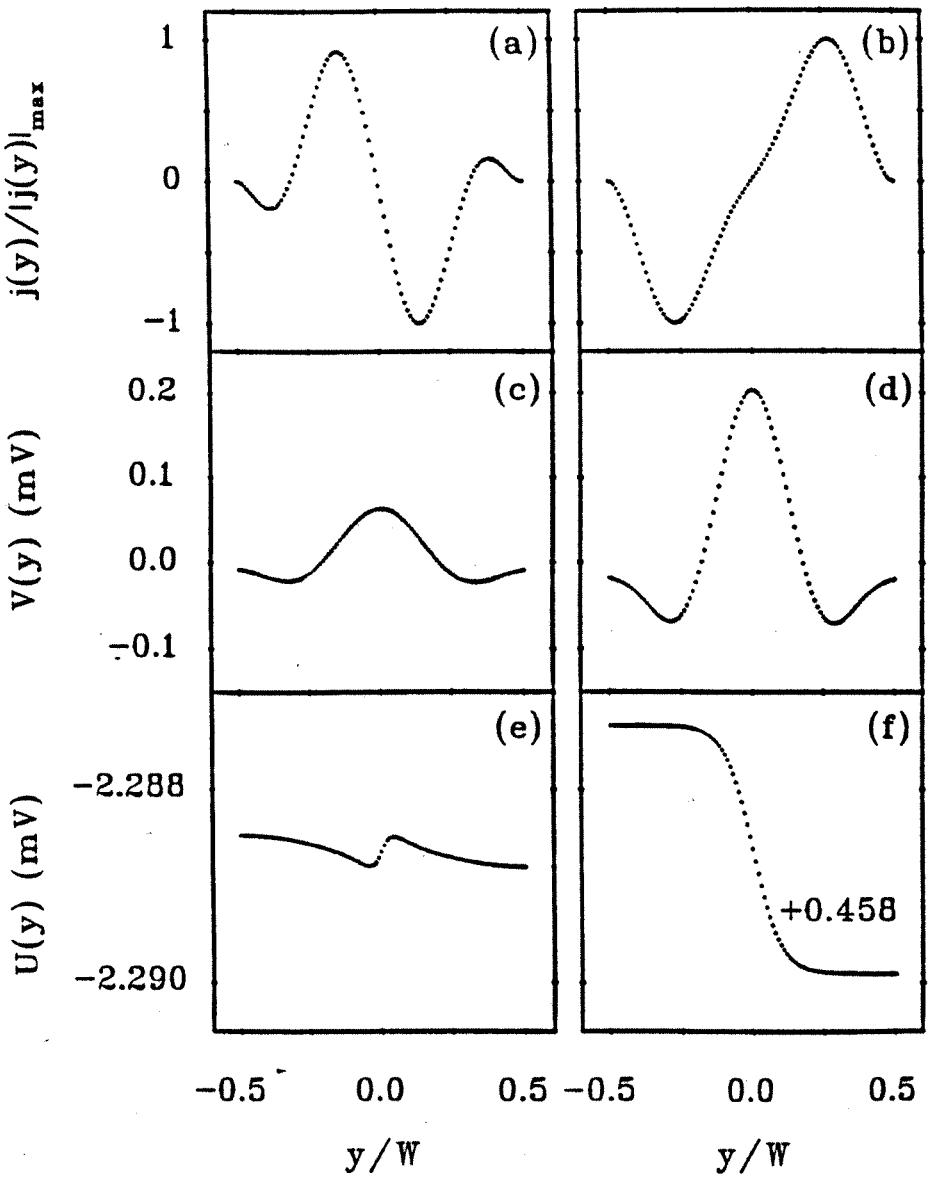

Figure 5.3: Current density $j_x(y)$: (a) $B = 0.25$ T and $|j_x(y)|_{max} = 0.3354$ A/m and (b) $B = 1.25$ T and $|j_x(y)|_{max} = 1.6968$ A/m; EHP $V(y)$: (c) $B = 0.25$ T and (d) $B = 1.25$ T; and $U(y) = \mu(y)/(-e)$: (e) $B = 0.25$ T and (f) $B = 1.25$ T. The offset to the LCP in (f) is 0.458 mV. Wire width is $W = 100$ nm and electron charge density is $n_s = 4 \times 10^{14}$ m^{-2}.

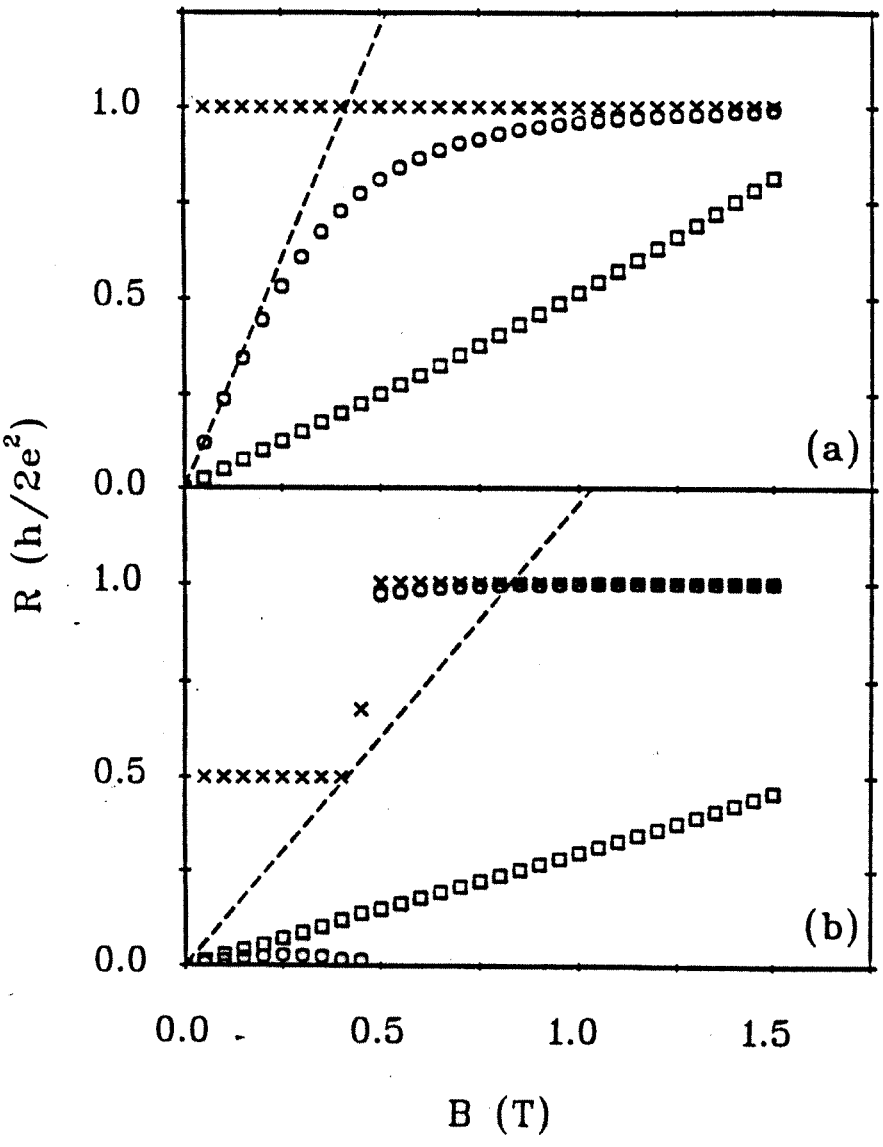

Figure 5.4: Plots versus B of the two kinds of intrinsic Hall resistance, R_{EHP} (squares) and R_{LCP} (circles), and the longitudinal resistance (crosses) for a quantum wire of width 100 nm with the electron densities (a) $n_s = 2\times10^{14}$ m^{-2} and (b) $n_s = 4\times10^{14}$ m^{-2}. The dashed lines in (a) and (b) are the corresponding Hall resistances for an unconfined 2DEG.

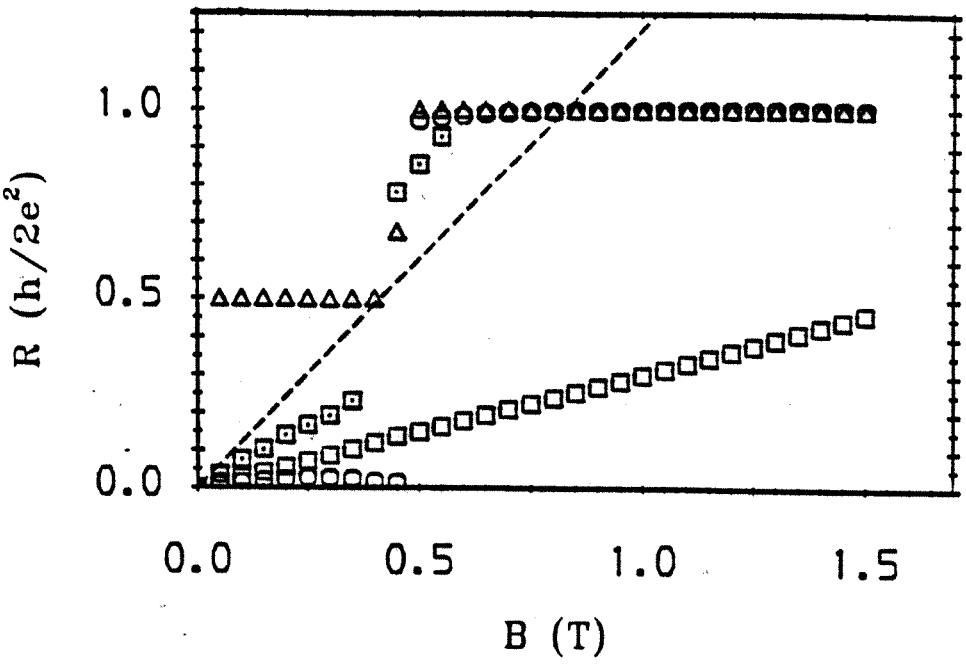

Figure 5.5: Plots versus B of the intrinsic Hall resistances, SC R_{EHP} (squares) and non-SC R_{EHP} (dotted squares) as well as non-SC R_{LCP} (circles), and the longitudinal resistance (triangles) for a quantum wire of width 100 nm with the electron density $n_s = 4 \times 10^{14}$ m^{-2}. The dashed line is the corresponding Hall resistances for an unconfined 2DEG.

opposite-going waves are more separated. We can easily show from Eq. (5.6) that, if there is no overlap, then the LCP between the two edges is equal to that between the two terminals of the wire and the quantisation steps of $R_{\rm LCP}$ become identical to those of the longitudinal resistance. Overlap is significant when the flux through an area W^2 is in the order of, or less than, h/e. In Fig. 5.4(b), the results for $R_{\rm EHP}$ (squares) show, in complete contrast to $R_{\rm LCP}$, nearly linear dependence on B despite the subband depopulation which occurs at $B = 0.5$ T. The slope of the line delineated by these squares is less than that appropriate to an unconfined 2DEG (dashed line) because of the finite width of the wire and the electrostatic interactions between electrons.

We see that quantisation of the IIQHE is seen only when differences of chemical potential are measured. The longitudinal resistance is exhibited by the crosses in Fig. 5.4. It is exactly quantised because it is again the result of measuring differences of chemical potential. Further calculations have shown that failure to achieve self-consistency leads to spurious jumps in $R_{\rm EHP}$ associated with the subband depopulation and a larger slope which increases when the number of occupied subband decreases. while the $R_{\rm LCP}$ in non-SC calculations behaves in almost exactly the same way as the SC result. An example is shown in Fig. 5.5 for the case of $n_s = 4 \times 10^{14}$ m^{-2}.

5.3.3 Further comparisons of the SC and non-SC results

First of all, let us show a schematic figure of dispersion curves with three subbands occupied and the corresponding distributions of electron wave functions associated with positive k_x for transport in a BQW in an external magnetic field. The results is shown in Fig. 5.6. The energy unit used for the top figure is $\hbar\omega_c$, and in the bottom figure each wave function, $F(y)$, is normalised by dividing by its maximum absolute value in the cross section of the wire. There is almost no flat part of the dispersion curves because the half width of the wire in our calculations is always smaller than or at the same order of the magnetic length. Clearly, we can see that the wave functions are spatially asymmetric due to the Lorenz force. A more important thing is that in the top figure the

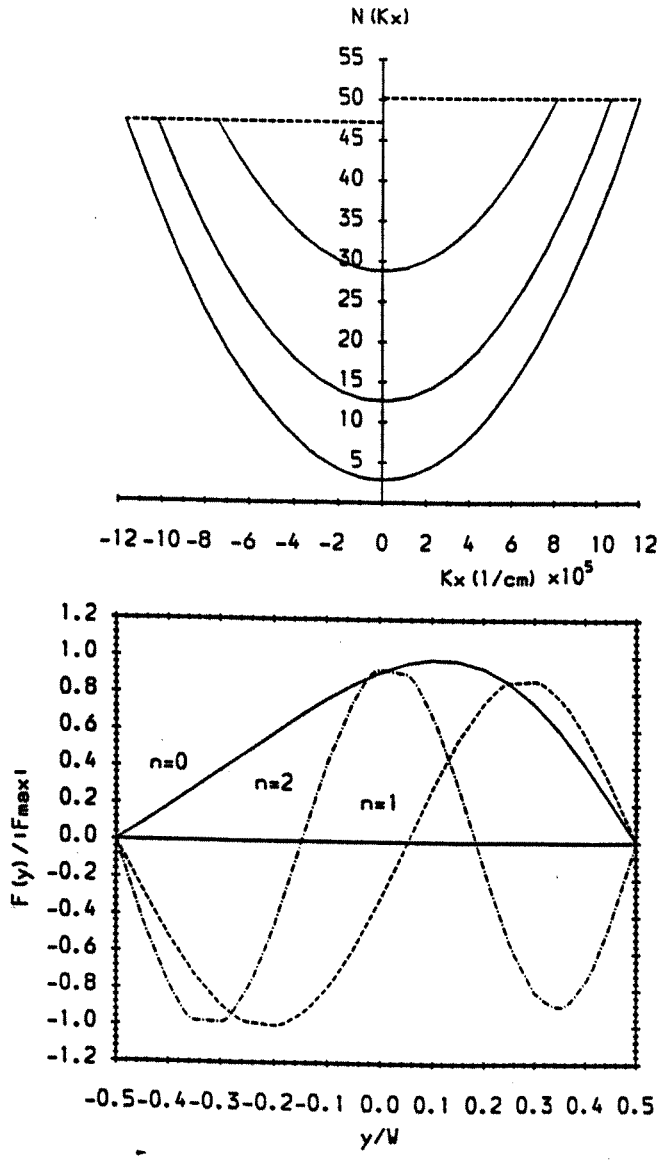

Figure 5.6: Dispersion curves for a transport BQW in a magnetic field with three subbands occupied (top). The unit for the vertical axis is $\hbar\omega_c$. The corresponding distributions of electron wave functions, $F(y)$, (bottom). Each of them is normalised by dividing by its maximum absolute value across the wire.

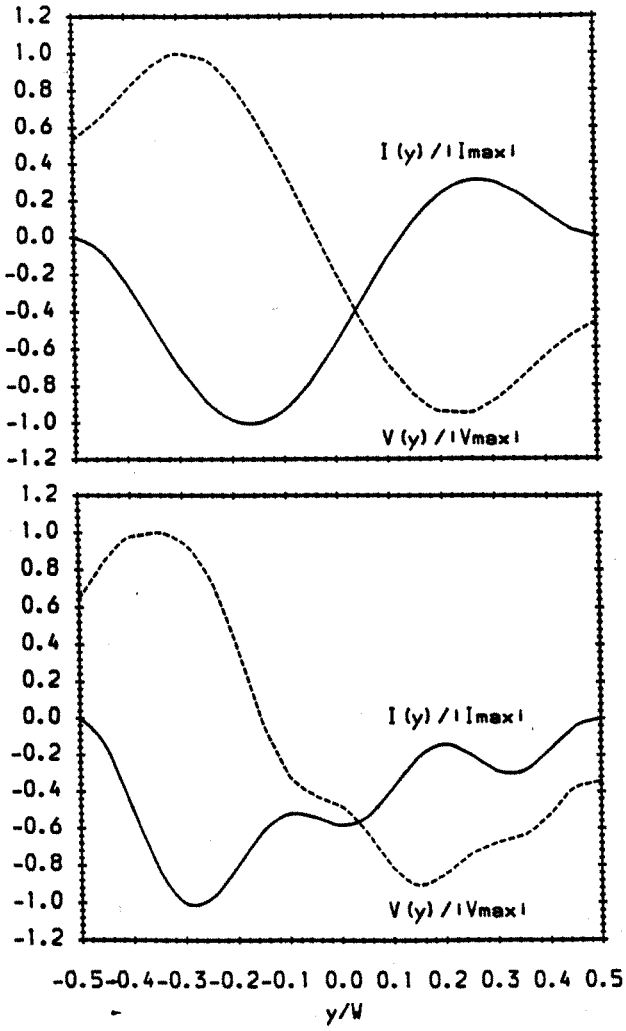

Figure 5.7: Normalised current density, $I(y)$, and EHP, $V(y)$, distributions when there is one subband occupied (top) and three subband occupied (bottom). The system is the same as in Fig. 5.6.

bottom of each subband is not an integer times of $\hbar\omega_c$ and the gap between adjacent subbands increases as the subband index increases. This is an effect of the hard wall confinement. In the next schematic figure, Fig. 5.7, we show the current density, $I(y)$, and the EHP, $V(y)$, distributions for the same system. The results in the top figure is for a strong magnetic field and only one subband is occupied, while in the bottom figure the magnetic field is weak and there are three subbands occupied. Each of the curve in Fig. 5.7 is normalised by dividing by its maximum absolute value across the wire. From these two figures, we can have a qualitative picture of a system with a fixed density of electrons. The parameters in the calculations are not important and exclusion of the Coulomb interaction only changes the results quantitatively.

We show the calculated electron wave functions, $\phi_i(y)$, in Fig. 5.8; the change of electron density in an applied magnetic field, $d(y)$, in Fig. 5.9; the EHP, $v(y)$, in Fig. 5.10; the LCP, $\mu(y)$, in Fig. 5.11; and current density, $j(y)$, in Fig. 5.12. The parameters we use here are $W = 100$ nm and $n_s = 4 \times 10^{14}$ m^{-2} for a GaAs BQW. The solid line and the dashed line are the results for the SC (interacting electrons) and the non-SC (non-interacting electrons) cases respectively. The top parts in each figure are for $B = 0.025$ T when there are two subbands occupied, while the bottom parts are for $B = 1.0$ T and there is only one subband occupied. There is no much difference for the electron wave functions between the two cases, as shown in Fig. 5.8. Only when $B = 1.0$ T the SC wave function spreads a little bit more than the non-SC one due to the Coulomb interactions between electrons. This confirms that the effect of an external magnetic field on the total SC effective single electron potential can be treated as a perturbation [47]. From Fig. 5.9 we see that the change of electron density in a magnetic field does show the difference between the SC and the non-SC cases. The magnitude in the non-SC case is nearly two times of the SC case. Consequently, the non-SC EHP difference between the two edges of the wire is larger than the SC difference of the EHP, as shown in Fig. 5.10, so does the corresponding $R_{\rm EHP}$. It should be pointed out that the EHP takes different values at the two edges of the wire when $B = 1.0$ T, and the reason that we

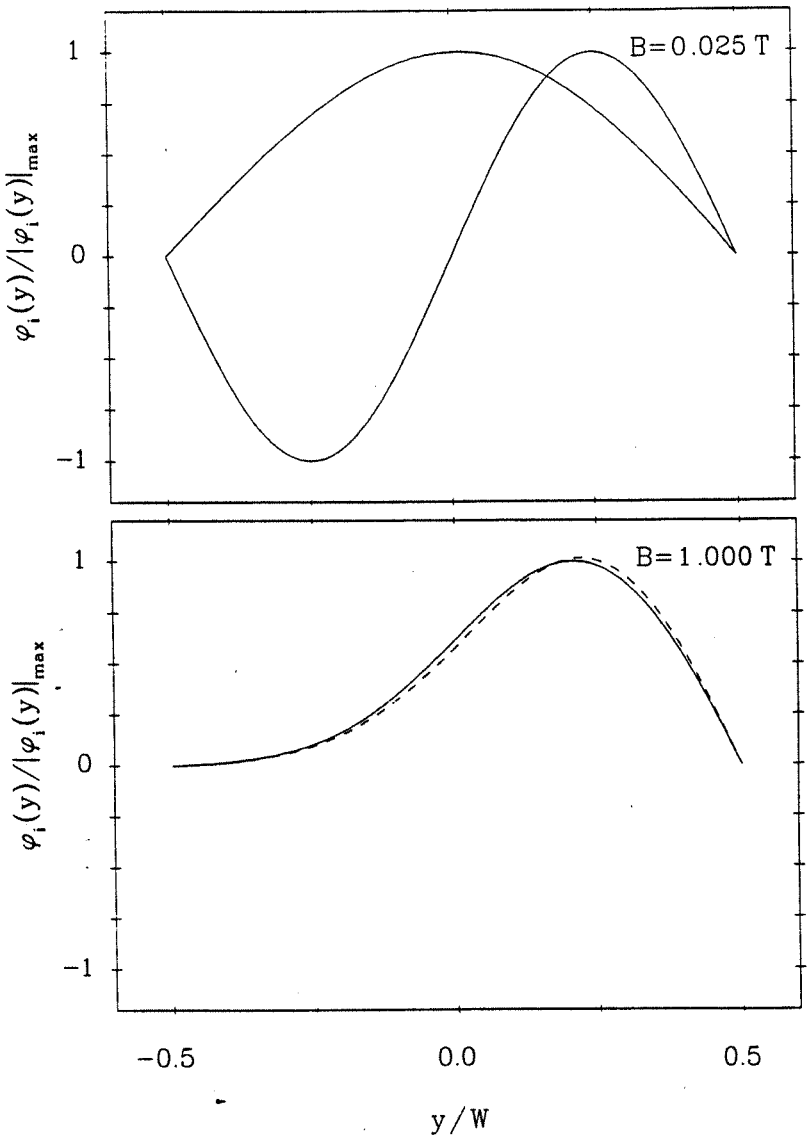

Figure 5.8: The SC (solid line) and the non-SC (dashed line) electron wave functions, $\phi_i(y)$, for a BQW with $W = 100$ nm and $n_s = 4 \times 10^{14}$ m^{-2}. There are two subbands occupied when $B = 0.025$ T (top), while there is only one subband occupied when $B = 1.0$ T (bottom).

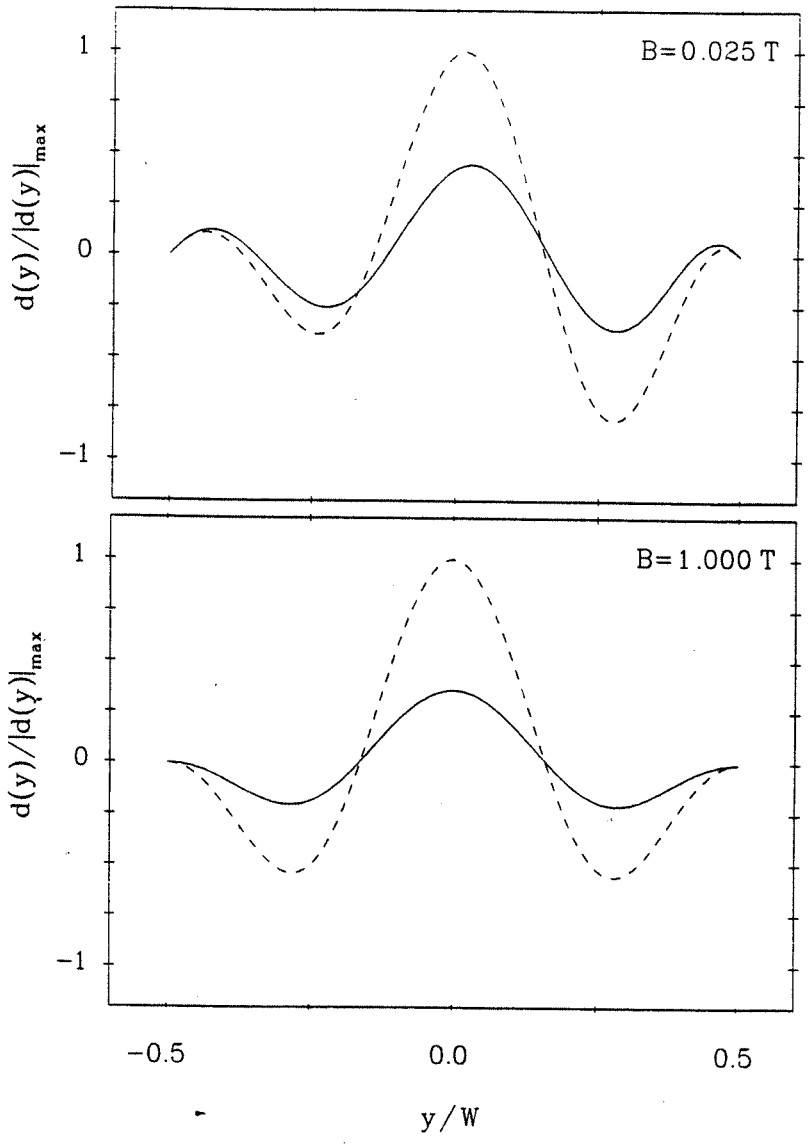

Figure 5.9: The SC (solid line) and the non-SC (dashed line) changes of electron density, $d(y)$, for a BQW with $W = 100$ nm and $n_s = 4 \times 10^{14}$ m^{-2}. There are two subbands occupied when $B = 0.025$ T (top), while there is only one subband occupied when $B = 1.0$ T (bottom).

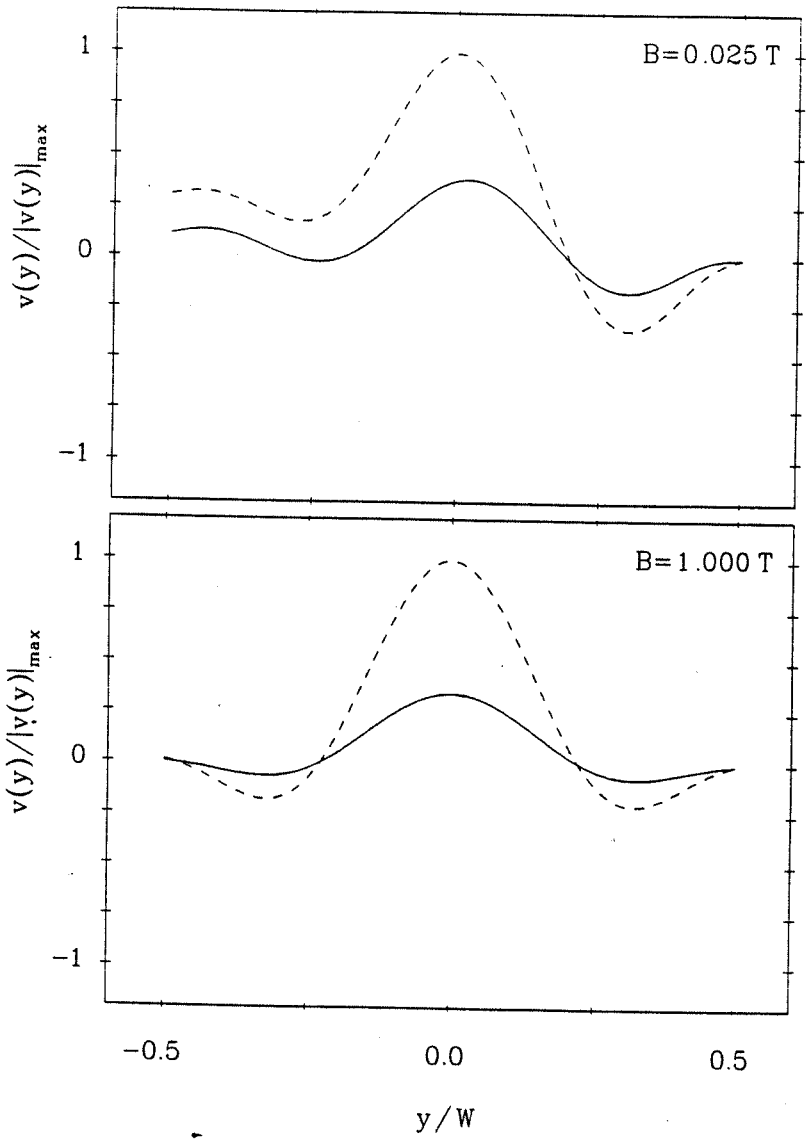

Figure 5.10: The SC (solid line) and the non-SC (dashed line) EHPs, $v(y)$, for a BQW with $W = 100$ nm and $n_s = 4 \times 10^{14}$ m^{-2}. There are two subbands occupied when $B = 0.025$ T (top), while there is only one subband occupied when $B = 1.0$ T (bottom).

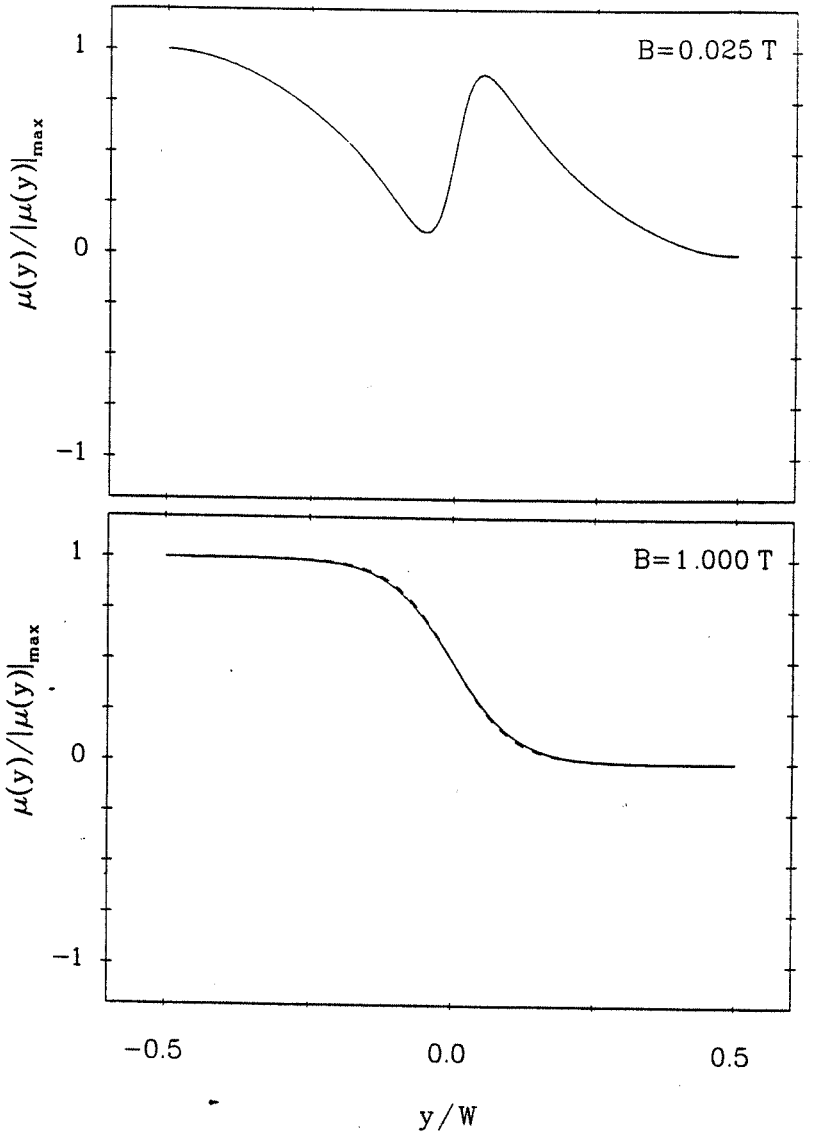

Figure 5.11: The SC (solid line) and the non-SC (dashed line) LCPs, $\mu(y)$, for a BQW with $W = 100$ nm and $n_s = 4 \times 10^{14}$ m^{-2}. There are two subbands occupied when $B = 0.025$ T (top), while there is only one subband occupied when $B = 1.0$ T (bottom).

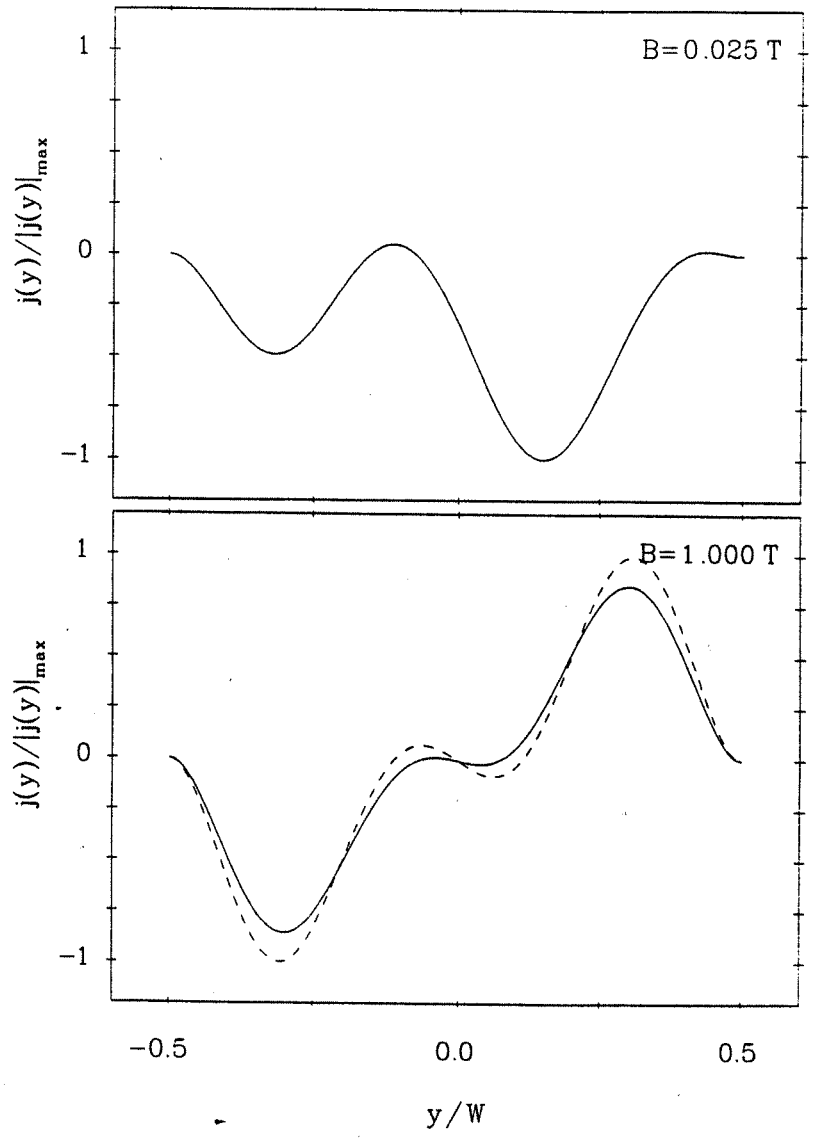

Figure 5.12: The SC (solid line) and the non-SC (dashed line) current densities, $j(y)$, for a BQW with $W = 100$ nm and $n_s = 4 \times 10^{14}$ m^{-2}. There are two subbands occupied when $B = 0.025$ T (top), while there is only one subband occupied when $B = 1.0$ T (bottom).

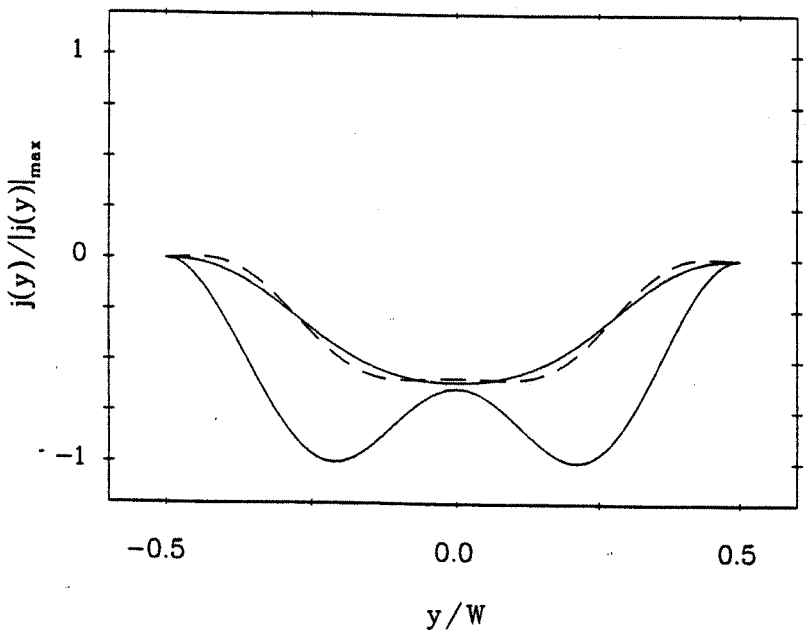

Figure 5.13: The net current density associated with the case of Fig. 5.12. The solid curve with two minima is the SC and non-SC results at $B = 0.025$ T, while the solid and dashed curves with only one minimum are the SC and non-SC results at $B = 1.0$ T respectively.

cannot see this very clearly in the bottom part of Fig. 5.10 is that the size of the figure is too small. As for the LCPs in Fig. 5.11, we can expect that there would no much difference between the SC and the non-SC cases because there is not much difference between the corresponding wave functions. However, the SC current density at $B = 1.0$ T is about 10 per cent smaller than the non-SC one as shown in Fig. 5.12. Again, we attribute this reduction to the wave function broadening due to the Coulomb interactions between electrons. From the bottom figure in Fig. 5.12, we see that the current density does show the same pattern as predicated in Ref. [136] although there are no flat parts in between the current density peaks because of the narrow width of our wire.

Finally, we take away the anti-symmetric parts in Fig. 5.12 and plot the remaining symmetric current densities. As shown in Fig. 5.13, the solid line with two minima is the SC result at $B = 0.025$ T with two subbands occupied and the non-SC result is the same. The solid and dashed lines with only one minimum are the SC and the non-SC results at $B = 1.0$ T with only one subband occupied. Careful calculations show that the net current with two subbands occupied is just twice the net current when there is only one subband occupied. In the other words, each conducting channel contributes the same amount to the total net current as we expect.

5.3.4 Scaling behaviour of the Hall resistances

From Eq. (5.4), we know that the same set of Fermi wave numbers in a given magnetic field can be obtained either by changing the width of a BQW, W, with fixed electron density, n_s, or by changing n_s with fixed W. First, we fix $B = 0.5$ T for a GaAs BQW and plot the SC resistances versus n_s in Fig. 5.14(a), the SC resistances versus W in Fig. 5.14(b) and the non-SC resistances versus W in Fig. 5.14(c). The circles, squares and crosses refer to $R_{\rm LCP}$, $R_{\rm EHP}$ and the longitudinal resistances in each situations. The fixed n_s in Fig. 5.14(a) and the fixed W in Figs. 5.14(b) and (c) are 100 nm and 2×10^{15} m^{-2} respectively. Again, we see that there are jumps for the non-SC $R_{\rm EHP}$ when a subband depopulates, while the SC $R_{\rm EHP}$ changes smoothly in all the range.

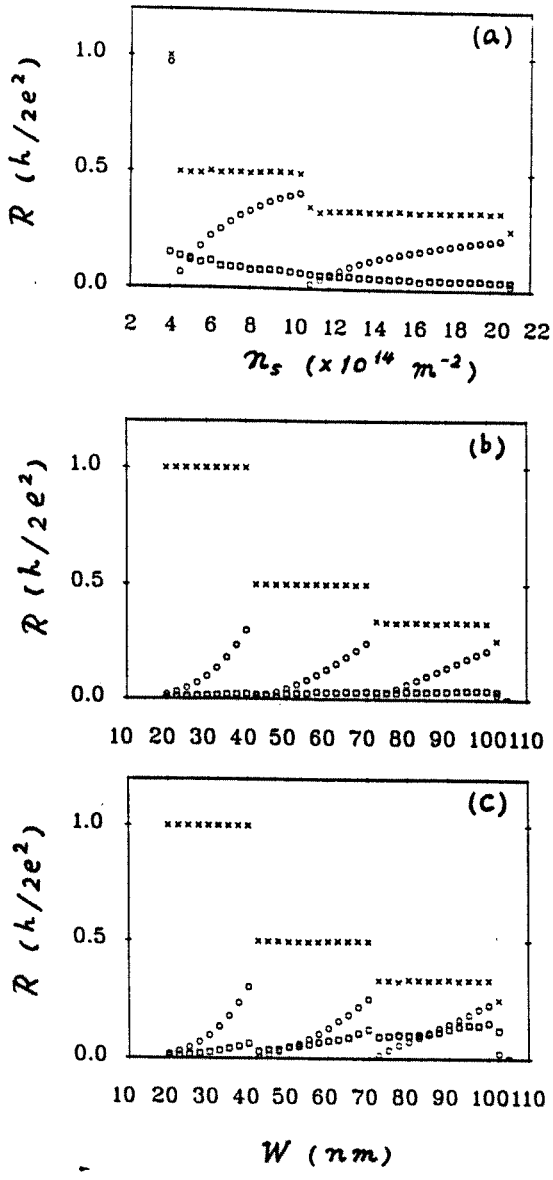

Figure 5.14: The SC resistances versus n_s, (a); the SC resistances versus W, (b); and the non-SC resistances versus W, (c). The circles, squares and crosses refer to $R_{\rm LCP}$, $R_{\rm EHP}$ and the longitudinal resistance in the wire. The parameters are fixed as $W = 100$ nm in (a), $n_s = 2 \times 10^{15}$ m^{-2} in (b) and (c) as well as $B = 0.5$ T for all the three.

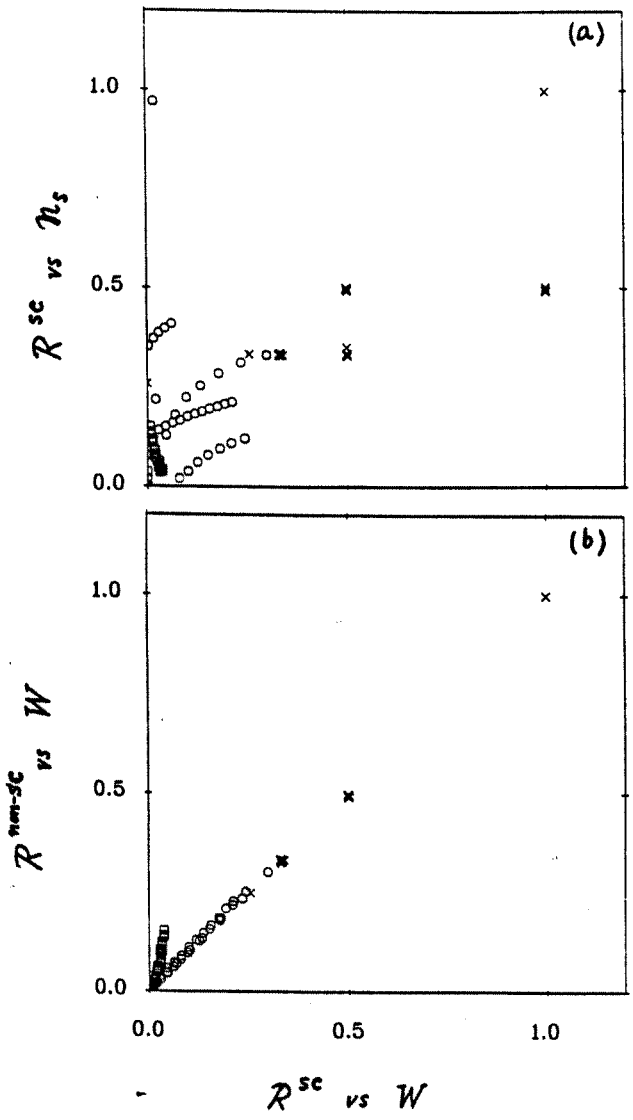

Figure 5.15: (a) The SC resistances versus n_s in the coordinates of the SC resistances versus W; (b) the non-SC resistances versus W in the coordinates of the SC resistances versus W. The circles, squares and crosses refer to R_{LCP}, R_{EHP} and longitudinal resistances.

Now we are going to plot the SC resistances versus n_s against the SC resistances versus W. For comparison, we also plot the non-SC resistances versus W against the SC resistances versus W. The results are shown in Fig. 5.15(a) and (b) respectively, with the circles for $R_{\rm LCP}$, the squares for $R_{\rm EHP}$ and the crosses for the longitudinal resistance along the wire. If these two procedures are equivalent, all the points should be in a line with a slope of 1. From Fig. 5.15(a), we can see that none of these SC resistances can be scaled by each other. This reveals that even for a transport system with the same set of Fermi wave numbers but with different pairs of W and n_s, the electron-electron interactions can be very different. Moreover, Fig. 5.15(b) tells us that $R_{\rm LCP}$ and the longitudinal resistance for the SC and non-SC system with the same W and n_s are, within our calculation accuracy, on the line with a slope of 1, *i.e.* the Coulomb interactions do not affect $R_{\rm LCP}$ and the longitudinal resistance very much in this situation. However, $R_{\rm EHP}$ cannot be simply scaled in this case and the non-SC $R_{\rm EHP}$ increases, rather than decreases as in Fig. 5.15(a), when the SC $R_{\rm EHP}$ increases.

5.3.5 A remark on edge channels

Halperin showed that the Landau levels increase and form the so-called edge states when they approach the edge of a microstructure in an external magnetic field B [50]. Based on this picture, Chklovskii, Shklovskii and Glazman further developed a theory for the edge channels in real space, classifying these channels as compressible or non-compressible [132]. As we have pointed out, the authors did not start from the real self-consistent electrostatic potential as calculated before [43], instead they inserted a hard wall confinement potential and then, based on that, calculated the EHP in the system. This procedure artificially introduces an additional very large amount of Coulomb interactions into a system. Therefore, their picture of the edge channels as due to the effect of self-consistent electrostatic potential is not very convincing. How to describe edge channels in real space remains a problem.

Naturally, we first look the distributions of electron wave functions in real

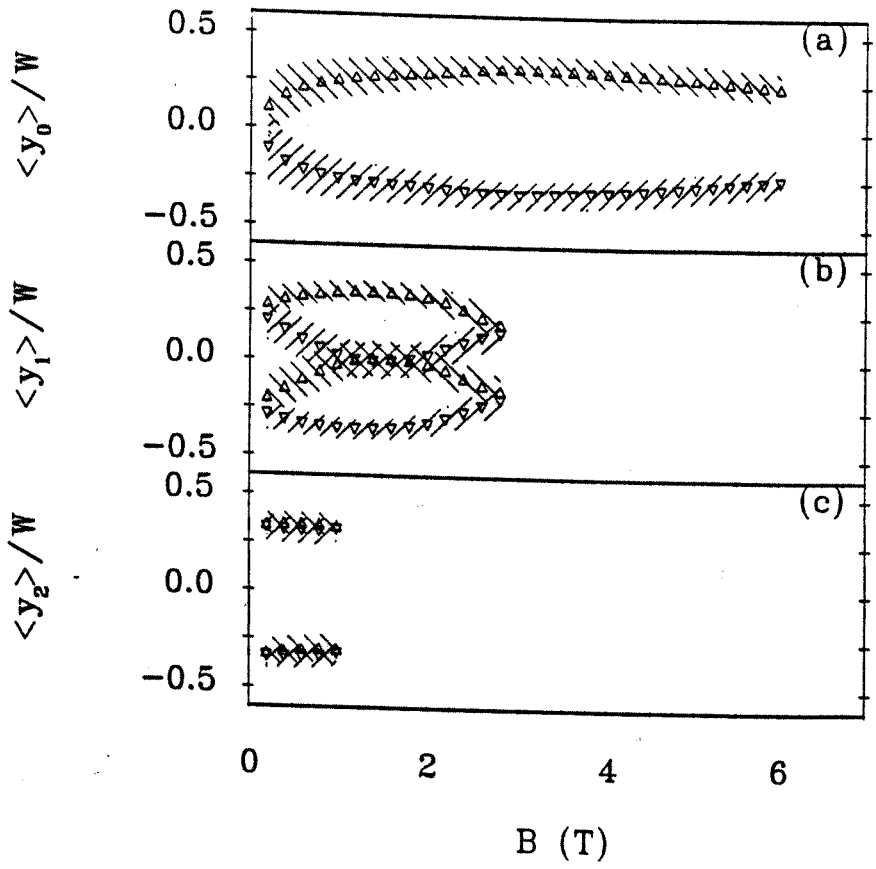

Figure 5.16: The distributions of electron wave functions versus B. Up(down)-triangle refers to the mean position of right(left)-going wave functions and the cross hatch lines sloping down to the right(left) mark the corresponding wave function spread. The width of wire is $W = 100$ nm and the electron densities are $n_s = 14.45 \times 10^{14}$ m^{-2}.

space. We plot our results in Fig. 5.16 for a GaAs BQW with $W = 100$ nm and $n_s = 14.45 \times 10^{14}$ m^{-2}. There are three subbands occupied when B approaches zero and we index them from the ground subband as 0, 1 and 2 respectively. To represent these wave functions we define a convenient mean position $\langle y_n \rangle$ and a half-width $\langle (\Delta y_n^2) \rangle^{1/2}$ in subband n. The up- and down-triangles refer to the mean positions of the wave functions propagating in the positive and negative directions of the x-axis which is parallel to the wire. Furthermore, for $n = 0$, we cross hatch the region lying between $\langle y_n \rangle - \langle (\Delta y_n^2) \rangle^{1/2}$ and $\langle y_n \rangle + \langle (\Delta y_n^2) \rangle^{1/2}$ to indicate the spread of wave functions. While for $n > 0$, we use a renormalised part of the wave function lying between one edge and the node closest to it to calculate the half-width. This gives a better pictorial representations of the electron wave function in the excited subbands near the edges. The calculations here are non-SC because we know the shape of electron wave functions is very close to the SC results. We see clearly from Figs. 5.16(a) and (b) that the mean positions of electron wave function in a BQW does not always tend to the system's edges. It first departs from the centre of the wire as the magnitude of an external magnetic field increases and then comes back towards the centre when the magnitude of the magnetic field is larger than a certain value. There are two main reasons for this kind of behaviour of the mean positions. Firstly, there are two edges in our system. In a one edge system, the mean positions always go towards the edge as the magnetic field increases. Secondly, we fix n_s in our calculations. If we fix the Fermi energy instead of n_s, we will have different results.

Now, we show that the LCP distribution provides a useful description of edge states in real space. Fig. 5.17 shows the distributions of the SC LCP across the wire $W = 100$ nm versus B. In Fig. 5.17, (a), (b) and (c) are for $n_s = 2$, 4 and 8×10^{14} m^{-2} respectively. The LCP in the figure is represented by $\Delta\mu(y)/\Delta\mu = (\mu(y) - \mu(W/2))/(\mu(-W/2) - \mu(W/2))$. The isothermal compressibility, κ, is defined as $\kappa = -(\partial V/\partial P)_{T,N}/V$, where V is the volume of a system, P is the pressure applied on the system, T is the system temperature and N is the number of particles in the system. For such a system with its temperature

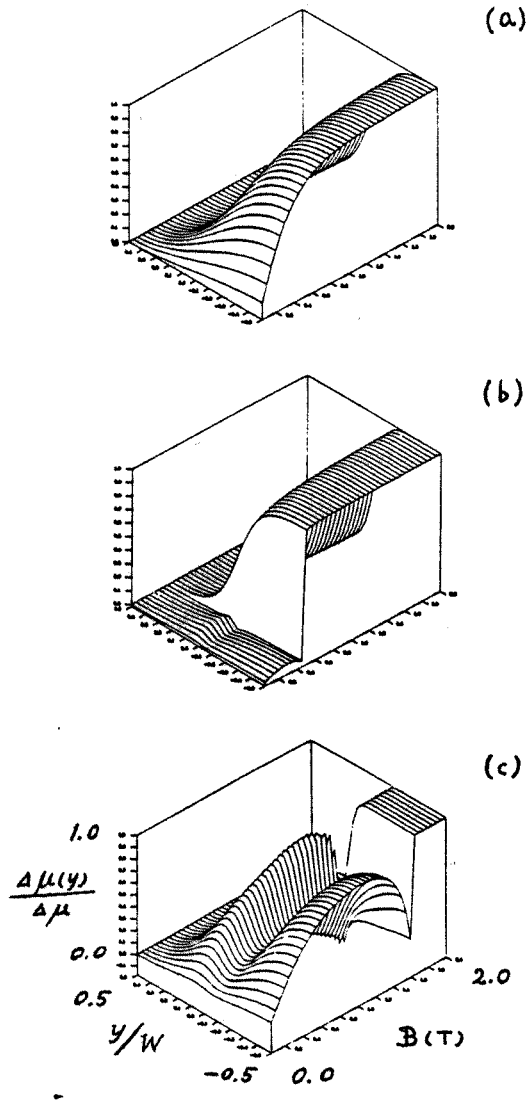

Figure 5.17: The SC LCP distributions across a BQW versus B. (a) $n_s = 2,0 \times 10^{14}$ m^{-2}; (b) $n_s = 4.0 \times 10^{14}$ m^{-2}; (c) $n_s = 8.0 \times 10^{14}$ m^{-2}. The LCP is represented by $\Delta\mu(y)/\Delta\mu = (\mu(y) - \mu(W/2))/(\mu(-W/2) - \mu(W/2))$. All the scales and $W = 100$ nm are the same for (a), (b) and (c).

and number of particles fixed, in our case $T = 0$ K, we have $Nd\mu = VdP$ so that $\kappa = -(\partial V/\partial\mu)_{T,N}/N$. If we consider every site in the system to be in a local quasi-equilibrium state which is described by the LCP, the compressibility across the wire can be express as $\kappa = -(\partial y/\partial\mu(y))_{T,N}/N$. Hence, the flat parts of $\mu(y)$ are compressible while the parts where $\mu(y)$ rapidly varies are incompressible. Combining with the current density distributions in Fig. 5.12, we find that compressible parts are current-carrying parts and they give us a picture of edge channels.

5.3.6 The case of two parallel BQWs

Before we end this chapter, we would like to present the SC results for the resistances of a transport GaAs BQW when there is another identical transport GaAs BQW lying parallel in a distance in the same magnetic field. The amount of current is the same in each wire, but the currents can be in the same direction or the other. There is no hopping between these two wires, and the only interaction between them is via the EHP which is calculated self-consistently for both wires. Change of relative direction of the currents results different EHP, and because of this, we expect to see some differences between the two cases which are individually different from the single wire case. The resistances versus B are shown in Fig. 5.18. The width of the wires and the nearest distance between them are all set to be 100 nm. In Fig. 5.18(a) and (b), $n_s = 2.0 \times 10^{14}$ m^{-2}; while in Fig. 5.18(c) and (d), $n_s = 4.0 \times 10^{14}$ m^{-2}. The currents are in the same direction in Fig. 5.18(a) and (c), and in the opposite directions in Fig. 5.18(b) and (d). The circles, squares and crosses refer to $R_{\rm LCP}$, $R_{\rm EHP}$ and the longitudinal resistance. As shown in Fig. 5.18, the change of current direction does not affect $R_{\rm LCP}$ and the longitudinal resistance very much, but we can see that $R_{\rm EHP}$ changes significantly, as we expect. It decreases rapidly when B becomes large in the cases where the currents are in the same direction, as shown in Fig. 5.18(a) and (c). On the other hand, $R_{\rm EHP}$ increases rapidly when B becomes large in the cases where the currents are in the opposite directions, as shown in Fig. 5.18(b) and (d). In the region $0 < B < 1.2$ T, $R_{\rm EHP}$ also

behaves quite different from the weak linear dependence on B in the case there is only one BQW, and it changes rapidly rather smoothly when a subband is depopulated.

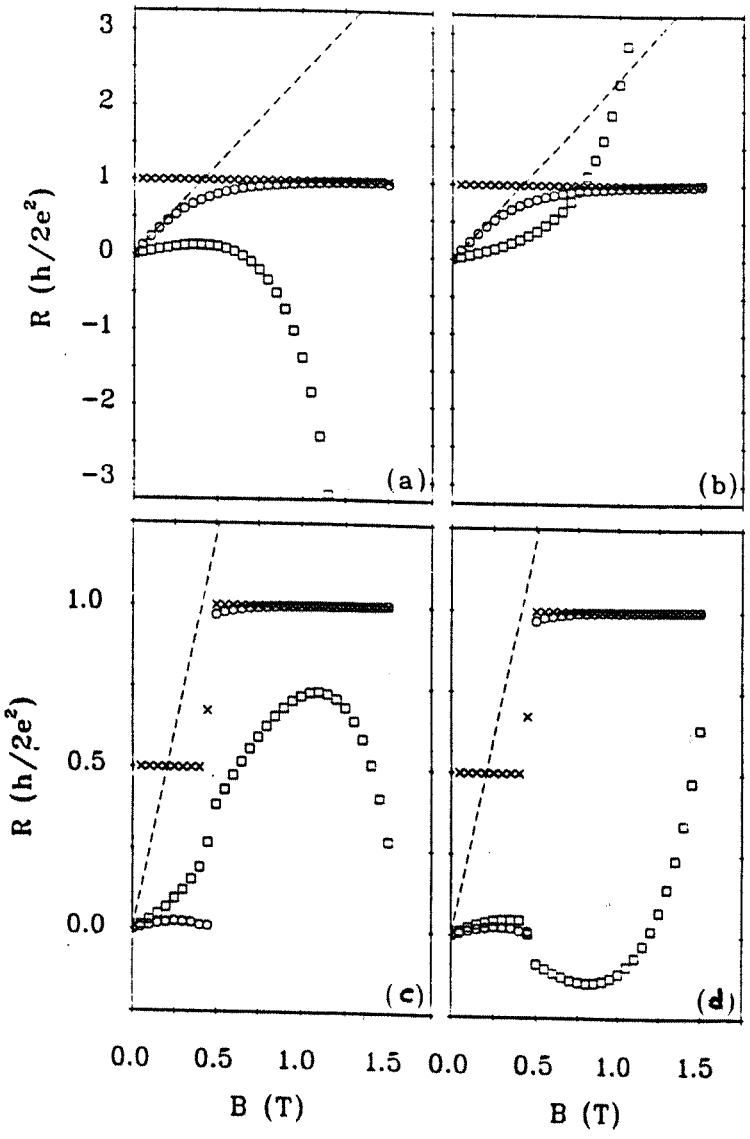

Figure 5.18: The SC R_{LCP} (circles) , R_{EHP} (squares) and the longitudinal resistance (crosses) versus B. Another identical BQW is placed parallel at a distance of 100 nm; it carries a current of the same magnitude in either the same direction, (a) and (c), or in the opposite direction, (b) and (d). The width of the BQWs is $W = 100$ nm. $n_s = 2.0 \times 10^{14}$ m^{-2} in (a) and (b); $n_s = 4.0 \times 10^{14}$ m^{-2} in (c) and (d). The dashed lines are corresponding classical results.

Chapter 6

Quenching of the IIHQE

6.1 Introduction

Recently, particular attention has been given to the behaviour of the QHE in weak magnetic fields, *e.g.* quenching of the quantum Hall resistance and the last Hall plateau [137, 138, 139, 140] as well as the bend resistance in a four terminal case [141, 142, 143]. Much theoretical effort has been devoted to understanding these phenomena. Microscopic calculations of a Q1D electron gas model which ignore significant density of states and Coulomb interaction effects in the weak-coupling limit failed to show quenching [99, 100]. SC calculations of the QHR associated with the electrostatic potential gave only a linear dependence on magnetic field as in the classical case [129]. In the strong coupling regime, quenching of the QHR has been obtained theoretically when there are resonant states involved [124, 144]. Other investigations suggest that quenching is due to a geometrical property of the structure and is not intrinsic to the Q1D limit even with strongly coupled probes [145]. They also demonstrate that smoothing the corners of the structure suppresses the QHR [146]. Assuming a realistic confining potential with soft boundaries provides a detailed explanation of many experimental results via classical trajectories [126]. However, very recent experimental results show that there *is* quenching of the QHR of a quantum wire in the weak coupling limit [123].

6.2 Our results

We present SC calculations of $R_{\rm LCP}$ in a uniform ballistic wire [147]. The following specific results are obtained: (1) quenching of the $R_{\rm LCP}$ is intrinsic in the weak coupling limit, (2) it is due to the overlap of opposite-going wave functions, (3) quenching happens intermittently as the electron density increases, and (4) R_{EHP} is closely linear in the magnetic field B in spite of subband depopulation effects.

Before we go into details, let us first distinguish two kinds of intrinsic Hall resistance in a quantum wire. One is $R_{\rm EHP}$, defined as the EHP difference between the two edges of a wire divided by the total current passing through the two terminals. The other, $R_{\rm LCP}$, is obtained by using the LCP difference across the wire instead of electrostatic Hall potential. The EHP is the potential induced by the electrons in the wire to balance the Lorentz force while the LCP is defined as the chemical potential of a reservoir which is connected non-invasively at a particular point in the wire when no net current flows through the contact. We believe that the potential difference measured by conventional weak-coupling current-stopping procedures, as discussed by Engquist and Anderson [70] and Landauer [122], is the LCP difference. We show in the following that it is $R_{\rm LCP}$ which is quenched in a weak magnetic field. $R_{\rm EHP}$ retains the linear dependence on magnetic field which occurs in classical theory.

The system to be considered is the same as we have used in the last chapter, a 2DEG with electron density n_s which is confined in a space of width W in the x-y plane by infinite potential barriers at $y = \pm W/2$. A uniform magnetic field B is applied in the z direction and described in the Landau gauge by writing the vector potential as $\mathbf{A} = (-By, 0, 0)$. Following previous authors [128, 129] and a recent paper by the present authors [133], we introduce an EHP $V(y)$ which is induced by the external magnetic field. We use the same Schrödinger equation and same form for the EHP and LCP as in the last chapter. We notice that there is a difference between the formula of LCP given above and the formula used in Refs. [99, 100] where the factor v_n^{-1} for the density of states at Fermi level is not included. This difference is the primary reason why there

is no quenching in their results.

When the above equations are solved we obtain self-consistent electron wave functions, the distributions of the EHP and the LCP across the wire and two kinds of intrinsic Hall resistance, $R_{\rm EHP}$ and $R_{\rm LCP}$. To interpret the physics which is revealed in the results it is useful to have representations of the electron distributions in the subband wave functions. As we have described in the last chapter, we therefore define a convenient mean position $\langle y_n \rangle$ and a half-width $\langle (\Delta y_n^2) \rangle^{1/2}$ in subband n and cross hatch the region lying between $\langle y_n \rangle - \langle (\Delta y_n^2) \rangle^{1/2}$ and $\langle y_n \rangle + \langle (\Delta y_n^2) \rangle^{1/2}$ to indicate the spread of wave functions. We take $\langle y_n \rangle = \langle n|y|n \rangle$ and $\langle (\Delta y_n^2) \rangle = \langle n|y^2|n \rangle - \langle y_n \rangle^2$. However, when $n > 0$, in evaluating $\langle y_n \rangle$ and $\langle (\Delta y_n^2) \rangle$ we keep only the renormalised part of the wave function lying between a side wall and the node closest to it. This procedure has the merit of producing useful pictorial representations of the electron distributions in the excited subband wave functions while avoiding unhelpful complications due to the nodes and gives a better description of the behaviour of the electron wave functions near the edges which is what determines $R_{\rm LCP}$. In our numerical calculations, we always use the parameters of a GaAs wire [39] of width $w = 100$ nm and we ignore the Zeeman splitting which is a reasonable first approximation in a model calculation for a GaAs system.

Fig. 6.1(a) shows plots against B which indicate the degree of overlap of the oppositely propagating wave functions in the ground subband when $n_s = 2 \times 10^{14}$ m^{-2}. For this electron density only the ground subband is occupied. In this case, the formula for the local chemical potential becomes very simple and the density of states factor cancels out. The departure of the QHR from its quantised value is therefore, entirely due to the overlap of opposite-going wave functions. Data for $\langle y_0 \rangle$ and the wave function spread is given by the up(down) triangles and the cross-hatch lines sloping down to the right(left) for right(left) going wave function respectively. Fig. 6.1(b) gives data for R_L (crosses), $R_{\rm EHP}$ (squares), and $R_{\rm LCP}$ (circles) for the same value of n_s. We see that $R_{\rm LCP}$ increases rapidly as the opposite-going wave functions begin to separate and stays at the quantised value when they are well separated at the

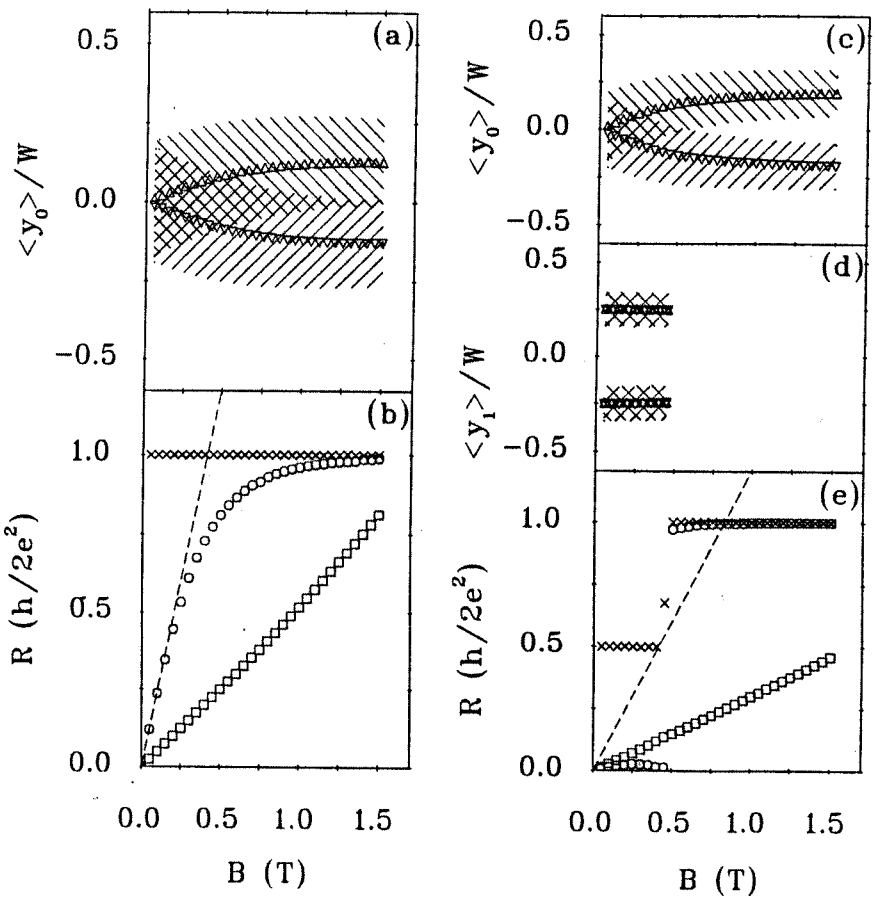

Figure 6.1: Plots showing overlap of the opposite-going wave functions in different subbands as a function of B and the corresponding R_L (crosses) and Hall resistances: R_{EHP} (squares) and R_{LCP} (circles). Up(down)-triangle refers the average position of right(left)-going wave functions and the cross hatch lines sloping down to the right(left) mark the corresponding wave function spread. The width of wire is $W = 100$ nm and the electron densities are $n_s = 2 \times 10^{14}$ m^{-2} in (a) and (b) and $n_s = 4 \times 10^{14}$ m^{-2} in (c), (d), and (e). The dashed lines show the classical Hall resistances.

two edges of the wire.

Figs. 6.1(c) to (e) show corresponding plots when $n_s = 4 \times 10^{14}$ m^{-2}. For this density two subbands are occupied when $B < 0.5$ T but only the ground subband is occupied when $B > 0.5$ T. We chose this n_s to make the Fermi wave number of the uppermost occupied subband much smaller than the others when $B \to 0$ so that the Fermi level is very close to the bottom of it which is flat. Consequently, the closer the Fermi level is to the bottom of a subband the larger is the density of states of that subband at the Fermi level. In this situation, the local chemical potential difference between the two edges of wire is greatly reduced by both the large overlap of the opposite-going wave functions at low B and the significant increase of the density of states of the uppermost occupied subband. Figs. 6.1(c) and (d) show the degree of overlap in the $n = 0$ and $n = 1$ subbands respectively. Fig. 6.1(e) shows that R_{LCP} is quenched when $B < 0.5$ T and Figs. 6.1(c) and (d) confirm that the quenching is associated with severe overlap of the $n = 1$ wave functions while the $n = 0$ wave functions are separating as they did in Fig. 6.1(a). The dashed lines in Figs. 6.1(b) and (e) show the behaviour of the classical Hall resistance. As soon as the second subband is depopulated, R_{LCP} jumps to the quantised value because the opposite-going $n = 0$ wave functions are separated at the two edges.

We see that the LCP at a wire edge is determined by the values there of the opposite-going electron wave functions of all of the occupied subbands. Increasing the overlap at the edges decreases the LCP difference between the edges. The singularity of density of states at the bottom of a subband enhances this effect enormously. In the limit, $B \to 0$, the left- and right-going wave functions coincide and the LCP difference across the wire is zero. For small B, there will consequently be almost complete quenching of R_{LCP} because the opposite-going wave functions of all the occupied subbands overlap heavily at the edges. When the opposite-going wave functions of any one subband are separated, the level of quenching of R_{LCP} is reduced. Finally, when every pair of opposite-going wave functions are well separated, the LCP difference approaches the chemical potential difference between the two ends of wire and

the $R_{\rm LCP}$ is almost exactly quantised.

We always suppose in the calculations described above that n_s is fixed. Consequently, when only the ground subband is occupied, the corresponding Fermi wave number k_{F0} is also fixed. In that case, increasing B from zero simply separates the wave functions. On the other hand, when two subbands are occupied, increasing B increases k_{F0} but *reduces* the Fermi wave number k_{F1} in the second subband. For $n_s = 4 \times 10^{14}$ m^{-2}, $k_{F1} \ll k_{F0}$. Hence, when B is increased the $n = 0$ wave functions separate quickly but the $n = 1$ wave functions do not with the result that $R_{\rm LCP}$ is quenched.

The behaviour when B is fixed and n_s is changed is also interesting. Results are shown in Fig. 6.2 for $B = 0.1$ T and $B = 0.5$ T in Figs. 6.2 (a)-(d) and Figs. 6.2(e)-(h) respectively. When $B = 0.1$ T the opposite-going wave functions of every occupied subband overlap heavily as shown in Figs. 6.2(a)-(c). Consequently, in Fig. 6.2(d) $R_{\rm LCP}$ is always small. When $B = 0.5$ T we see from Figs. 6.2(e)-(g) that the overlap between the opposite-going wave functions in each occupied subband is reduced and the wave functions separate as n_s (and consequently k_{Fn}) increases. Consequently, $R_{\rm LCP}$ in Fig. 6.2(h) increases quickly with n_s as each subband is traversed.

We see from Fig. 6.2 that $R_{\rm LCP}$ is quenched intermittently as n_s varies. This effect has been seen experimentally [140] and theoretically in a strong-coupling case [144]. To investigate it in more detail we show in Fig. 3 plots of the various Hall resistances against B for several different values of n_s. The graphical notation is the same as in Figs. 6.1 and 6.2. In Fig. 6.3(a) $n_s = 1.0 \times 10^{14}$ m^{-2}. Only the ground subband is occupied and k_{F0} is large enough to prevent overlap so that there is no quenching. This is also true in Fig. 6.3(b) for which $n_s = 3.0 \times 10^{14}$ m^{-2}. However, because k_{F0} is now larger, $R_{\rm LCP}$ increases more rapidly towards $h/2e^2$. In Fig. 6.3(c) $n_s = 4.5 \times 10^{14}$ m^{-2}. Only the ground subband is occupied when $B > 0.7$ T but n_s is now large enough for the $n = 1$ subband to be occupied as well when $B < 0.7$ T. We see that quenching sets in this regime because k_{F1} is small and the wave functions in the $n = 1$ subband overlap. In Fig. 3(d) we have increased n_s to 9.5×10^{14} m^{-2}

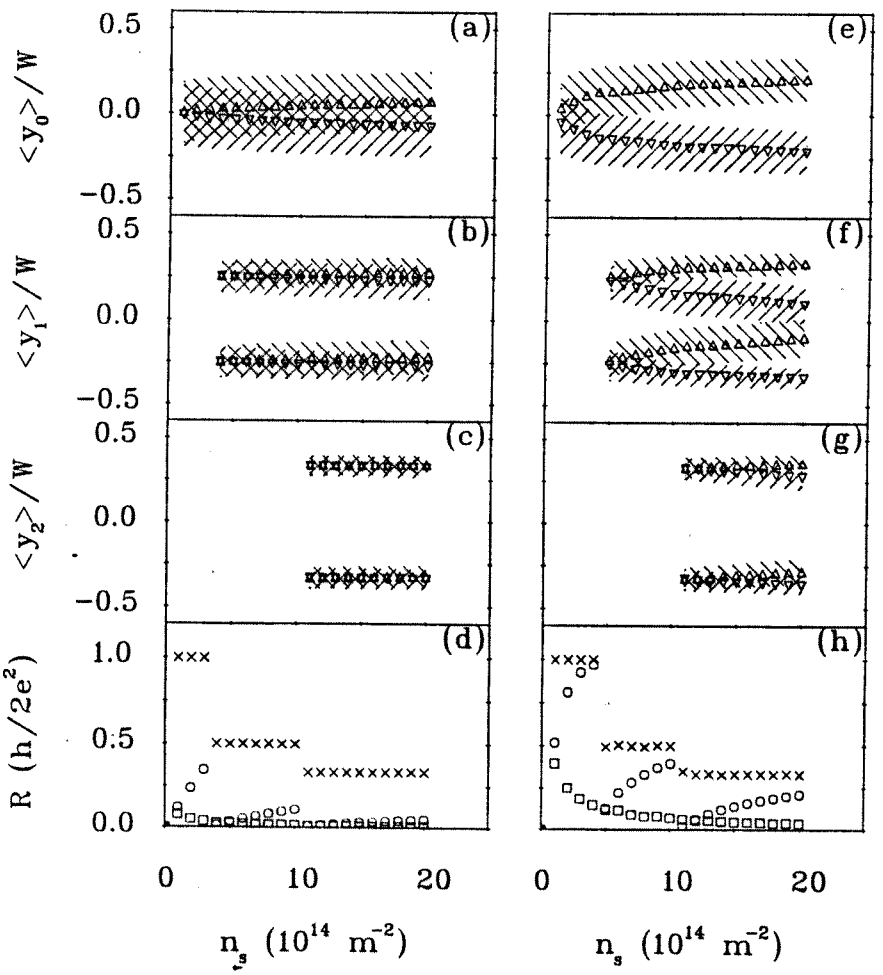

Figure 6.2: Plots showing the dependence on n_s of the opposite-going wave functions in different subbands and the corresponding Hall resistances. The width of the wire and the notation is the same as in Fig. 6.1; B = 0.1 T in (a)-(d) and 0.5 T in (e)-(h).

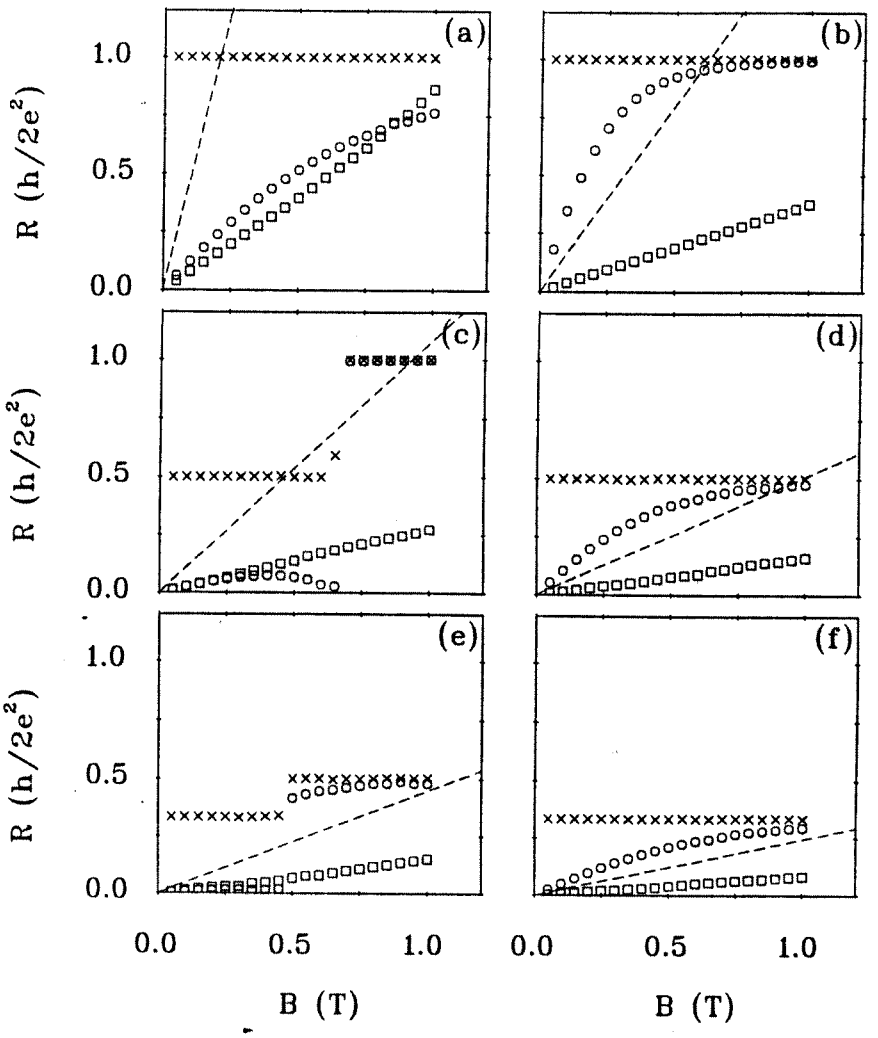

Figure 6.3: Plots showing R_{EHP} (squares), R_{LCP} (circles), and R_L (crosses) vs. B for $n_s = 10^{14}$ m^{-2} $\times$ 1.0 (a), 3.0 (b), 4.5 (c), 9.5 (d), 10.8 (e), and 19.8 (f). The width of the wire and the notation is the same as in Fig. 6.1. The dashed lines show classical Hall resistance.

to ensure that both subbands remain occupied for all B and both k_{F0} and k_{F1} are large enough to prevent significant overlap. Consequently, R_{LCP} is not quenched. In Fig. 6.3(e) $n_s = 10.8 \times 10^{14}$ m^{-2} and three subbands are occupied when $B < 0.5$ T. As would be expected, the quenching behaviour is similar to that shown in Fig. 6.2(c). Finally, in Fig. 6.3(f), we have increased n_s to 19.8×10^{14} m^{-2} so that all three subbands remain occupied for all B with relatively large Fermi wave numbers. The situation is similar to that shown in Fig. 3(d) and quenching is suppressed.

Chapter 7

Noninvasive measurement of the IIQHE

7.1 Introduction

To study the electronic transport properties of a system, it is normal to use at least four leads, attaching two pairs of leads to the system to measure the current passing through it and the voltage drop across it. In the macroscopic regime, the scale of system is much larger than the scale of the measurement leads. Consequently, this approach has very little effect on the system being measured and the measurement results can be used to fully characterise the system itself. This desirable situation has changed with the rapid development of semiconductor fabrication techniques which make it possible to investigate 2DEG microstructures. In this case both current and voltage leads become an inseparable part of the system being measured. Moreover, the dimensions of the part being measured and the measurement leads are of the same order and can be comparable with the de Broglie wavelength of the electron propagating in the system. Many novel phenomena are observed in this situation. They are attributed to this new partnership between the system being measured and the leads and are explained successfully by using L-B formulae which reveal the relationship of resistance to transmission coefficient between leads [62, 75]. Büttiker has proposed a general formula to determine the chemical potential

measured by a voltage lead through a current-stop procedure [75, 80]:

$$\mu_l = \frac{T_{ls}\mu_s + T_{ld}\mu_d}{T_{ls} + T_{ld}} \tag{7.1}$$

where $T_{ls}(T_{ld})$ is the sum of all the transmission coefficients for a carrier incident in lead $s(d)$ to be transmitted to lead l and the subscripts l, s, and d denote voltage, source, and drain leads respectively.

A problem arises when one asks how to determine the *intrinsic* resistance of such a microstructure system, *i.e.* its *own* response to the change of environment [133]. To do this, it is necessary to study the effect of the leads on the resistance measurement in detail. The two kinds of leads (current and voltage) have different interactions with the system. Current leads function as sources and drains which respectively inject electrons into and collect them from the system being measured. Voltage leads do not have any net electron exchange with the system; they determine the potential being measured by a current-stop procedure. Furthermore, different shapes of leads give different results. To be definite we consider ideal current leads, *i.e.* hard wall ballistic electron waveguides which become an integral part of a system. (They are used as filters [148] to get rid of fluctuations, evanescent modes, etc. coming from the reservoirs and introduce standard propagating modes of electrons into the system.) The injection modes are determined by the character of the ideal leads only. If the shape of the current leads are fixed we have only to consider the effect of the voltage leads.

There is no confusion when we use just one pair of leads to measure both the current passing through a system and the "voltage drop" across it. The result of such measurements is a conventional longitudinal resistance. When we have separate pairs of leads to measure current and "voltage drop", which is essential in studies of the QHE, the resistance measured reflects the behaviour of the original system plus a pair of voltage leads and is voltage-lead dependent. We are not able to isolate the contribution from the system being measured in the total signal. The only way to solve this problem is to reduce the coupling between the system to be measured and the voltage leads. The weaker the coupling, the less the measurement result is effected by the measurement

process. However, we know that there is no way to measure a system without *some* perturbation of the system being measured. What we must do, then, is to make the coupling small enough so that the measured resistance does not change within the accuracy of the measurement instrument when the coupling decreases further. Then, in this sense, the measurement is non-invasive and the measured resistance can be regarded as intrinsic to the system which we measure.

Many papers discuss methods of making non-invasive voltage leads. For technical reasons, most of the studies concentrate on the geometrical edge of a 2DEG microstructure. Li and Thouless suggest using a scanning-tunnelling-microscope tip as a weakly coupled voltage lead to detect the electrostatic potential response in the QHE at an etched edge [129]. Field *et al.* use a separate quantum point contact sited at the side of a gated edge to achieve non-invasive measurement of electrostatic potential [149]. When we work out the resistance of a system, however, we need to know the chemical potential difference rather the electrostatic potential difference between two points, as is stressed by Engquist and Anderson [70]. Experimental attempts to measure resistance in the weak coupling limit have been made recently by Shepard *et al.* [123]. It is much more difficult to determine the chemical potential at a certain point of a transport system. The main reason is that the chemical potential in a system is normally not well defined when there is a net current flowing through it. Many suggestions have been made about how to define this quantity locally in a system away from thermal equilibrium [70, 97, 102]. They all lead to the same chemical potential and average electron occupation in an equilibrium system as has been pointed out by Landauer [93, 92]. Different procedures for non-invasive measurement have been suggested, *e.g.* phase-insensitive [70] and phase-sensitive [150]. They give different results when there is a net current passing through the system with reflections.

To avoid of these problems, a particular formula has been introduced through an assumption of a virtual contact measurement procedure for both single and multi-mode two-terminal cases by Entin-Wohlman *et al.* [97] and Imry [98]

respectively. The advantage of this formula is that it defines a local chemical potential (LCP) in a non-equilibrium system so that we can *calculate* the resistance between any two points in a system in which net currents are flowing without introducing voltage leads. Büttiker derives a similar expression for a self-consistent electrostatic potential [80]. The same formula for the LCP is obtained in a general multi-mode and multi-terminal case by using only the assumptions inherent in L-B formulas [102]. It is

$$\mu(\mathbf{r}) = \frac{\sum_t p_t \mu_t}{\sum_t p_t} \tag{7.2}$$

where $p_t = \sum_m |\psi_{tm}(\mathbf{r})|^2 / v_{tm}$. Here t labels the leads feeding the microstructure, v_{tm} is the group velocity of mode m in lead t and $\psi_{tm}(\mathbf{r})$ is the total wave function generated by an incident wave of unit amplitude in mode m in lead t. We would like to stress that the LCP is phase-sensitive. The phase relation between the incident wave and the reflected wave is fully considered in the calculation of the wave function for the whole system. Moreover, the resistance determined by the LCP is non-local resistance which is not normally additive.

7.2 Our model calculations: analytical results

We model a non-invasive measurement procedure in a system consisting of a quasi-one-dimensional ballistic quantum wire (BQW) and two voltage leads [151]. The current leads are part of the BQW. Transmission coefficients are calculated and the chemical potential as well as the Hall resistance associated with it are obtained using Büttiker's formula, Eq. (7.1). In the strong confinement limit, we prove analytically that Büttiker's formula is equivalent to the formula for the LCP, Eq. (7.2), and the Hall resistance approaches the intrinsic Hall resistance defined by the LCP [133]. Numerical results are given to show how the character of the voltage leads affects the Hall resistance and to which every mode therein makes a non-negligible contribution.

The main part of our model system is a non-interacting 2DEG with electron density n_s which is confined in a space of width W in the x-y plane by infinite

potential barriers at $y = \pm W/2$. The two ends of the BQW are connected to the electron reservoirs with chemical potential μ_s (at the end where $x < 0$) and μ_d (at the end where $x > 0$) respectively. When $\mu_s \neq \mu_d$, there is a net current traversing the BQW. To model a four-terminal measurement of the Hall resistance, we use the weak-link model studied by Peeters [99] and later by Akera and Ando [100] to put two voltage leads on the two sides of the wire in the x-y plane and parallel to the y-axis. The confinement potential in the voltage leads has the form of $m^*\omega_p^2 x^2/2$ and is characterised by an equivalent magnetic field $B_p = m^*\omega_p/e$ where m^* is the effective mass of electron. We assume these two types of confinements for the BQW and the voltage leads respectively because they are mathematically simple and are close to the calculated self-consistent potential profiles for the relatively wide and narrow BQWs in which the Fermi energy is the same [43] which is the case when we explore the strong confinement limit in the voltage leads. Moreover, two identical tunnelling barriers with heights V_b and widths b are symmetrically placed between the wire and the ends of the voltage leads. The amount of current leaking into the voltage leads can be made very small by increasing the product $V_b b$ so that we can approach the non-invasive limit defined above. For convenience in the calculations, delta functions of area $V_b b$ are located at $y = \pm W/2$ to describe potential energies of the tunnelling barriers as $V_b b\delta(y \mp W/2)$.

A magnetic field B is applied in the direction perpendicular to the x-y plane and is described in the Landau gauge by writing the vector potential as $\mathbf{A} = (-By, 0, 0)$ for the BQW and as $\mathbf{A} = (0, Bx, 0)$ for the voltage leads. Taking account of the gauge difference between the two regions, the tunnelling wave function of an electron from the BQW to the voltage lead at $y = W/2 + \epsilon$ ($\epsilon \to 0^+$) is

$$\psi^{(n\pm)}(x, \frac{W}{2}) = C_\psi^{(n\pm)} \exp\left[i\left(\pm k_x^{(n)} + \frac{W}{2l_c^2}\right)x\right] \tag{7.3}$$

with

$$C_\psi^{(n\pm)} = -\frac{\hbar^2}{2m^*}\frac{1}{V_b b}\left.\frac{d\chi^{(n)}\left(\frac{y}{l_c} \mp l_c k_x^{(n)}\right)}{dy}\right|_{y=W/2}, \tag{7.4}$$

where we write $l_c^2 = \hbar/eB$, and $\chi^{(n)}$ for the n-th eigenfunction for an electron

in the BQW. The Fermi wave vector $k_x^{(n)}$ is real and positive and determined with the Fermi energy E_F by a sum constrained to keep n_s fixed [133]. The $\pm$ sign refers to modes propagating along the $\pm x$ direction.

The eigenfunction of electron in the voltage lead at $y > W/2$ is

$$\phi^{(m)}(x,y) = C_\phi^{(m)} e^{-\frac{1}{2}\eta_m{}^2} H_m(\eta_m) \tag{7.5}$$

with

$$C_\phi^{(m)} = \frac{(1+\gamma^2)^{1/8}}{(2^m m!\pi^{1/2} l_c)^{1/2}} \exp\left[ik_y^{(m)}\left(y - \frac{W}{2}\right)\right] \tag{7.6}$$

and

$$\eta_m = (1+\gamma^2)^{1/4}\frac{x}{l_c} + \frac{1}{(1+\gamma^2)^{3/4}} l_c k_y^{(m)}, \tag{7.7}$$

where m is the mode index, H_m is Hermite polynomial, $k_y^{(m)}$ is the Fermi wave number of the electron, and $\gamma = B_p/B$. The Fermi wave number $k_y^{(m)}$ is either real or imaginary (corresponding to propagating and evanescent mode) due to the parabolic potential confinement.

We choose the $k_y^{(m)}$'s so that the electron energy in the voltage lead is E_F when we expand the tunnelling electron wave function in Eq. (7.3) in the terms of the eigenfunction of electron in the voltage lead at $y = W/2$

$$\psi^{(n\pm)}(x, \frac{W}{2}) = \sum_m g_m^{(n\pm)} \phi^{(m)}(x, \frac{W}{2}) \tag{7.8}$$

The wave functions $\phi^{(m)}(x, W/2)$ are normalised but they are not orthogonal. Consequently, the $g_m^{(n\pm)}$ are determined by using the following equations:

$$\sum_m f_{jm} g_m^{(n\pm)} = h_j^{(n\pm)} \tag{7.9}$$

with

$$f_{jm} = \int_{-\infty}^{+\infty} dx \phi^{(j)}(x, W/2)\phi^{(m)}(x, W/2) \tag{7.10}$$

and

$$h_j^{(n\pm)} = \int_{-\infty}^{+\infty} dx \phi^{(j)}(x, W/2)\psi^{(n\pm)}(x, W/2). \tag{7.11}$$

After solving Eq. (7.9), we can directly calculate the transmission coefficients from their definitions:

$$\begin{aligned} T_{ls} &= \sum_n T_{ls}^{(n)} = \sum_n \frac{1}{v_n} \sum_m v_m \left| g_m^{(n+)} \right|^2, \\ T_{ld} &= \sum_n T_{ld}^{(n)} = \sum_n \frac{1}{v_n} \sum_m v_m \left| g_m^{(n-)} \right|^2, \end{aligned} \tag{7.12}$$

where the summations over n and m include all the values for which $\{n|E_F = E(k_x^{(n)})\}$ and $\{m|k_y^{(m)} \in \mathrm{R}\}$ respectively. Here, the subscripts have the same meaning as in Eq. (7.1) and $v_m \geq 0$ ($v_n \geq 0$) is the group velocity of electron of the m-th (n-th) propagating mode in the voltage lead (BQW) with its energy equals E_F.

The chemical potential defined by Büttiker's formula, Eq. (7.1), can be calculated easily from T_{ls} and T_{ld} in Eq. (7.12). If we have strong potential confinement in the voltage lead, *i.e.* $B_p \gg B$, the leading term of the coefficients f_{jm} and $h_j^{(n\pm)}$ are

$$f_{jm} \simeq \delta_{jm}, \quad h_j^{(n\pm)} \simeq \frac{(2\pi)^{1/2} l_c}{\gamma^{1/2}} i^j C_\phi^{(j)} C_\psi^{(n\pm)} H_j(0). \tag{7.13}$$

Consequently, we can easily show that

$$\begin{aligned} \sum_m v_m \left| g_m^{(n\pm)} \right|^2 &\simeq \sum_m v_m \left| h_m^{(n\pm)} \right|^2 \\ &= \text{const.} \times \gamma^{-1/2} \left| C_\psi^{(n\pm)} \right|^2. \end{aligned} \tag{7.14}$$

Hence, the chemical potential measured by the voltage lead attached to the BQW at the edge $y = W/2$, which is defined by Eq. (7.1), reduces to

$$\mu_l = \frac{\sum_n \frac{1}{v_n} \left(\left| F^{(n+)} \right|^2 \mu_s + \left| F^{(n-)} \right|^2 \mu_d \right)}{\sum_n \frac{1}{v_n} \left(\left| F^{(n+)} \right|^2 + \left| F^{(n-)} \right|^2 \right)} \tag{7.15}$$

where

$$F^{(n\pm)} = \partial \psi^{(n\pm)}(x,y)/\partial y \Big|_{y=W/2}. \tag{7.16}$$

We see by inspection of Eq. (7.15) that Büttiker's chemical potential is identical to the LCP at $y = W/2$ defined by Eq. (7.2) in a BQW with no voltage probes attached. Normal derivatives of the wave functions in the BQW replace the wave functions themselves in Eq. (7.15) because the latter vanish and a limiting procedure is necessary to evaluate the LCP at the boundary. It is important to note that the eigenfunctions of electrons in the voltage lead do not change significantly as we change B when $B_p \gg B$. In this situation, the coupling strength of each mode in the BQW to the voltage lead will depend only on the character of the mode itself and nothing else. As long as these

electron modes are undisturbed by the voltage lead, we can make noninvasive measurements and the LCP defined by Eq. (7.2) which determines the *intrinsic* Hall resistance.

7.3 Model calculations: numerical results

The Hall resistance $R_{\rm H}$ associated with the chemical potential μ_l defined by Büttiker's formula, Eq. (7.1), is obtained by solving Eq. (7.9) with $m^* = 0.067m_e$ for GaAs [39], $W = 100$ nm, and $n_s = 1.1 \times 10^{15}$ m^{-2} so that three subbands are populated when $B = 0$. We include the necessary number of evanescent modes in the voltage leads, such that no change of the expansion coefficient $g_m^{(n\pm)}$ (for the $k_y^{(m)} \in$ R) occurs when we take more evanescent modes into account. The same zero point of potential is used in both the BQW and the voltage leads.

Fig. 7.1 shows the changes of the dependence of $R_{\rm H}$ on B from $B_p \sim B$ to $B_p \gg B$. The solid line is the result of $R_{\rm H}$ associated with the LCP of Eq. (7.2) as studied in Refs. [133, 147], while the dashed line and the dot-and-dash line are the results for $R_{\rm H}$ calculated by Büttiker's formula Eq. (7.1) for $B_p = 1$ T and 11 T respectively. The dotted line is for the longitudinal resistance which is perfectly quantised because there are no reflections in the BQW. We verify from Fig. 7.1 that the $R_{\rm H}$ derived from Büttiker's formula does approach the intrinsic Hall resistance derived from the LCP when we increase B_p and has it as its limit when $B_p \gg B$. In the range of $0 < B < 0.6$ T, there is a quenching of $R_{\rm H}$ for both $B_p = 1$ T and $B_p = 11$ T as we have found for the intrinsic quantum Hall resistance in the BQW with interacting electrons in the last chapter and the magnitude of $R_{\rm H}$ reduces when B_p increases. The dips of $R_{\rm H}$ are deeper than those displayed in the last chapter because only one electron state is used here to calculate $R_{\rm H}$ rather than the SC electron states in a small but finite range of energy due to the chemical potential difference between source and drain. We also notice from Fig. 7.1 is that there is a quantised plateau on the $R_{\rm H}$ curve around $B \sim 2.2$ T when $B_p = 1$ T instead of the dip found when $B_p = 11$ T. This implies that measurements of $R_{\rm H}$ made with two weakly confined voltage

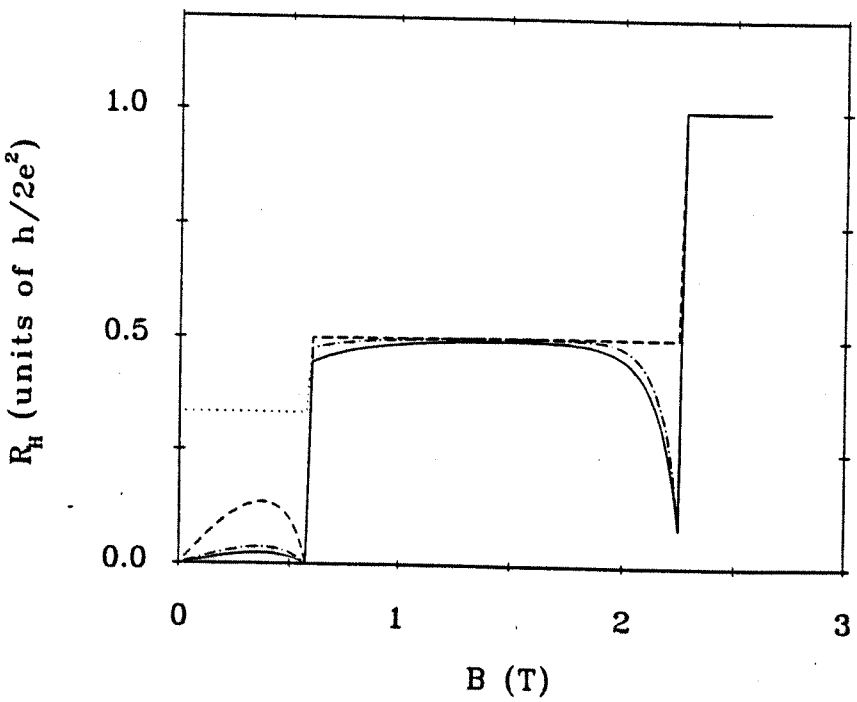

Figure 7.1: Hall resistance $R_{\rm H}$ calculated from Eq. (7.1) when $B_p = 1$ T (dashed line) and 11 T (dot-and-dash line). The $R_{\rm H}$ associated with LCP and the longitudinal resistance of BQW are shown by solid line and dotted line respectively.

leads give results which are similar to those found using a Hall bar geometry. On the other hand, we have confirmed both analytically and numerically, that strongly confined voltage leads give the R_H values predicted by the LCP given in Eq. (7.2).

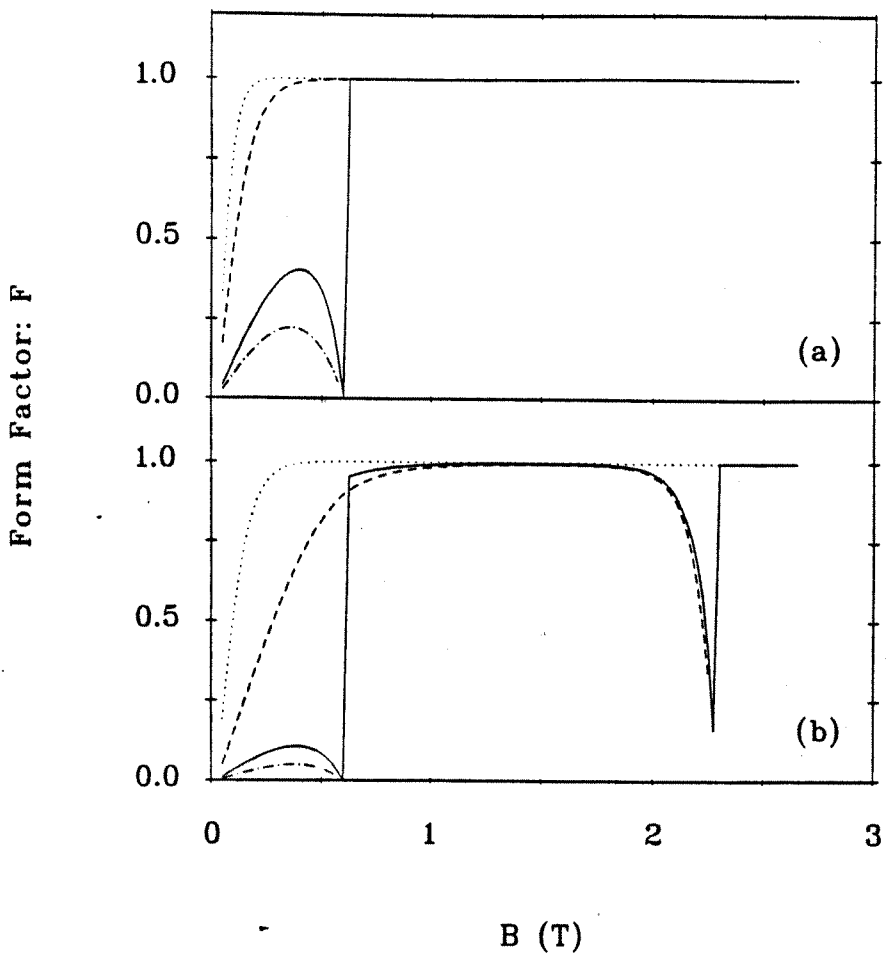

Figure 7.2: The total form factor F (solid line) with three single mode form factor $F^{(1)}$ (dotted line), $F^{(2)}$ (dashed line), and $F^{(3)}$ (dot-and-dash line) for (a) $B_p = 1$ T and (b) $B_p = 11$ T.

In Fig. 7.2, we present results for the single mode form factor $F^{(n)} = (T_{ls}^{(n)} - T_{ld}^{(n)})/(T_{ls}^{(n)} + T_{ld}^{(n)})$ as defined in Ref. [99] for propagating modes. Figs. 7.2(a)

and (b) are for $B_p = 1$ T and 11 T respectively. The dotted, dashed, dot-and-dash, and solid lines are for $F^{(1)}$, $F^{(2)}$, $F^{(3)}$, and the total form factor $F = \sum_n (T_{ls}^{(n)} - T_{ld}^{(n)}) / \sum_n (T_{ls}^{(n)} + T_{ld}^{(n)})$ respectively. Each mode (not only the one closest to the edge of the BQW) makes a contribution to the total form factor. Quantisation of $R_{\rm H}$ can be reached when every single mode form factor $F^{(n)} = 1$. Comparing Figs. 7.2(a) and (b), we can see that $F^{(n)}$ is closer to 1 when $B_p \sim B$ than when $B_p \gg B$. In other words, better quantisation plateaus of $R_{\rm H}$ can be observed by using more loosely confined voltage leads.

7.4 Some remarks

We make some remarks here, which are inspired by discussions about the contents in this chapter with Markus Büttiker [152].

The aim of this chapter is to demonstrate that the so-called local chemical potential can be measured by a voltage lead in some circumstances. Consequently, the intrinsic quantum Hall effect can also be understood in the language of voltage leads instead of virtual contacts. Eq. (7.15) is the result of the special situation which we discuss here. It is valid, we believe, when two necessary conditions are fulfilled: (1) there is such a voltage lead in which energy levels and wavefunctions do not change significantly when the applied magnetic field changes, *e.g.* as a strongly confined lead for which $B_p \gg B$; (2) such a probe does not have any observable effect on the system to be measured, *e.g.* the tunnelling through a high barrier, or an artificial atom [153], or even a remote quantum point contact [152]. In this formula, a conducting channel is dominant only if the ratio of the squared wave function of that channel and the corresponding velocity is much larger than the other ratios. This means that a channel near depopulation gives the largest contribution. The situation in our calculation is different from the experiments of detecting innermost channels by Faist, Guréret, and Meier [154] and Faist [155]. First, in the experiments they use Hall bar geometry rather than a wire and the size of the system is in the order of 10 μm; second, the current they measure is a part of the main system so that the measurement is invasive and the direction of the measurement lead

is along the direction of the current. Moreover, in many cases, the outermost edge channel may play the main role. Our loose confinement probe favours the outermost one even when there is a hard wall.

The voltage lead in our case can support more than one conducting channel. We show our calculated results in Figs. 7.3 and 7.4. The systems used in these two figures are the same except that the confinement potential reference in Fig. 7.4 is lowered by $5\hbar\omega_p$. This difference makes the number of conducting channels different in these two situations. There are ten energy levels involved in the measurement lead when $B_p = 1$ T, some of them are propagating modes (dots in the top parts of each figure) and some of them are evanescent modes (circles in the top parts of each figure). In Fig. 7.3, the number of conducting channels varies from three to one as we increase the applied magnetic field B, while in Fig. 7.4 it varies from eight to three in the same range of B. The Fermi energy levels versus B in the system being measured, a GaAs BQW with $W = 100$ nm and $n_s = 4 \times 10^{14}$ m^{-2}, are also plotted as solid lines in the top parts of both figures. The Hall resistances in both cases are shown in the bottom parts in both figures, where the solid lines refer to the Hall resistance calculated from Büttiker's formula, Eq. (7.1), the dashed lines refer to the Hall resistance associated with the LCP and the dotted lines refer to the longitudinal resistance in the main BQW. Comparing the bottom parts of Figs. 7.3 and 7.4, we find that they are identical. This fact confirms that the measurement procedure in our model *is* noninvasive. While the two kinds of the Hall resistances in both figures do not coincide because here $B_p \sim B$.

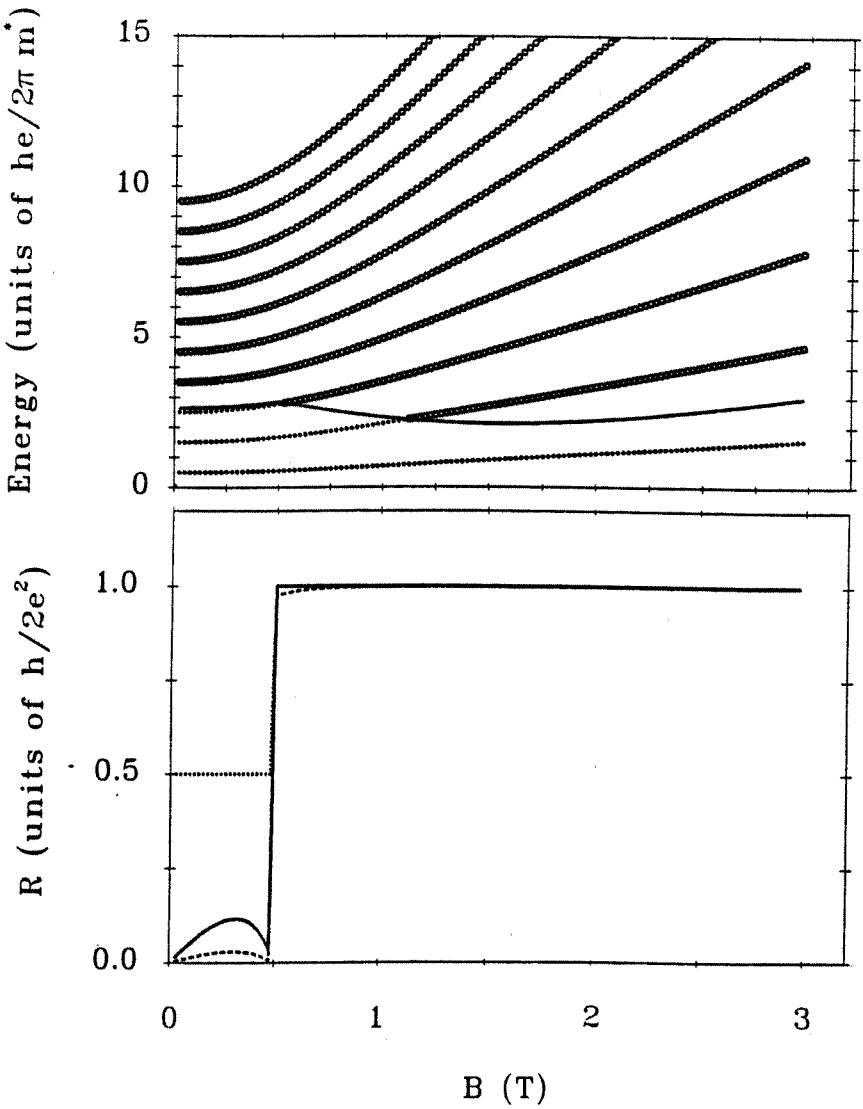

Figure 7.3: The ten energy levels in the measurement with $B_p = 1$ T versus B (top) and the corresponding resistance curves (bottom). In the top figure, the dots refer to propagating modes, the circles refer to evanescent modes and the solid line refers to Fermi energy in the main BQW with $W = 100$ nm and $n_s = 4 \times 10^{14}$ m^{-2}. In the bottom figure, the solid line, dashed line and dotted line refer to the Hall resistances calculated from L-B formula, LCP and the longitudinal resistance respectively.

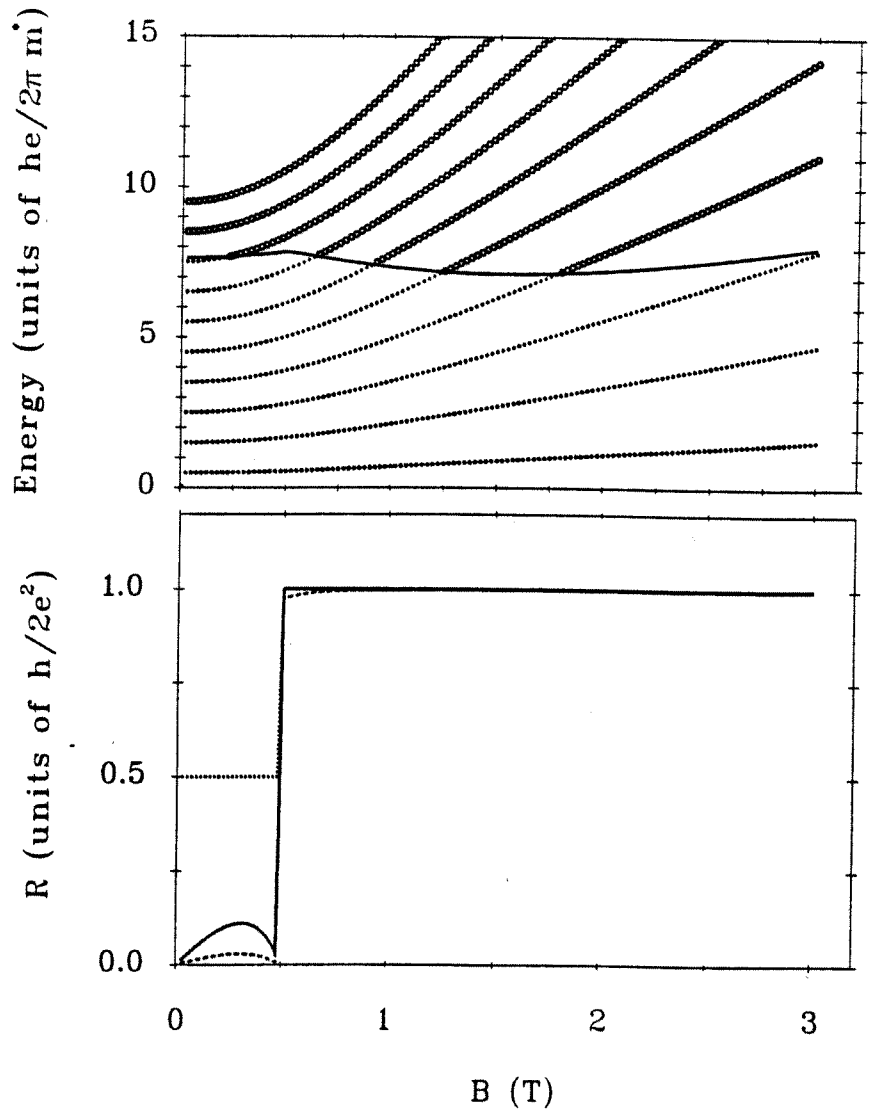

Figure 7.4: The ten energy levels in the measurement with $B_p = 1$ T versus B (top) and the corresponding resistance curves (bottom). The meaning of the symbols and lines as well as the parameters used in our calculations are the same as in Fig. 7.3, except that the potential reference in the measurement lead is lowered by $5\hbar\omega_p$.

Chapter 8

Conclusions

We have shown that the local chemical potential is a suitable parameter to describe the current driving force in a transport microstructure. Its physical nature is discussed in detail. A new definition of local chemical potential is given, which involves only the approximations underlying the Landauer-Büttiker formulae and includes the original formula as its two-lead limit at zero temperature.

The results for the intrinsic quantum Hall effect are presented. We distinguish two kinds of potential responses to a magnetic field and find that they reveal different aspects of the intrinsic quantum Hall effect in a quantum wire. The two corresponding intrinsic Hall resistances are calculated when one or two subbands are occupied. Quantisation is found for the Hall resistance associated with local chemical potential in a large magnetic field. The overlap of oppositely propagating wave functions rounds off the front edge of the quantisation steps at low fields. To a very good approximation the Hall resistance associated with the electrostatic potential is linearly proportional to the magnetic field (as in classical systems) despite of the occurrence of subband depopulation. Distributions of electrostatic Hall potential, local chemical potential, and current density are given.

We find intermittent quenching of the quantum Hall resistance associated with local chemical potential in a uniform ballistic quantum wire as n_s varies. The quenching is intrinsic and produced by overlap near the edges of the wire

of opposite-going wave functions in the same *excited* subband. The overlap is strong at low B when n_s has a value which yields a small Fermi wave number in the uppermost occupied subband. The singularity of the density of states at the bottom of the subband greatly enhances this effect. No quenching is found when this singularity is omitted from the local chemical potential formula. The calculations presented here are self-consistent. We find that both the intra- and inter-subband couplings produced by the Coulomb interaction play a part in determining the quenching behaviour of the quantum Hall resistance. Calculations which do not include Coulomb interaction show less overlap, weaker quenching, and reduced widths of the ranges of n_s in which quenching occurs. The uniform quantum wire has a geometry which is simple enough to allow self-consistent calculations to be carried out relatively easily. However, measurements of the intrinsic quantum Hall resistance of a wire are difficult because they require the insertion of non-invasive probes. For this reason the quantum Hall resistance is usually measured in (at least) a cross with four terminals. The fundamental reason for quenching in the cross is similar to that discussed here: mixing in the Hall voltage probes of the wave functions for electrons emerging from the current source and the current drain. In both cases it is geometry which produces the overlap or mixing: the narrowness of the wire in our calculations and, for example, rounded corners in a cross. In a wire we find that Coulomb interaction is an important factor in determining quenching behaviour. It is expected that this is also true in a cross and the implementation of self-consistent calculations in a cross geometry presents a challenging problem.

We also investigate the possibility of making non-invasive measurement of the local chemical potential and the intrinsic quantum Hall resistance. A model procedure is used for calculation. We show that the chemical potential described by Büttiker's formula has the so-called local chemical potential as its limit when the potential confinement parameter B_p in the voltage leads increases indefinitely. Numerical calculations are carried out, which confirm the limiting behaviour of the quantum Hall resistance R_{H}. Quenching of R_{H} is seen over a

broad range of B_p. Our calculations indicate that it is possible to measure the local chemical potential and the intrinsic quantum Hall effect non-invasively in some circumstances. It is hoped that further experimental studies of this problem will be made.

Appendix A

Exact solutions for a 2DEG in a BQW in a magnetic field

A.1 Hard wall confinement case

A.1.1 Equation

Consider a 2DEG in a BQW lying in x-y plane along x-axis under an external magnetic field B at z-direction. The origin of the y-axis is set at the centre of the wire, and the two edges of the wire are at $y = \pm W/2$ respectively. The electron sheet density and effective mass are n_s and m^* respectively. Here, we ignore the spin of electrons, which does not affect our solutions and can be easily included when it is needed. The Hamiltonian of the system is

$$\mathcal{H} = \frac{1}{2m^*}(\mathbf{p} - q\mathbf{A})^2 + q\phi, \tag{A.1}$$

where

$$\begin{aligned} &\mathbf{p} = -i\hbar\nabla, \\ &q = -e, \\ &\mathbf{A} = (-By, 0, 0), \\ &\phi = \begin{cases} 0, & -W/2 < y < W/2, \\ -\infty, & y \le -W/2, \quad y \ge W/2. \end{cases} \end{aligned} \tag{A.2}$$

The 2D form of the Hamiltonian is:

$$\mathcal{H} = \frac{1}{2m^*}(p_x - eBy)^2 + \frac{1}{2m^*}p_y^2 - e\phi. \tag{A.3}$$

Because

$$[\mathcal{H}, p_x] = 0, \tag{A.4}$$

the corresponding single electron wave function can be expressed in the form:

$$\psi(x,y) = \begin{cases} e^{ik_x x}\chi(y), & -W/2 < y < W/2, \\ 0, & y \le -W/2, \quad y \ge W/2, \end{cases} \tag{A.5}$$

where k_x is the electron wave number at the x direction.

A.1.2 Dimensionless equation

From Schrödinger equation $\mathcal{H}\psi = E\psi$, we have:

$$\chi''(y) + \left[\frac{2m^*E}{\hbar^2} - \frac{1}{l_c^2}(y - l_c^2 k_x)^2\right]\chi(y) = 0 \tag{A.6}$$

for the electrons in the wire when $B > 0$, where $l_c = (\hbar/eB)^{1/2}$. By defining $\xi = y/l_c - l_c k_x$, $\omega_c = eB/m^*$ and $\lambda = 2E/\hbar\omega_c$, we finally get a dimensionless second-order ordinary differential equation for the function χ:

$$\chi''(\xi) + (\lambda - \xi^2)\chi(\xi) = 0 \tag{A.7}$$

with the boundary conditions

$$\chi(\xi_+) = \chi(\xi_-) = 0, \tag{A.8}$$

where $\xi_\pm = \pm W/2l_c - l_c k_x$.

A.1.3 Solutions

Let

$$\chi(\xi) = e^{-\frac{1}{2}\xi^2} f(\xi), \tag{A.9}$$

Eq. (A.7) becomes

$$f''(\xi) - 2\xi f'(\xi) + 2\nu f(\xi) = 0, \tag{A.10}$$

where $\nu = (\lambda - 1)/2$. After expanding $f(\xi)$ by a Taylor series:

$$f(\xi) = \sum_{n=0}^{\infty} a_n \xi^n, \tag{A.11}$$

we have

$$f'(\xi) = \sum_{n=1}^{\infty} n a_n \xi^{n-1},$$
$$f''(\xi) = \sum_{n=2}^{\infty} n(n-1) a_n \xi^{n-2} = \sum_{n=0}^{\infty} (n+2)(n+1) a_{n+2} \xi^n. \tag{A.12}$$

Hence, Eq. (A.10) becomes:

$$\sum_{n=0}^{\infty} \left[(n+2)(n+1) a_{n+2} - 2n a_n + 2\nu a_n \right] \xi^n = 0. \tag{A.13}$$

Therefore, we have the following relation for the coefficients a_n:

$$a_{n+2} = \frac{2(n-\nu)}{(n+2)(n+1)} a_n. \tag{A.14}$$

By using this relation, the general solution of Eq. (A.10), $f(\xi)$, can be rewritten as a linear combination of two linear independent solutions, $H_{e_1}^{(\nu)}(\xi)$ and $H_{e_2}^{(\nu)}(\xi)$:

$$f(\xi) = a_0 H_{e_1}^{(\nu)}(\xi) + a_1 H_{e_2}^{(\nu)}(\xi), \tag{A.15}$$

where

$$H_{e_1}^{(\nu)}(\xi) = 1 + \sum_{n=1}^{\infty} \prod_{k=0}^{n-1} \frac{2(2k-\nu)}{(2k+2)(2k+1)} \xi^{2n},$$
$$H_{e_2}^{(\nu)}(\xi) = \xi \left(1 + \sum_{n=1}^{\infty} \prod_{k=0}^{n-1} \frac{2((2k+1)-\nu)}{(2k+3)(2k+2)} \xi^{2n} \right). \tag{A.16}$$

A.1.4 Linear independence of $H_{e_1}^{(\nu)}(\xi)$ and $H_{e_2}^{(\nu)}(\xi)$

Multiply Eq. (A.10) by $e^{-\xi^2}$ and rewrite it as:

$$\frac{d}{d\xi} \left(e^{-\xi^2} f'(\xi) \right) + 2\nu e^{-\xi^2} f(\xi) = 0. \tag{A.17}$$

We use $H_{e_1}^{(\nu)}(\xi)$ and $H_{e_2}^{(\nu)}(\xi)$ in turn to substitute $f(\xi)$ in Eq. (A.17) and multiply the equation by $H_{e_2}^{(\nu)}(\xi)$ and $H_{e_1}^{(\nu)}(\xi)$ respectively. Then, we have:

$$H_{e_2}^{(\nu)}(\xi) \frac{d}{d\xi} \left(e^{-\xi^2} H_{e_1}^{(\nu)}(\xi) \right) + 2\nu e^{-\xi^2} H_{e_1}^{(\nu)}(\xi) H_{e_2}^{(\nu)}(\xi) = 0 \tag{A.18}$$

and

$$H_{e_1}^{(\nu)}(\xi) \frac{d}{d\xi} \left(e^{-\xi^2} H_{e_2}^{(\nu)}(\xi) \right) + 2\nu e^{-\xi^2} H_{e_1}^{(\nu)}(\xi) H_{e_2}^{(\nu)}(\xi) = 0. \tag{A.19}$$

Subtracting Eq. (A.18) from Eq. (A.19) gives the result:

$$\begin{aligned} & \frac{d}{d\xi}\left[e^{-\xi^2}\left(H_{e_1}^{(\nu)}(\xi)\frac{d}{d\xi}H_{e_2}^{(\nu)}(\xi) - H_{e_2}^{(\nu)}(\xi)\frac{d}{d\xi}H_{e_1}^{(\nu)}(\xi)\right)\right] \\ = & \frac{d}{d\xi}\left[e^{-\xi^2}\mathcal{W}\{H_{e_1}^{(\nu)}(\xi), H_{e_2}^{(\nu)}(\xi)\}\right] \\ = & 0. \end{aligned} \tag{A.20}$$

This implies that the Wronskian, $\mathcal{W}\{H_{e_1}^{(\nu)}(\xi), H_{e_2}^{(\nu)}(\xi)\}$, is

$$\mathcal{W}\{H_{e_1}^{(\nu)}(\xi), H_{e_2}^{(\nu)}(\xi)\} = Ce^{\xi^2}. \tag{A.21}$$

Because

$$H_{e_1}^{(\nu)}(0) = 1, \quad H_{e_2}^{(\nu)}(0) = 0, \quad \frac{d}{d\xi}H_{e_2}^{(\nu)}(0) = 1, \tag{A.22}$$

we have $C = 1$ and $\mathcal{W}\{H_{e_1}^{(\nu)}(\xi), H_{e_2}^{(\nu)}(\xi)\} \neq 0$, *i.e.* $H_{e_1}^{(\nu)}(\xi)$ and $H_{e_2}^{(\nu)}(\xi)$ are linear independent.

A.1.5 Convergence radius of $H_{e_1}^{(\nu)}(\xi)$ and $H_{e_2}^{(\nu)}(\xi)$

From Eq. (A.16), we know that

$$H_{e_1}^{(\nu)}(\xi) = \frac{1}{a_0}\sum_{n=0}^{\infty} a_{2n}\xi^{2n}, \quad H_{e_2}^{(\nu)}(\xi) = \frac{1}{a_1}\sum_{n=0}^{\infty} a_{2n+1}\xi^{2n+1}, \tag{A.23}$$

where the coefficients can be expressed by the same formula:

$$a_{m+2} = \frac{2(m-\nu)}{(m+2)(m+1)}a_m. \tag{A.24}$$

Hence, the convergence radius which is the same for both the $H_{e_1}^{(\nu)}(\xi)$ and $H_{e_2}^{(\nu)}(\xi)$ is

$$R = \lim_{m\to\infty}\left|\frac{a_m}{a_{m+2}}\right| \to \infty, \tag{A.25}$$

i.e. $H_{e_1}^{(\nu)}(\xi)$ and $H_{e_2}^{(\nu)}(\xi)$ are convergent when $\forall\xi \in \mathbf{C}$.

A.1.6 Asymptotic behaviour of $H_{e_1}^{(\nu)}(\xi)$ and $H_{e_2}^{(\nu)}(\xi)$

For both of $H_{e_1}^{(\nu)}(\xi)$ and $H_{e_2}^{(\nu)}(\xi)/\xi$, we have

$$\lim_{m\to\infty}\left|\frac{a_{m+2}}{a_m}\right| \to \left.\frac{2}{m}\right|_{m\to\infty} \tag{A.26}$$

if $\nu \neq$ integers. Similarly, we find that for

$$e^{\xi^2} = \sum_{m=0}^{\infty} b_m \xi^{2n} = \sum_{m=0}^{\infty} \frac{2^n}{n!} \tag{A.27}$$

the limiting behaviour of the ratio of the two adjacent coefficients is

$$\lim_{m\to\infty} \left| \frac{b_{m+1}}{b_m} \right| \to \left. \frac{2}{m} \right|_{m\to\infty}. \tag{A.28}$$

Therefore, for non-integer ν, we have

$$H_{e_1}^{(\nu)}(\xi) \sim e^{\xi^2}, \quad H_{e_2}^{(\nu)}(\xi) \sim \xi e^{\xi^2} \tag{A.29}$$

when $\xi \to \infty$. In fact, because $H_{e_1}^{(\nu)}(\xi)$ and $H_{e_2}^{(\nu)}(\xi)$ are convergent, we can compare the each term of $H_{e_1}^{(\nu)}(\xi)$ and $H_{e_2}^{(\nu)}(\xi)$ with the corresponding terms of e^{ξ^2}/ξ^2 and e^{ξ^2} and obtain that $e^{\xi^2}/\xi^2 < H_{e_1}^{(\nu)}(\xi), H_{e_2}^{(\nu)}(\xi) < e^{\xi^2}$ when $\xi \to \infty$.

A.1.7 Differential and recurrence relations for $H_{e_1}^{(\nu)}(\xi)$ and $H_{e_2}^{(\nu)}(\xi)$

Differentiating $H_{e_1}^{(\nu)}(\xi)$ and $H_{e_2}^{(\nu)}(\xi)$ in Eq. (A.16) and rearranging the results, we get the following differential relations for $H_{e_1}^{(\nu)}(\xi)$ and $H_{e_2}^{(\nu)}(\xi)$:

$$\begin{aligned} \frac{d}{d\xi} H_{e_1}^{(\nu)}(\xi) &= -2\nu H_{e_2}^{(\nu-1)}(\xi), \\ \frac{d}{d\xi} H_{e_2}^{(\nu)}(\xi) &= H_{e_1}^{(\nu-1)}(\xi). \end{aligned} \tag{A.30}$$

Furthermore, by using $H_{e_1}^{(\nu)}(\xi)$ and $H_{e_2}^{(\nu)}(\xi)$ in turn to substitute $f(\xi)$ in Eq. (A.10), we can have the recurrence relations:

$$\begin{aligned} \xi H_{e_1}^{(\nu)}(\xi) &= (\nu+1) H_{e_2}^{(\nu+1)}(\xi) + \nu H_{e_2}^{(\nu-1)}(\xi), \\ \xi H_{e_2}^{(\nu)}(\xi) &= \frac{1}{2}\left(H_{e_1}^{(\nu+1)}(\xi) - \nu H_{e_1}^{(\nu-1)}(\xi) \right). \end{aligned} \tag{A.31}$$

Finally, we would like to mention that by multiplying different coefficients to $H_{e_1}^{(\nu)}(\xi)$ and $H_{e_2}^{(\nu)}(\xi)$, we can define two new functions, $H_1^{(\nu)}(\xi)$ and $H_2^{(\nu)}(\xi)$, which are equivalent to the well known Hermite functions:

$$\begin{aligned} H_1^{(\nu)}(\xi) &= \frac{(-1)^{\nu/2}}{\Gamma(\nu/2)} H_{e_1}^{(\nu)}(\xi), \\ H_2^{(\nu)}(\xi) &= \frac{(-1)^{(\nu-1)/2}}{\Gamma((\nu+1)/2)} H_{e_2}^{(\nu)}(\xi), \end{aligned} \tag{A.32}$$

for which the following symmetric differential and recurrence relations are obtained:

$$\begin{aligned}
&\frac{d}{d\xi}H_1^{(\nu)}(\xi) = 2\nu H_2^{(\nu)}(\xi),\\
&\frac{d}{d\xi}H_2^{(\nu)}(\xi) = 2\nu H_2^{(\nu)}(\xi),\\
&\xi H_1^{(\nu)}(\xi) = \frac{1}{2}\left(H_2^{(\nu+1)}(\xi) - 2\nu H_2^{(\nu-1)}(\xi)\right),\\
&\xi H_2^{(\nu)}(\xi) = \frac{1}{2}\left(H_1^{(\nu+1)}(\xi) - 2\nu H_1^{(\nu-1)}(\xi)\right).
\end{aligned} \tag{A.33}$$

A.1.8 Boundary conditions and secular equation

The hard well boundary conditions,

$$\psi(x,y)|_{y=\pm W/2} = 0, \tag{A.34}$$

result a set of equation:

$$\begin{cases} a_0 H_{e_1}^{(\nu)}(\xi_+) + a_1 H_{e_2}^{(\nu)}(\xi_+) = 0 \\ a_0 H_{e_1}^{(\nu)}(\xi_-) + a_1 H_{e_2}^{(\nu)}(\xi_-) = 0 \end{cases} . \tag{A.35}$$

To get the non-zero solutions of a_0 and a_1 from the above equations, the secular equation should be satisfied:

$$H_{e_1}^{(\nu)}(\xi_+)H_{e_2}^{(\nu)}(\xi_-) - H_{e_1}^{(\nu)}(\xi_-)H_{e_2}^{(\nu)}(\xi_+) = 0 \tag{A.36}$$

which determines the eigenvalues, ν. Then, for each ν, the ratio of a_1 to a_0 is

$$\frac{a_1}{a_0} = -\frac{H_{e_1}^{(\nu)}(\xi_+)}{H_{e_2}^{(\nu)}(\xi_+)} = -\frac{H_{e_1}^{(\nu)}(\xi_-)}{H_{e_2}^{(\nu)}(\xi_-)}. \tag{A.37}$$

Now, only one coefficient hasn't been fixed, and it has to be determined through the procedure of wave function normalisation which we are not going to mention here.

A.2 Parabolic confinement case

We can use the same steps as in the previous section to calculate this problem. The confinement potential, ϕ, is now read as:

$$\phi = -\frac{1}{2}\frac{m^*}{e}\omega_p^2 y^2. \tag{A.38}$$

Moreover, we would like to change the Landau gauge chosen previously a little bit by adding a constant, y_0. This should not affect our final results. We are going to see what the effect of this change. The vector potential, $\mathbf{A}$, is chosen as:

$$\mathbf{A} = (-B(y + y_0), 0, 0). \tag{A.39}$$

Dimensionless equation, Eq. (A.7), can be obtained with exactly the same form with new parameters:

$$\begin{aligned} \lambda &= \frac{l_c^2}{(1+\gamma)^{1/2}} \left[\frac{2m^* E}{\hbar^2} - \left(k_x - \frac{y_0}{l_c^2} \right)^2 \frac{\gamma^2}{(1+\gamma^2)} \right], \\ \xi &= (1+\gamma^2)^{1/4} \frac{y}{l_c} - \frac{1}{(1+\gamma^2)^{3/4}} l_c \left(k_x - \frac{y_0}{l_c^2} \right), \end{aligned} \tag{A.40}$$

where $\gamma = \omega_p/\omega_c$.

The two linear independent solutions are, therefore, the same as in Eq. (A.16). Applying the natural boundary conditions, $\psi(x,y)|_{y\to\pm\infty} = 0$, we have the eigenvalue $\nu = (\lambda - 1)/2 = 0, 1, 2, \cdots$. Hence, the corresponding energy is

$$E = \hbar \left(\omega_c^2 + \omega_p^2 \right)^{1/2} \left(\nu + \frac{1}{2} \right) + \frac{\hbar^2}{2m^*} \left(k_x - \frac{y_0}{l_c^2} \right)^2 \frac{\omega_p^2}{(\omega_c^2 + \omega_p^2)}. \tag{A.41}$$

We see that changing one coordinate of the gauge by a constant is equivalent to shifting the zero point of system momentum at the corresponding direction. Calculations of other physical quantities confirm this conclusion.

Appendix B

The three-point Anderson-Pulay prediction method

In our self-consistent calculations, we need to determine the self-consistent potential function and to choose a optimum trial function for each round. The three-point Anderson-Pulay prediction method [134, 135] is what we use to accelerate the convergence of the self-consistent potential.

Suppose we already know the m-th round input function as $f_{\rm in}^{(m)}$, the corresponding output functions as $f_{\rm out}^{(m)}$, the difference between them is $d^{(m)} = f_{\rm in}^{(m)} - f_{\rm out}^{(m)}$ and the same kind of quantities for the the $(m-1)$-th and $(m-2)$-th rounds as well. Then, the $(m+1)$-th round input function $f_{\rm in}^{(m+1)}$ can be determined by the functions in the previous three rounds through the following way:

$$f_{\rm in}^{(m+1)} = (1-\alpha) g_{\rm in}^{(m)} + \alpha g_{\rm out}^{(m)}, \tag{B.1}$$

with

$$\begin{aligned} g_{\rm in}^{(m)} &= (1-\beta_1-\beta_2) f_{\rm in}^{(m)} + \beta_1 f_{\rm in}^{(m-1)} + \beta_2 f_{\rm in}^{(m-2)}, \\ g_{\rm out}^{(m)} &= (1-\beta_1-\beta_2) f_{\rm out}^{(m)} + \beta_1 f_{\rm out}^{(m-1)} + \beta_2 f_{\rm out}^{(m-2)} \end{aligned} \tag{B.2}$$

where $0 < \alpha < 1$ is chosen artificially and is fixed during the whole calculation, while β_1 and β_2 are calculated separately for each round.

The departure of the function $g^{(m)}$ can be defined as:

$$\begin{aligned}\bar{D} &= D\left[g_{\rm in}^{(m)}, g_{\rm out}^{(m)}\right] \\ &= \langle g_{\rm in}^{(m)} - g_{\rm out}^{(m)} | g_{\rm in}^{(m)} - g_{\rm out}^{(m)} \rangle^{1/2} \\ &= \Big[\langle d^{(m)}|d^{(m)}\rangle - 2\beta_1\langle d^{(m)}|d^{(m)} - d^{(m-1)}\rangle \\ &\quad -2\beta_2\langle d^{(m)}|d^{(m)} - d^{(m-2)}\rangle + 2\beta_1\beta_2\langle d^{(m)} - d^{(m-1)}|d^{(m)} - d^{(m-2)}\rangle \\ &\quad +\beta_1^2 D^2[d^{(m)}, d^{(m-1)}] + \beta_2^2 D^2[d^{(m)}, d^{(m-2)}]\Big]^{1/2}.\end{aligned} \tag{B.3}$$

The partial derivatives of $\bar{D}$ are

$$\begin{aligned}\frac{\partial \bar{D}}{\partial \beta_1} &= \frac{2}{\bar{D}}\Big[-\langle d^{(m)}|d^{(m)} - d^{(m-1)}\rangle \\ &\quad +\beta_2\langle d^{(m)} - d^{(m-1)}|d^{(m)} - d^{(m-2)}\rangle + \beta_1 D^2[d^{(m)}, d^{(m-1)}]\Big], \\ \frac{\partial \bar{D}}{\partial \beta_2} &= \frac{2}{\bar{D}}\Big[-\langle d^{(m)}|d^{(m)} - d^{(m-2)}\rangle \\ &\quad +\beta_1\langle d^{(m)} - d^{(m-1)}|d^{(m)} - d^{(m-2)}\rangle + \beta_2 D^2[d^{(m)}, d^{(m-2)}]\Big].\end{aligned} \tag{B.4}$$

Let these two first-order derivatives be zero, *i.e.*

$$\frac{\partial \bar{D}}{\partial \beta_1} = \frac{\partial \bar{D}}{\partial \beta_2} = 0, \tag{B.5}$$

we determine β_1 and β_2 and give the prediction for the $(m+1)$-th round input function $f_{\rm in}^{(m+1)}$ though Eqs. (B.1) and (B.2).

The coefficients, β_1 and β_2, determined by Eq. (B.5) assures the convergence of the self-consistent potential. This is because

$$\begin{aligned}\frac{\partial^2 \bar{D}}{\partial \beta_1^2} &= \frac{1}{\bar{D}} D^2[d^{(m)}, d^{(m-1)}] \geq 0, \\ \frac{\partial^2 \bar{D}}{\partial \beta_1^2}\frac{\partial^2 \bar{D}}{\partial \beta_2^2} - \frac{\partial^2 \bar{D}}{\partial \beta_1 \partial \beta_2}\frac{\partial^2 \bar{D}}{\partial \beta_2 \partial \beta_1} &= \frac{1}{\bar{D}}\Big[D^2[d^{(m)}, d^{(m-1)}]D^2[d^{(m)}, d^{(m-2)}] \\ &\quad -\langle d^{(m)} - d^{(m-1)}|d^{(m)} - d^{(m-2)}\rangle^2\Big] \geq 0\end{aligned} \tag{B.6}$$

when Eq. (B.5) is satisfied. The last inequality in Eq. (B.6) is obtained with the help of Cauchy inequality.

Bibliography

[1] J. R. Schrieffer, in *Semiconductor Surface Physics*, edited by R. H. Kingston, University of Pennsylvania Press, Philadelphia, 1957.

[2] A. B. Fowler, F. F. Fang, W. E. Howard, and P. J. Stiles, Phys. Rev. Lett., **16**, 901 (1966).

[3] R. Dingle, A. C. Gossard, and W. Weigmann, Phys. Rev. Lett., **33**, 827 (1974).

[4] K. von Klitzing, G. Dorda, and M. Pepper, Phys. Rev. Lett., **45**, 494 (1980).

[5] R. Dingle, H. L. Stormer, A. C. Gossard, and W. Weigmann, Appl. Phys. Lett., **33**, 665 (1978).

[6] C. T. Foxon, J. J. Harris, D. Hilton, J. Hewett, and C. Roberts, Semicond. Sci. Technol., 4, 582 (1989).

[7] A. A. M. Staring, Ph. D. Thesis, Technical University of Eindhoven, 1992.

[8] T. J. Thornton, M. Pepper, H. Ahmed, D. Andrews, and G. J. Davies, Phys. Rev. Lett., **56**, 1198 (1986).

[9] B. J. van Wees, H. van Houten, C. W. J. Beenakker, J. G. Williamson, L. P. Kouwenhoven, D. van der Marel, and C. T. Foxon, Phys. Rev. Lett., **60**, 848 (1988).

[10] D. A. Wharam, T. J. Thornton, R. Newbury, M. Pepper, H. Ahmed, J. E. F. Frost, D. G. Hasko, D. C. Peacock, D. A. Ritchie, and G. A. C. Jones, J. Phys. C, **21**, L209 (1988).

[11] H. van Houten, B. J. van Wees, M. G. J. Heijman, and J. P. Andre, Appl. Phys. Lett., **49**, 1781 (1986).

[12] M. A. Reed, J. N. Randall, R. J. Aggarwal, R. J. Matyi, T. M. Moore, and A. E. Wetsel, Phys. Rev. Lett. **60**, 535 (1988).

[13] H. van Houten, C. W. J. Beenakker, J. G. Williamson, M. E. I. Broekaart, P. H. M. van Loosdrecht, B. J. van Wees, J. E. Mooij, C. T. Foxon, and J. J. Harris, Phys. Rev. B, **39**, 8556 (1989).

[14] T. A. Fulton and G. J. Dolan, Phys. Rev. Lett. **59**, 807 (1987).

[15] L. S. Kuzmin, P. Delsing, T. Claeson, and K. K. Likharev, Phys. Rev. Lett., **62**, 2539 (1989).

[16] Y. Aharonov and D. Bohm, Phys. Rev., **115**, 485 (1957).

[17] G. Badurek, H. Rauch and J. Summhammer, Phys. Rev. Lett. **51**, 1015 (1983).

[18] E. Abrahams, P. W. Anderson, D. C. Licciardello, and T. V. Ramakrishnan, Phys. Rev. Lett., **42**, 673 (1979).

[19] S. Washburn and R. A. Webb, Adv. Phys., **35**, 375 (1986).

[20] B. L. Al'tshuler and B. I. Shoklovskii, Sov. Phys. JETP, **64**, 127 (1986).

[21] L. P. Levy, G. Dolan, J. Dunsmuir, and H. Bouchiat, Phys. Rev. Lett., **64**, 2094 (1990).

[22] O. D. Cheishvili, Sov. Phys. JETP Lett., **48**, 225 (1988).

[23] H. Fukuyama, J. Phys. Soc. Jpn., **58**, 47 (1989).

[24] B. L. Al'tshuler, Y. Gefen, and Y. Imry, Phys. Rev. Lett., **66**, 88 (1991).

[25] A. D. Stone, in *Physics of Nanostructures*, edited by J. H. Davies and A. R. Long, IOP Publishing, Bristol, 1992.

[26] R. A. Webb, S. Washburn, C. P. Umback, and R. B. Laibowitz, Phys. Rev. Lett., **54**, 2696 (1985).

[27] G. Timp, A. M. Chang, P. Mankiewich, R. Behringer, J. E. Cunningham, T. Y. Chang, and R. E. Howard, Phys. Rev. Lett., **59**, 732 (1987).

[28] E. H. Hall, Am. J. Math., **2**, 287 (1879).

[29] N. W. Ashcroft and N. D. Mermin, *Solid State Physics*, Holt, Rinehart and Winston, New York, 1976.

[30] R. E. Prange, in *The Quantum Hall Effect*, edited by R. E. Prange and S. M. Girvin, Springer-Verlag, New York, 1987.

[31] K. von Klitzing, Surface Science, **113**, 1 (1982).

[32] D. C. Tsui, H. L. Stömer, and A. C. Gossard, Phys. Rev. Lett., **48**, 1559 (1982).

[33] M. Büttiker, in *Nanostructured Systems*, Vol. 35 of *Semiconductors and Semimetals*, edited by M. A. Reed, Academic Press, San Diego, 1992.

[34] N. d'Ambrumenil, in *Quantum Transport in Semiconductors*, edited by D. K. Ferry and C. Jacoboni, Plenum Press, New York, 1992.

[35] T. Ando, A. B. Fowler, and F. Stern, Rev. Mod. Phys., **54**, 437 (1982).

[36] G. D. Mahan, *Many-Partical Theory*, Plenum Press, New York, 1981.

[37] F. F. Feng and W. E. Howard, Phys. Rev. Lett., **16**, 797 (1966).

[38] M. A. Gell, D. Ninno, M. Jaros, D. J. Wolford, T. F. Kuech, and J. A. Bradley, Phys. Rev. B, **35**, 1196 (1987).

[39] C. W. J. Beenakker and H. van Houten, in Vol. 44 of *Solid State Physics: Advances in the Research and Applications*, edited by H. Ehrenreich and D. Turnbull, Academic Press, New York, 1991.

[40] F. Stern, in *Physics of Nanostructures*, edited by J. H. Davies and A. R. Long, IOP Publishing, Bristol, 1992.

[41] J. A. Brum and G. Bastard, Superlatt. and Microstruct., **4**, 443 (1988).

[42] S. E. Laux and F. Stern, Appl. Phys. Lett., **49**, 91 (1986).

[43] S. E. Laux, D. J. Frank, and F. Stern, Surf. Sci., **196**, 101 (1988).

[44] K. Kojima, K. Mitsunaga, and K. Kyuma, Appl. Phys. Lett., **55**, 862 (1989).

[45] K. F. Berggren, T. J. Thornton, D. J. Newson, and M. Pepper, Phys. Rev. Lett., **57**, 1769 (1986).

[46] T. P. Smith, H. Arnot, J. M. Hong, C. M. Knoedler, S. E. Laux, and H. Schmid, Phys. Rev. Lett., **59**, 2082 (1987).

[47] F. Stern, private communications.

[48] J. C. Maan, in *Two-dimensional Systems, Heterostructures, and Superlattices*, Vol. 53 of *Springer Series in Solid-State Sciences*, edited by G. Bauer, F. Kuchar, and H. Heinrich, Springer-Verlag, Berlin, 1984.

[49] C. W. J. Beenakker, H. van Houten, and B. J. van Wees, Superlatt. and Microstruct., **5**, 127 (1989).

[50] B. I. Halperin, Phys. Rev. B, **25**, 2185 (1982).

[51] For example, see L. E. Reichl, *A Modern Course in Statistical Physics*, University of Texas Press, 1980.

[52] P. Drude, Ann. der Physik, **1**, 566 (1900); **3**, 369 (1900); **7**, 687 (1902).

[53] L. D. Landau and E. M. Lifshitz, *Statistical Physics*, Pergamon Press, Oxford, 1958.

[54] A. B. Pippard, *The Dynamics of Conduction Electrons*, Blackie & Son Ltd., London, 1965.

[55] P. N. Butcher, in *Crystalline Semiconducting Materials and Devices*, edited by P. N. Butcher, N. H. March, and M. P. Tosi, Plenum Press, New York, 1986.

[56] R. Kubo, J. Phys. Soc. Jpn., **12**, 570 (1957).

[57] P. N. Butcher, in *Electrons in Crystalline Solids*, edited by A. Salam, IAEA, Vienna, 1973.

[58] *Quantum Transport in Semiconductors*, edited by D. K. Ferry and C. Jacoboni, Plenum Press, New York, 1992.

[59] A. D. Stone and A. Szafer, IBM J. Res. Develop., **32**, 384 (1988).

[60] R. Landauer, IBM J. Res. Develop., **1**, 223 (1957).

[61] R. Landauer, in *Localization, Interaction, and Transport Phenomena*, edited by G. Bergmann and Y. Bruynseraede, Springer-Verlag, Heidelberg, 1985.

[62] R. Landauer, Phil. Mag., **21**, 863 (1970).

[63] R. Kubo, in Vol. 1 of *Lectures in Physics*, edited by W. E. Brittin and L. G. Dunham, Interscience Publishers Inc., New York, 1959.

[64] P. W. Anderson, D. J. Thouless, E. Abrahams, and D. S. Fisher, Phys. Rev. B, **22**, 3519 (1980).

[65] D. J. Thouless, Phys. Rev. Lett., **39**, 1167 (1977).

[66] D. J. Thouless, Phys. Rev. Lett., **47**, 972 (1981).

[67] D. C. Langreth and E. Abrahams, Phys. Rev. B, **24**, 2978 (1981).

[68] M. Ya. Azbel, J. Phys. C, **14**, L225 (1981).

[69] M. Büttiker, Y. Imry, R. Landauer, and S. Pinhas, Phys. Rev. B, **31**, 6207 (1985).

[70] H. L. Engquist and P. W. Anderson, Phys. Rev. B, **24**, 1151 (1981).

[71] E. N. Economou and C. M. Soukoulis, Phys. Rev. Lett., **46**, 618 (1981).

[72] D. S. Fisher and P. A. Lee, Phys. Rev. B, **23**, 6851 (1981).

[73] P. A. Lee and D. S. Fisher, Phys. Rev. Lett., **47**, 882 (1981).

[74] Y. Imry, Europhys. Lett., **1**, 249 (1986).

[75] M. Büttiker, Phys. Rev. Lett., **57**, 1761 (1986).

[76] R. Kubo, et al., *Solid State Physics*, McGraw-Hill Inc., New York, 1969.

[77] L. Onsager, Phys. Rev., **37**, 405 (1931); Phys. Rev., **38**, 2265 (1931).

[78] H. B. G. Casimir, Rev. Mod. Phys., **17**, 343 (1945).

[79] M. Büttiker, Y. Imry, and M. Ya. Azbel, Phys. Rev. A, **30**, 1982 (1984).

[80] M. Büttiker, IBM J. Res. Develop., **32**, 317 (1988).

[81] P. N. Butcher, J. Phys.: Condens. Matter, **2**, 4869 (1990).

[82] G. F. C. Searle, *The Electrician*, **66**, 999 (1911).

[83] Y. Imry, in *Directions in Condensed Matter Physics*, Vol. 1, edited by G. Grinstein and G. Mazenko, World Scientific Publishing Co., Singapore, 1986.

[84] Yu. V. Sharvin, Sov. Phys. JETP, **21**, 655 (1965).

[85] H. Z. Zheng, in *Lectures for the Workshop on the Semiconductor Superlattice and Quantum Well Physics and Devices* (in Chinese), Guangzhou, 1991.

[86] R. Kubo, *Statistical Mechanics*, North-Holland Publishing Co., Amsterdam, 1965.

[87] S. N. Bose, Z. Physik, **26**, 178 (1924).

[88] A. Einstein, Berliner Ber., 261 (1924); 3 (1925); 18 (1925).

[89] E. Fermi, Z. Physik, **36**, 902 (1926).

[90] P. A. M. Dirac, Proc. Roy. Soc., **A112**, 661 (1926).

[91] K. von Klitzing, in *The Physics of the Two-Dimensional Electron Gas*, edited by J. T. Devreese and F. M. Peeters, Plenum Press, New York, 1987.

[92] R. Landauer, IBM J. Res. Develop., **32**, 306 (1988).

[93] R. Landauer, J. Phys. C: Solid State Phys., **8**, 761 (1975).

[94] M. Büttiker, Phys. Rev. B, **33**, 3020 (1986).

[95] M. Büttiker, Phys. Rev. B, **40**, 3409 (1986).

[96] M. Büttiker, in *Analogies in Optics and Micro Electronics*, edited by W. van Haeringen and D. Lenstra, Kluwer Academic Publishers, Netherlands, 1990.

[97] O. Entin-Wohlman, C. Hartzstein, and Y. Imry, Phys. Rev. B, **34**, 921 (1986).

[98] Y. Imry, in *Nanostructure Physics and Fabrication*, edited by M. A. Reed and W. P. Kirk, Academic Press, San Diego, 1989.

[99] F. M. Peeters, Phys. Rev. Lett., **61**, 589 (1988).

[100] H. Akera and T. Ando, Phys. Rev. B, **39**, 5508 (1989).

[101] H. Akera and T. Ando, Phys. Rev. B, **41**, 11967 (1990).

[102] P. N. Butcher and D. P. Chu, J. Phys.: Condens. Matter **5**, L633 (1993).

[103] See, e.g., *The Physics of the Two-Dimensional Electron Gas*, edited by J. T. Devreese and F. M. Peeters, Plenum Press, New York, 1987.

[104] See, e.g., *The Quantum Hall Effect*, edited by R. E. Prange and S. M. Girvin, Springer-Verlag, New York, 1987.

[105] R. B. Laughlin, Phys. Rev. B, **23**, 5632 (1981).

[106] E. Teller, Z. Phys., **67**, 311 (1931).

[107] R. B. Laughlin, Phys. Rev. Lett., **50**, 1395 (1983).

[108] F. D. M. Haldane, Phys. Rev. Lett., **51**, 605 (1983).

[109] Q. Niu and D. J. Thouless, J. Phys. A, **17**, 2453 (1984); Phys. Rev. B, **25**, 2185 (1987).

[110] J. E. Avron, A. Raveh, and B. Zur, Rev. Mod. Phys., **60**, 873 (1988).

[111] J. K. Jain, Phys. Rev. Lett., **63**, 199 (1989); Phys. Rev. B, **41**, 7653 (1990); Adv. Phys., **41**, 105 (1992).

[112] B. I. Halperin, P. A. Lee, and N. Read, Phys. Rev. B, **47**, 7312 (1993).

[113] B. J. van Wees, E. M. M. Willems, C. J. P. M. Harmans, C. W. J. Beenakker, H. van Houten, J. G. Williamson, C. T. Foxon, and J. J. Harris, Phys. Rev. Lett., **62**, 1181 (1989).

[114] S. Komiyama, H. Hirai, S. Sasa, and S. Hiyamizu, Phys. Rev. B, **40**, 12566 (1989).

[115] M. Büttiker, Phys. Rev. B, **38**, 9375 (1988).

[116] M. Büttiker, Phys. Rev. B, **38**, 12724 (1988).

[117] C. W. J. Beenakker, Phys. Rev. Lett., **64**, 216 (1990).

[118] S. Komiyama, H. Hirai, S. Sasa, and F. Fujii, Solid State Commun., **73**, 91 (1990).

[119] B. J. van Wees, E. M. M. Willems, L. P. Kouwenhoven, C. J. P. M. Harmans, J. G. Williamson, C. T. Foxon, and J. J. Harris, Phys. Rev. B, **39**, 8066 (1989).

[120] T. Martin and S. Feng, Phys. Rev. Lett., **64**, 1971 (1990).

[121] B. W. Alphenaar, P. L. McEuen, R. G. Wheeler, and R. N. Sacks, Phys. Rev. Lett., **64**, 677 (1990).

[122] R. Landauer, Z. Phys. B, **68**, 217 (1987).

[123] K. L. Shepard, M. L. Roukes, and B. P. van der Gaag, Phys. Rev. Lett., **68**, 2660 (1992).

[124] D. G. Ravenhall, H. W. Wyld, and R. L. Schult, Phys. Rev. Lett., **62**, 1780 (1989).

[125] R. L. Schult, H. W. Wyld, and D. G. Ravenhall, Phys. Rev. B, **41**, 12760 (1990).

[126] T. Geisel, R. Ketzmerick, and O. Schedletzky, Phys. Rev. Lett., **69**, 1680 (1992).

[127] R. W. Rendell and S. M. Girvin, Phys. Rev. B, **23**, 6610 (1981).

[128] A. H. MacDonald, T. M. Rice, and W. F. Brinkman, Phys. Rev. B, **28**, 3648 (1983).

[129] Q. Li and D. J. Thouless, Phys. Rev. Lett., **65**, 767 (1990).

[130] F. M. Peeters, Superlatt. and Microstruct., **6**, 217 (1989).

[131] H. Akera and T. Ando, Surf. Sci., **229**, 268 (1990).

[132] D. B. Chklovskii, B. I. Shklovskii, and L. I. Glazman, Phys. Rev. B, **46**, 4026 (1992).

[133] D. P. Chu and P. N. Butcher, Phys. Rev. B, **47**, 10008 (1993).

[134] D. G. Anderson, J. Asso. Comput. March., **12**, 547 (1964).

[135] P. Pulay, Chem. Phys. Lett., **73**, 393 (1980).

[136] D. J. Thouless, Phys. Rev. Lett., **71**, 1879 (1993).

[137] M. L. Roukes, A. Scherer, S. J. Allen, Jr., H. G. Craighead, R. M. Ruthen, E. D. Beebe, and J. P. Harbison, Phys. Rev. Lett. **59**, 3011 (1987).

[138] C. J. B. Ford, T. J. Thornton, R. Newbury, M. Pepper, H. Ahmed, D. C. Peacock, D. A. Ritchie, J. E. F. Frost, and G. A. C. Jones, Phys. Rev. B **38**, 8518 (1988).

[139] C. J. B. Ford, S. Washburn, M. Büttiker, C. M. Knoedler, and J. M. Hong, Phys. Rev. Lett. **62**, 2724 (1989).

[140] A. M. Chang, T. Y. Chang, and H. U. Baranger, Phys. Rev. Lett. **63**, 996 (1989).

[141] G. Timp, H. U. Baranger, P. de Vegvar, J. E. Cunningham, R. E. Howard, R. Behringer, and P. M. Mankiewich, Phys. Rev. Lett. **60**, 2081 (1988).

[142] Y. Takagaki, K. Gamo, S. Ishida, K. Ishibashi, and Y. Aoyagi, Solid State Commun. **68**, 1051 (1988).

[143] T. Kakuta, Y. Takagaki, K. Gamo, S. Namba, S. Takaoka, and K. Murase, Phys. Rev. B **43**, 14321 (1991).

[144] G. Kirczenow, Phys. Rev. B **39**, 10452 (1989).

[145] H. U. Baranger and A. D. Stone, Phys. Rev. Lett. **63**, 414 (1989); H. U. Baranger, D. P. DiVincenzo, R. A. Jalabert, and A. D. Stone, Phys. Rev. B **44**, 10637 (1991).

[146] C. W. J. Beenakker and H. van Houten, Phys. Rev. Lett. **63**, 1857 (1989).

[147] D. P. Chu and P. N. Butcher, J. Phys.: Condens. Matter **5**, L397 (1993).

[148] D. L. Maslov, C. Barnes, and G. Kirczenow, Phys. Rev. Lett. **70**, 1984 (1993).

[149] M. Field, C. G. Smith, M. Pepper, D. A. Ritchie, J. E. F. Frost, G. A. C. Jones, and D. G. Hasko, Phys. Rev. Lett. **70**, 1311 (1993).

[150] M. Büttiker, in *Analogies in Optics and Micro Electronics*, edited by W. van Haeringen and D. Lenstra (Kluwer Academic Publishers, Netherlands, 1990.

[151] D. P. Chu and P. N. Butcher, Phys. Rev. Lett., **72**, 3698 (1994).

[152] M. Büttiker, private communications.

[153] O. Klein, C. de C. Chamon, D. Tang, D. M. Abush-Magder, X.-G. Wen, M. A. Kastner, and S. J. Wind, preprint, 1994.

[154] J. Faist, P. Guére, and H. P. Meier, Phys. Rev. B, **43**, 9332 (1991).

[155] J. Faist, Europhys. Lett., **15**, 331 (1991).